Pocket Rocket: An electrothermal plasma micro-thruster

Amelia Diane Greig

A thesis submitted for the degree of

Doctor of Philosophy

of The Australian National University

July 2015

Declaration

This thesis is an account of research undertaken between February 2012 and July 2015 at The Research School of Physics and Engineering, College of Physical and Mathematical Sciences, The Australian National University, Canberra, Australia. Except where acknowledged in the customary manner, the material presented in this thesis is, to the best of my knowledge, original and has not been submitted in whole or part for a degree in any university.

Amelia Diane Greig

July 2015

To my parents,

for giving me the confidence to tackle any challenge

and to my nephews, may you have the same opportunities in life as me

Acknowledgments

The past three and a half years have been some of the most amazing of my life to date, due entirely to the wonderful guidance and friendship I have received from my supervisors, Christine Charles and Rod Boswell. Christine, you are the best role model possible for a young female researcher and I hope that I can take what you have taught me on board and have a career even half as successful as yours. Rod, our conversations are always entertaining and educational; you have taught me so much, and not just about plasma physics but life in general. I also would like to thank you both for patiently trying to teach me to surf, and introducing me to the wonder that is canoeing down a river for days at a time. I have never before met supervisors who are so open and welcoming to their students, and I will be eternally grateful for everything you have done for me over these short years.

A large portion of this work would not have been possible without the assistance of Rhys Hawkins, thanks to his contribution writing the rovibrational spectroscopy fitting code. Best of luck finishing your own Ph.D. now Rhys! This work would also not have been possible without the technical brilliance of Peter Alexander, Steven Holgate, Dennis Gibson and the rest of the mechanical and electrical workshop staff, and James, Martin and Julie in the School Computer Unit. Your efforts over the years to keep equipment functioning, repair broken components, and help set up new parts are greatly appreciated and it is safe to say this work could not have happened without your help. Similarly, thank you to the wonderful admin staff at RSPE, especially Karen N, Karen S, Luda, Uyen and Suzie. Your help with all my student, finance and travel matters have made this experience much simpler.

This experience has been made significantly better by being part of the wonderful group that is the Space Plasma, Power and Propulsion lab. Thank you to Andrew Bish for teaching me all about RF electronics, and to James, Sam, Craig, Yunchao

and Andy for creating such a great team dynamic and for always being there for a chat. I would also like to thank Naomi Mathers from RSAA for your continual guidance and suggestions for moving forwards after my Ph.D.

I am very lucky to have a wonderful group of friends from RSPE, the highland dancing world and the ANU hockey club, to relax and take a break from work with. A special thank you must go to Andrew Papworth; the philosophers drinking club after hockey on Thursdays has been great fun and educational and I hope you manage to keep the tradition alive.

A great part of my personal development and growth during the past few years that has allowed me to complete my Ph.D. as a well-rounded individual with a broad skill set encompassing more than research ability is due to Michael West and the rest of the AIAA Sydney Section council. It was great to be involved with such a proactive and interesting group of people working together to organise various events to promote and advance the aerospace sciences within Australia.

Finally, I would like to thank my family for the love and support they have given me my entire life. It is much easier to take on the challenges of life knowing you have set me up with everything I need to succeed, but will also always be there if I need you.

Publications

This thesis has resulted in a number of publications in peer reviewed journals, as listed below. Some of the results presented in the chapters to follow have been adapted from the material in these publications.

- **A. Greig,** C. Charles, R. Hawkins and R.W. Boswell, *Direct measurement of neutral gas heating in a radio-frequency electrothermal plasma micro-thruster*, **Applied Physics Letters,** 103, 074101 (2013)

- **A. Greig,** C. Charles, N. Paulin and R.W. Boswell, *Volume and surface propellant heating in an electrothermal radio-frequency plasma micro-thruster*, **Applied Physics Letters,** 105, 054102 (2014)

- **A. Greig,** C. Charles and R.W. Boswell, *Plume Characteristics of an Electrothermal Plasma Microthruster*, **IEEE Trans. on Plasma Science,** Vol 42, No 10, (2014)

- **A. Greig,** C. Charles and R.W. Boswell, *Simulation of main plasma parameters of a cylindrical asymmetric capacitively coupled plasma micro-thruster using computational fluid dynamics*, **Frontiers in Plasma Physics,** Vol 2, No 80, (2015)

- C. Charles, A. Bish, R.W. Boswell, J. Dedrick, **A. Greig,** R. Hawkins and T.S. Ho, *A short review of experimental and computational diagnostics for radiofrequency plasma micro-thrusters*, **Plasma Chemistry and Plasma Processing**, Online Sept 2015

- **A. Greig,** C. Charles and R.W. Boswell, *Spatiotemporal study of gas heating mechanisms in a radio-frequency electrothermal plasma micro-thruster*, **Frontiers in Plasma Physics**, Vol 2, No 84, (2015)

Abstract

Recently, an increase in use of micro-satellites constructed from commercial off the shelf (COTS) components has developed, to address the large costs associated with designing, testing and launching satellites. One particular type of micro-satellite of interest are CubeSats, which are modular 10 cm cubic satellites with total weight less than 1.33 kg. To assist with orbit boosting and attitude control of CubeSats, micro-propulsion systems are required, but are currently limited.

A potential electrothermal plasma micro-thruster for use with CubeSats or other micro-satellites is under development at The Australian National University and forms the basis for this work. The thruster, known as 'Pocket Rocket', utilises neutral gas heating from ion-neutral collisions within a weakly ionised asymmetric plasma discharge, increasing the exhaust thermal velocity of the propellant gas, thereby producing higher thrust than if the propellant was emitted cold.

In this work, neutral gas temperature of the Pocket Rocket discharge is studied in depth using rovibrational spectroscopy of the nitrogen (N_2) second positive system ($C^3\Pi_u \rightarrow B^3\Pi_g$), using both pure N_2 and argon/N_2 mixtures as the operating gas. Volume averaged steady state gas temperatures are measured for a range of operating conditions, with an analytical collisional model developed to verify experimental results. Results show that neutral gas heating is occurring with volume averaged steady state temperatures reaching 430 K in N_2 and 1060 K for argon with 1% N_2 at standard operating conditions of 1.5 Torr pressure and 10 W power input, demonstrating proof of concept for the Pocket Rocket thruster. Spatiotemporal profiles of gas temperature identify that the dominant heating mechanisms are ion-neutral collisions within the discharge and wall heating from ion bombardment of the thruster walls.

To complement the experimental results, computational fluid dynamics (CFD) simulations using the commercial CFD-ACE+ package are performed. Simulation

results demonstrate that the discharge is driven by ion induced secondary or 'gamma' electrons emitted from the surface of the plasma cavity radial wall in the vicinity of the powered electrode. These electrons are accelerated to high velocities through an enhanced sheath formed by the asymmetry of the device, creating a peak in ion density within the centre of the discharge tube.

Contents

List of Figures

Chapter 1

Introduction

The first artificial satellite to successfully reach space was Sputnik 1, launched on 4 October 1957. Since then, the number of artificial satellites launched by humans has passed several thousand and they now form an integral part of modern civilisation. Satellites are used for civilian, military, and scientific applications and are involved in the everyday activities of most humans. However, most satellites are large, highly complex systems that can cost upwards of $600 million US dollars.

A large portion of satellite expenses comes from launch costs which are on the order of $10,000 US per kilogram lifted into orbit [1], and from costs associated with development and qualification of components. In an attempt to combat the increasing expense of satellites the current trend is moving towards decreased satellite size and use of Commercial-Off-The-Shelf (COTS) components. These smaller satellites are known as micro-satellites and are opening up space to a wider range of users.

1.1 Micro-satellites

While an exact definition for micro-satellites does not yet exist, it is generally accepted that a micro-satellite has a total mass less than 100 kg, total power less than 100 W and maximum dimension less than 1 m [2]. Within the micro-satellite category is a sub-class of interest here called CubeSats. CubeSats are 10 cm cube satellites with a maximum mass of 1.33 kg [3], designed to be constructed from standardised components. The standardised size and mass means CubeSats can be easily deployed into space from a larger mothership using a specially designed de-

ployer [4]. They are also designed to be modular, and can be easily fitted together to form larger satellites if required.

To date, over one hundred CubeSat missions have been launched into space, covering a variety of missions such as technology demonstration, scientific research, communications or simply educating students in the design and build process for satellites [5]. Like all satellites, CubeSats require on-board systems to control attitude (orientation) and orbit altitude. Currently, the majority of CubeSats are launched with no propulsion system on board, using reaction wheels or similar devices to maintain attitude control with uncontrolled orbital decay limiting operational lifetimes. The strict size and weight requirements of CubeSats limit the size and weight of the associated propulsion systems adding complex design challenges. Fittingly, propulsions systems designed for use on CubeSats or other micro-satellites are known as micro-propulsion systems.

1.2 Micro-propulsion

For any vehicle travelling within a vacuum (or near vacuum), thrust is produced by expelling propellant from the spacecraft. To maintain conservation of momentum, the momentum with which the propellant is expelled from the spacecraft must be equal and opposite to the momentum gained by the spacecraft. Assuming the propellant is expelled at a constant velocity (the thermal exhaust velocity (v_{ex})), the resultant thrust (T) is given by Equation 1.1 [6, 7], where $\dot{m}_p$ is the time rate of change of propellant mass on board the spacecraft.

$$T = v_{ex}\dot{m}_p \tag{1.1}$$

Thermal exhaust velocity (v_{ex}) is directly related to the propellant neutral gas temperature (T_g), as shown in Equation 1.2, where k is the Boltzmann constant and M the propellant molecular mass. The higher the gas temperature, the higher the exhaust thermal velocity and the higher the thrust produced.

$$v_{ex} = \sqrt{\frac{8kT_g}{\pi M}} \tag{1.2}$$

Thrust is required by spacecraft for attitude control, orbit boosting or orbital transfers. For orbit boosting and attitude control, short low thrust bursts are re-

quired to generate only small changes in velocity, whereas orbital transfers require higher thrust to sufficiently change the velocity of the spacecraft to reach the new orbit. The change in velocity (Δv) required for any spacecraft manoeuvre is related to v_{ex} and propellant usage through Equation 1.3 where m_0 is the initial mass of the spacecraft including propellant and m_f is the final mass of the spacecraft after the manoeuvre including any leftover propellant [8, 9].

$$\Delta v = v_{ex} \ln(\frac{m_0}{m_f}) \tag{1.3}$$

The specific impulse (I_{sp}) is a measure of how efficiently thrust is produced per unit mass of propellant used. The maximum attainable I_{sp} assuming all propellant exits the thruster with v_{ex} is given by Equation 1.4 where g is acceleration due to gravity.

$$I_{sp} = \frac{T}{\dot{m}g} = \frac{v_{ex}}{g} \tag{1.4}$$

A high specific impulse indicates a high production of thrust per unit mass of propellant, requiring less propellant mass to be carried on board to complete a specific Δv manoeuvre. However, the slower usage of propellant mass requires a longer burn time (t_{burn}), as shown in Equation 1.5.

$$t_{burn} = \frac{m_p}{\dot{m}_p} \tag{1.5}$$

The choice of a propulsion system depends on both the Δv and t_{burn} requirements of the mission. Micro-satellite missions do not carry human life, so t_{burn} is usually a low priority, whereas minimising the propellant mass is a high priority and a high I_{sp} is desirable. A summary of performance values for some micro-propulsion systems potentially suited for CubeSat applications in use or under development is included in Table 1.1, with a summary of the thrusters following in Sections 1.2.1 to 1.2.3.

Cold gas thrusters are the smallest and least complex type of propulsion system, where an inert propellant is simply expelled through a nozzle [10,11]. Thrust produced by small cold gas thrusters suitable for CubeSats varies from μNs to mNs [2], but propellant efficiency is quite low as the gas is cold. Propellant efficiency can be improved by heating the propellant before it is expelled through the nozzle, which can be performed through either chemical or electrical means.

Table 1.1: Performance values for micro-satellite propulsion options

Thruster Type	Propellant	Thrust (mN)	I_{sp} (s)	Power (W)	Efficiency (%)	Refs.
Cold Gas	Nitrogen	0.1-5	45-75	-	-	[2,10,11]
Monopropellant	Hydrazine	1-4450	162-230	-	-	[2,12]
	H_2O_2	1-1.82	100-180	-	-	[13,14]
Solid Rocket	Various	157-325	196-257	-	-	[2,15]
PPT	Teflon	0.01-5	200-1500	2.5-30	-	[1,2,16]
FEEP	Cesium	0.001-1.4	9000	3-93	95	[2]
	Indium	0.001-0.14	2000-8000	1	95+	[17,18]
Colloid	Various	<0.007	300-1500	2	75	[2,19,20]
Mini-Ion	Xenon	0.1-1.553	3000	20-60	45	[9]
Mini-Hall	Xenon	0.1-16	830-1718	50-300	6-34	[2,21]
Hollow Cathode	Xenon	0.0016	85	55	-	[22]
Micro-Plasma	Argon	0.3-0.4	-	15-20	5-20	[23]
Mini-Helicon	Xenon	1	1000	50	20	[24]
	Argon	-	1200	50	-	[25]
Resistojet	Hydrazine	-	300-400	100-1000	65-90	[1,26]
	Water	0.125	127-150	100	-	[2]
	Various	109-335	93-385	167-506	-	[27]
Arcjet	Helium	0.014-0.031	313	119	36	[28]
	Hydrazine	-	345-471	650-1400	29-36	[1,29]
	Ammonia	-	600-900	10^3-10^4	-	[1,26]
	Hydrogen	-	700-1200	10^4	-	[1,26,30]
MET	Argon	0.2-1.4	50-80	6	2-12	[31,32]
	Helium	0.04-0.51	150-270	6	2-12	[33]
RFET	Argon	0.01-0.1	50-85	10-60	-	[34,35]
	Hydrogen	0.1	30000	100	75	[36]

1.2.1 Chemical Propulsion

Chemical propulsion systems are those where the energy produced is stored within the propellant itself, usually in chemical bonds. **Monopropellant rockets** heat the propellant, commonly HAN (Hydroxylammonium Nitrate) or hydrogen peroxide (H_2O_2) through an exothermic breakdown reaction induced by an appropriate catalyst [2, 13, 14]. Monopropellant rockets are usually too large for CubeSat applications, but work investigating microelectromechanical systems (MEMS) techniques to reduce the size and weight is being undertaken [12–14].

Hydrazine monopropellant rockets decompose hydrazine into ammonia and nitrogen, then further decompose the ammonia to nitrogen and hydrogen [2, 12]. The additional energy gained through the decomposition of hydrazine compared to hydrogen peroxide or HAN means significantly higher thrusts can be achieved. However, hydrazine is extremely toxic and flammable increasing cost and risk, and the by-products of hydrazine decomposition are hazardous to the environment.

Solid propellant rockets are widely used for orbit insertion and orbit boosting of larger satellites, but are also usually too large and heavy for CubeSat applications, although a small array of solid rockets suited for micro-satellite applications has been tested giving sub mN thrust and specific impulse of a few seconds [15]. Solid propellant storage is simple but the rockets can only be ignited once. Hybrid rockets allow for reignition and hence multiple burns, but the propellants are required to be kept separate increasing the size and complexity of the complete system [1].

Chemical propulsion systems produce high thrust, but v_{ex} is limited to 5000 m s^{-1} by the energy stored in the chemical bonds [6, 7]. Low v_{ex} gives low I_{sp} which increases the mass of propellant required to be carried on board. Alternatively, the propellant may be heated or accelerated through electrical means in which case the energy of the propellant is controlled by an external source and is not limited by the propellant internal energy storage [1,6]. This results in higher achievable v_{ex} and I_{sp} reducing the fuel required to be carried on board. Conversely, the thrust to power ratio is quite low so thrust from electric propulsion can be orders of magnitude lower than chemical propulsion.

1.2.2 Electric Propulsion

Electric propulsion systems are divided into three categories being electrothermal, electrostatic and electromagnetic. Electrothermal systems use electrical means to directly heat the propellant and will be discussed further in Section 1.2.3. For electrostatic or electromagnetic propulsion, ionised propellant is accelerated by static electric devices or Lorentz forces, respectively.

The first electric propulsion system was a **pulsed plasma thruster (PPT)**, launched in 1964 on the Soviet Zond 2 spacecraft [37]. A PPT contains a solid bar of propellant, usually Teflon [2, 26, 37], held between two electrodes. An electrical discharge across the surface of the Teflon from discharging a capacitor ablates propellant material that is then accelerated by electromagnetic forces. The thrust per pulse is low so PPTs are well suited for precision pointing applications [1].

Field Emission Electric Propulsion (FEEP) devices extract ions from the surface of a liquid propellant using a strong electric field, then accelerate the ions across a potential gradient [1,2]. **Colloid** or **electrospray** thrusters work on similar principles, but use charged droplets formed at the tip of a highly biased needle or capillary from a liquid feed that is not necessarily metallic [1, 2].

The charged propellant may also come from a gaseous discharge rather than extracted from a solid or liquid source. Within a standard **gridded ion thruster**, ions in a gaseous discharge are accelerated using biased grids to speeds in the order of 10^5 to 10^6 m s^{-1} [6] giving an I_{sp} of several thousand seconds. Micro-ion thrusters suitable for CubeSat applications with powers under 100 W and dimensions on the order of centimetres are currently under development [9]. **Hall thrusters** operate with a gaseous discharge created using counterflowing electrons in an annular chamber [26, 38]. The ionised propellant is accelerated by an electric field removing the exposed grids of ion thrusters, somewhat reducing erosion issues. Micro-Hall thrusters suited for CubeSat applications with diameters of a few centimetres operating on 50-300 W are currently being investigated [21].

Both Hall and ion thrusters expel only positive ions in the exhaust plume leading to spacecraft charging problems. To balance the charge and allow the plume to detach from the spacecraft, an external neutraliser is required to inject electrons into the plume, adding weight and complexity to the propulsion system. Commonly,

neutralisers are hollow cathode devices [6] that utilise a heater to emit electrons from a source tube inside a hollow cylindrical cathode. In addition to applications as neutralisers for ion and Hall effect thrusters, hollow cathodes are also being developed directly as thrusters. The Surrey Space Centre have developed a **hollow cathode thruster**, capable of delivering a maximum thrust of 1.6 mN with a specific impulse of 85 s for 55 W power input [22].

The need for a neutraliser is nullified with the use of plasma thrusters that expel equal numbers of electrons and ions leading to a naturally quasi-neutral exhaust plume. A 0.6 mm diameter capillary **micro-plasma thruster** creates an estimated thrust of 0.3-0.4 mN using 20 W input power [23]. **Mini-Helicon thrusters** are a sub-type of micro-plasma thruster with high plasma densities, with expected performance of around 1 mN and 1000 s for less than 50 W power input [25, 39].

1.2.3 Electrothermal Thrusters

As opposed to the electric thrusters discussed in Section 1.2.2 where thrust is produced by ions or other charged particles accelerated through electrical or magnetic means, electrothermal thrusters use electrical means to directly heat the propellant, with thrust produced by the heated neutral propellant expanding through a nozzle.

A **resistojet** supplies heat to the propellant gas by passing it around a heating element or through a tube with heated walls [1,2]. Propellant choices vary and most gases can be used, but superheated decomposed hydrazine is most successful [26,27]. **Arcjets** work on similar principles to resistojets, but gas heating is produced by passing the propellant gas through an electrical arc. The heating then occurs in the gas volume rather than by the walls, increasing gas temperatures significantly by removing any material restrictions on maximum temperature. Propellants used are mostly inert gases [28, 30], although hydrazine has also been investigated [40].

Both resistojets and arcjets require high powers (10^2-10^3 W) to operate, potentially beyond the capabilities of a CubeSat. Power is limited to less than 5 W continuous for a 1U CubeSats by the available solar panel area, although bursts of higher power may be available for short time [41].

Alternatively, low power plasma discharges can be used to heat the propellant. The low power discharge may be created using microwave power [31,32] (**microwave**

electrothermal thrusters (METs)) or radio-frequency power [34, 36] (**radio-frequency electrothermal thrusters (RFETs)**). Performance values for METs and RFETs are similar, giving thrust in the order of mNs and specific impulses up to 85 s for powers less than 10 W using argon.

A radio-frequency electrothermal plasma micro-thruster known as 'Pocket Rocket' [42, 43], under development in the Space Plasma, Power and Propulsion laboratory at The Australian National University, operates on the theory of propellant heating occurring through ion-neutral collisions within the discharge volume. The Pocket Rocket thruster forms the basis for this work and is described in depth in Chapter 2. Firstly though, a complete understanding of propellant heating from ion-neutral collisions within a plasma discharge requires an understanding of base plasma physics, collisional processes and gas dynamics. A summary of the relevant physics follows in Section 1.3.

1.3 Plasma

Plasma is the fourth state of matter, created when additional energy supplied to a gas through thermal or electrical means ionises a non-negligible number of neutral gas particles. To sustain a plasma, there must be a sufficient number of electrons with energy higher than the ionisation potential of the background gas to partially or fully ionise the gas [44].

The charged particles in a plasma discharge interact over relatively long distances through Coulombic forces, making the plasma conductive and controllable using applied electric and magnetic fields. Overall a plasma is quasineutral (equal numbers of positive and negative charges) but small regions of charge imbalance may spontaneously form within the discharge. The scale length over which charge imbalance can exist is called the Debye length (λ_{De}) [38, 45], which is a function of electron temperature (T_e), permittivity of free space (ϵ_0), elementary charge (e) and plasma density (n_0), as shown in Equation 1.6.

$$\lambda_{De} = \sqrt{\frac{\epsilon_0 T_e}{e n_0}} \tag{1.6}$$

The length of the containing volume must be many times larger than the Debye length [44, 45], otherwise charge imbalances and potential gradients form over the

entire volume and charged particles are lost to the wall until charge balance is once again reached.

1.3.1 Plasma Breakdown

Breakdown of a gas into the plasma state can be done electrically in a laboratory environment using an applied electric field. The electric field by itself is usually not strong enough to directly ionise gas particles, but even in a neutral gas there exists a sufficient number of free electrons to initiate a breakdown. Free electrons are accelerated in a direction parallel to the applied electric field gaining energy. Electrons with sufficient energy undergo ionising collisions with neutral particles creating electron-ion pairs.

Newly created electrons drift through the discharge volume potentially undergoing additional ionising collisions, exponentially increasing the electron density (n_e) in a process termed an electron avalanche, represented by Equation 1.7 where n_{e0} is the initial electron population, d is the distance between the electrodes or the size of the container, and λ_i is the average distance between ionising collisions [45, 46].

$$n_e = n_{e0} e^{\frac{d}{\lambda_i}} \tag{1.7}$$

If the applied electric field is direct current (DC), then the electric potential acting to accelerate the electrons is constant and unidirectional. Therefore, each electron has only one pass through the discharge volume as it moves from the cathode to the anode to undergo ionising collisions before being lost to the anode surface. For an alternating current (AC) applied electric field, the electric potential constantly switches polarity and electrons oscillate within the discharge volume making multiple passes through the gas before being lost to the walls or anode, thereby undergoing more ionising collisions [47, 48].

Breakdown in a radio-frequency (RF) field occurs at a specific applied peak voltage known as the breakdown voltage (V_{br}), dependent on both the input power frequency (ω_{rf}) and the pressure-distance (pd) parameter [48,49]. The pd parameter is simply the product of the pressure (p) of the background gas and the characteristic distance of the discharge (d), usually the distance between electrodes, and provides a standardised parameter for breakdown characterisation.

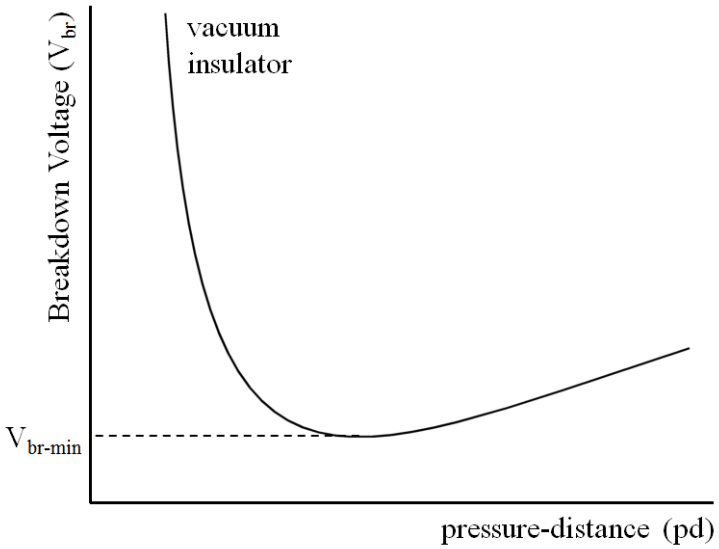

Figure 1.1: A generic Paschen curve showing breakdown voltage with pressure-distance.

For low ω_{rf} or high pd electrons undergo many collisions per oscillation decreasing T_e, therefore a higher V_{br} is required for sufficient ionising collisions. For high ω_{rf} or low pd the gas trends towards becoming a vacuum insulator as electrons undergo many oscillations per collision, and V_{br} heads to infinity at a critical value [46,48,49]. A curve of V_{br} with pd is known as a Paschen curve, a generic example of which is shown in Figure 1.1. The minimum point on the curve corresponds to the minimum V_{br} achievable for the gas.

1.3.2 Plasma Sheaths

Ions formed during breakdown are accelerated by the external field in the opposite direction to the electrons, and at a much slower rate as ion thermal velocity is around 100 times lower than electron thermal velocity [45]. During the initial stages of breakdown, an influx of electrons lost to the walls occurs before the slower moving ions reach the walls, creating a region of positive space charge in the plasma bulk separated from the walls by sheaths. A sheath is a sharp potential drop over a relatively small physical space that acts to retain electrons in the main plasma bulk and accelerate ions towards the walls. Once sheaths are established, the plasma bulk sits at a positive potential known as the plasma potential (V_p), with a region called the presheath separating the main bulk and the wall sheath. The plasma potential

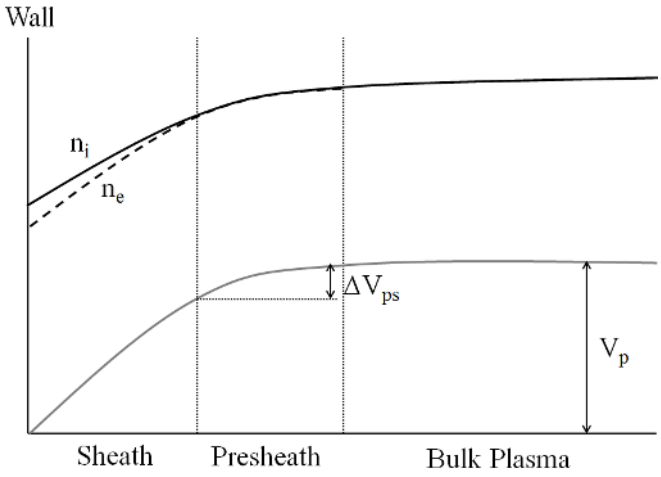

Figure 1.2: Generic example of potential gradient, and electron and ion densities within the sheath, presheath and bulk plasma.

remains at a constant value by the sheath maintaining equal fluxes of electrons and ions to the walls. A generic example of potential gradient, and electron and ion densities within the sheath, presheath and plasma bulk is shown in Figure 1.2.

Ion density (n_i) within the sheath is higher than n_e as shown in Figure 1.2, with quasineutrality returning at the presheath boundary. Lower n_e in the sheath makes the region appear dark as excitation collisions from electrons occur less frequently than in the main bulk [50]. Despite n_i being greater than n_e in the sheath region, the electrons are moving significantly faster and to maintain a stable sheath to allow equal fluxes of ions and electrons to the wall ions must enter the sheath region at a specific velocity. This is known as the Bohm velocity (v_B) [38, 45, 46], given by Equation 1.8 where M_i is the ion mass. Complete derivation of v_B is widely available (in [38, 45] for example) so not included here.

$$v_B = \sqrt{\frac{eT_e}{M_i}} \tag{1.8}$$

The potential in the main plasma bulk changes slowly and can be assumed to have a scale length approximately equal to the size of the containing vessel [46]. Ions in the main bulk are therefore relatively static and an additional region of potential change must exist acting to give the ions the required directed velocity to reach v_B at the sheath edge. This is the presheath region, shown in Figure 1.2, and it carries a potential drop of $\Delta V_{ps} = \frac{T_e}{2}$ [45].

The Child law sheath thickness approximation (Equation 1.9) can be used as an

estimate for average sheath thickness (s), where λ_{Ds} and V_0 are the Debye length and potential at the sheath edge, respectively [45].

$$s = \frac{\sqrt{2}}{3}\lambda_{Ds}(\frac{2V_0}{T_e})^{\frac{3}{4}} \tag{1.9}$$

Sheaths are usually a few Debye lengths thick, as λ_{De} gives an indication of the distances that a potential gradient can exist within a plasma.

1.3.3 Secondary Electrons

Ions accelerated through the sheath regions impact on the wall surface and may release a secondary electron into the discharge through the Auger process [51]. The charged nucleus of an ion approaching within atomic distances to the wall deforms the surface potential well into a passable potential barrier and an electron is released to neutralise the ion. If the excess energy from neutralisation is higher than the workfunction of the surface an additional or secondary electron may also be released [46, 51]. The secondary electron emission coefficient (γ) gives an indication of the number of electrons emitted per incident ion. Metastable atoms may also release secondary electrons through a similar process by the atom becoming ionised near the surface [46].

The emitted secondary electron is accelerated by the sheath back into the main plasma bulk reaching high energies, potentially well above the ionisation potential of the discharge gas. In a direct current (DC) discharge, secondary electrons are required to sustain the plasma as electrons pass only once from the cathode to the anode, and the number of secondary electrons emitted must be sufficient to balance the electrons lost to the anode to maintain population levels in the bulk. In an AC discharge with frequency sufficient to trap electrons through oscillations in the bulk region, secondary electrons are not as important but can play an important role in discharge parameters, and there have been reported cases where a radio-frequency (RF) discharge cannot be maintained without secondary electrons [52].

1.3.4 Capacitively Coupled Plasmas

Power coupling to the discharge gas from RF sources in low pressure discharges occurs through three different modes. These are the capacitively coupled (electro-

static - E) mode, inductive (evanescent electromagnetic - H) mode, and the Helicon (propagating wave - W) mode [38, 45, 53]. Each successive mode achieves slightly higher power deposition and plasma density compared to the previous.

The capacitively coupled plasma (CCP) has a powered electrode immersed directly within the discharge, sometimes covered with a dielectric material, developing large sheath potentials oscillating with the same frequency as the applied power. The oscillation of the sheath potentials deposit power into the plasma by accelerating the electrons. The CCP mode has two additional sub-modes, being the α and γ modes, where the main ionisation is from bulk electrons and secondary electrons, respectively [54, 55]. Heating in a CCP occurs through both Ohmic and stochastic processes. Ohmic heating comes from collisions between electrons and heavy background gas particles within the discharge [38, 54]. Stochastic heating comes from moving sheaths imparting energy to the electrons [38, 45].

The sheath regions in a CCP act like capacitors, so a sheath at the RF electrode and a sheath at the grounded electrode can be thought of as two capacitors in series with capacitances C_{rf} and C_g, respectively [56]. The voltage (V) distribution between the two sheaths is given by Equation 1.10 where S is the maximum sheath width and A is the electrode area.

$$\frac{V_{rf}}{V_g} = \frac{C_g}{C_{rf}} = \frac{A_g S_{rf}}{A_{rf} S_g} \tag{1.10}$$

Usually, S_{rf} is bigger than S_g, so if A_g is bigger than A_{rf} then V_{rf} is significantly larger than V_g and a blocking capacitor placed in the circuit prior to the RF electrode will charge to give a negative DC self-bias at the RF electrode. The self-bias forms during breakdown as an influx of electrons to the electrode surface occurs before the positive space charge and sheaths develop. Electrons lost to the powered electrode during this period contribute to negatively charging the blocking capacitor [56].

A dielectric material capable of carrying a capacitance placed between the powered electrode and the plasma may also carry a DC self-bias. A voltage applied to the powered electrode induces a response voltage (V_r) on the surface of the dielectric exposed to the plasma. When V_r is positive an electron current flows readily to the dielectric surface while little or no ion current flows. However, as the dielectric acts as an insulator, there must be equal fluxes of ions and electrons to the surface, and V_r must sit at an average negative value [50].

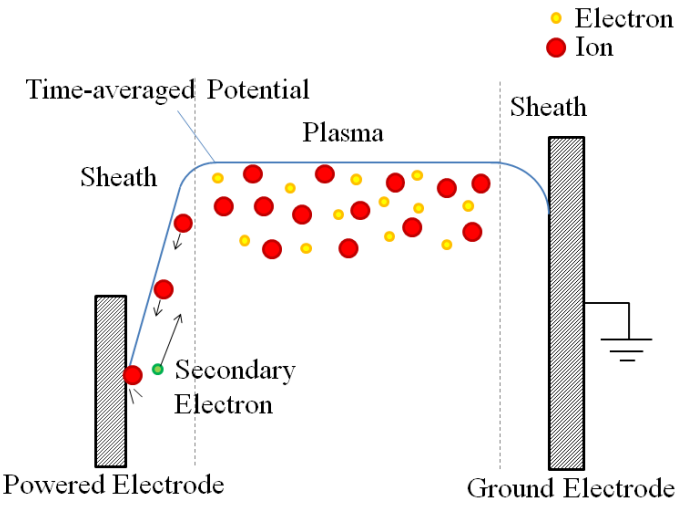

Figure 1.3: General features of an asymmetric CCP showing self-bias, asymmetric sheath potentials and secondary electron emission.

The negative DC self-bias developed on the dielectric insert must be smaller in magnitude than the peak RF voltage to allow the sheath to collapse once per RF cycle. Ions are lost to the walls throughout the entire RF cycle, whereas electrons are only lost if the sheath potential near the wall collapses to near zero. To balance the number of positive and negative charges within the discharge, the sheath must collapse once per cycle to allow a sufficient number of electrons to be lost to the walls to maintain quasineutrality [45, 56, 57].

An example asymmetric CCP is given in Figure 1.3. The asymmetric sheath potentials from a negative self-bias on the powered electrode are clearly shown. Secondary electron emission from ion bombardment of the powered electrode surface is also demonstrated.

1.3.5 Global Modelling

For a plasma to be in a steady state condition, the number of charged particles lost to the walls must balance the volume production of charged particles through ionisation. This provides the basis for a global or zero dimensional model of a plasma accounting for energy and particle conservation. Particle conservation is represented by Equation 1.11 [45, 46]. The left hand side (LHS) of Equation 1.11 represents volumetric ionisation with ionisation rate $K_{iz}(T_e)$ of a background neutral population with density n_g, by electrons with density n_e in an effective volume V_{eff}.

The right hand side (RHS) of Equation 1.11 represents walls losses through the effective surface area A_{eff} assuming ions are travelling at the Bohm velocity (v_B).

$$K_{iz}(T_e)n_g n_e V_{eff} = n_e v_B(T_e) A_{eff} \tag{1.11}$$

Effective volume and area depend on the plasma density profile. For a high pressure CCP (>100 mTorr) the density profile is approximately sinusoidal [45] and V_{eff} and A_{eff} can be approximated using the length correction factor (h) given in Equation 1.12, where l is length (or radius) of the plasma volume and ν_i is the ionisation collision frequency.

$$h = \frac{\pi v_B}{l\nu_i} \tag{1.12}$$

Both K_{iz} and v_B are functions of T_e, so an iterative procedure to scan through values of T_e until the LHS and RHS of Equation 1.11 are equal gives an estimate for T_e. Once T_e is known, a power balance accounting for energy within the discharge gives an estimate for plasma density (n_0) using Equation 1.13, where the LHS is power input to the discharge from an external source (P_{in}) and the RHS is energy losses from processes within the discharge [45, 46].

$$P_{in} = n_0 e v_B(T_e) A_{eff}[\epsilon_c(T_e) + \epsilon_s(T_e) + 2T_e] \tag{1.13}$$

Energy loss related to collisions, both ionisation and excitation, is given by $\epsilon_c(T_e)$, energy lost to the walls though ion bombardment is given by $\epsilon_s(T_e)$, and energy lost during electron collisions with walls is equivalent to the electron thermal energy ($2T_e$). For a low voltage sheath, $\epsilon_s(T_e) \approx 5kT_e$ (the plasma potential) but for a high voltage sheath or in the presence of a negative DC self-bias, $\epsilon_s(T_e)$ is much higher and becomes the dominant energy loss mechanism [45].

1.3.6 Gas Discharge Collisional Processes

Within the main plasma bulk collisions between particles both sustain and heat the discharge and are paramount to plasma physics. Collisional processes within a gas discharge may be elastic, inelastic or superelastic. During an elastic collision potential energy does not change and kinetic energy is conserved. An elastic collision between two particles of the same mass will result in about half the kinetic energy being transferred on average. During an inelastic collision a transfer between kinetic

energy and potential energy occurs and one particle enters an excited or ionised state. Inelastic collisions only occur if the energy of the incoming particle exceeds the first excitation potential. A superelastic collision results in a transfer from potential energy to kinetic energy during de-excitation of a particle.

The collisional cross-section (σ) is the area within which two particles will interact. For neutral-neutral collisions σ can be approximated simply as a hard body sphere cross section and is independent of particle velocity (energy). For collisions involving charged particles the electric field of the charged particle temporarily changes the electronic configuration of the neutral by attracting or repelling the electron cloud, forming a temporary dipole acting to increase the attraction between the particles. The effect of the electric field is dependent on the velocity of the charged particle and σ is dependent on particle energy.

The mean free path (λ_{mfp}) is a measure of the distances a particle will travel before the uncollided flux drops to $\frac{1}{e}$, and is given by Equation 1.14 for charged particle collisions, where n_g is neutral gas particle density [45]. For neutral-neutral collisions, a factor of $\frac{1}{4}$ must be included on the RHS of Equation 1.14 to account for the size of the colliding particles [46]. The mean time between collisions (τ_c) is given by Equation 1.15 where $\bar{v}$ is the average particle velocity.

$$\lambda_{mfp} = \frac{1}{\sigma n_g} \tag{1.14}$$

$$\tau = \frac{\lambda_{mfp}}{\bar{v}} \tag{1.15}$$

Of particular interest in this work are ion-neutral momentum transfer collisions, and ion-neutral charge exchange (I-N CEX) collisions that occur when an ion passes sufficiently close to a neutral atom for a valance electron to be transferred from the neutral to the ion. If this occurs with no change in particle kinetic energy the collision results in a slow ion and a fast neutral. For a discharge volume where the ion-neutral mean free path is much smaller than the containing vessel scale length, a significant population of hot neutral atoms is generated. The hot neutrals have higher velocities than the cold neutral population and may accelerate in the direction of plasma flow leaving a depleted neutral population in the main bulk in a process termed 'neutral pumping' [58, 59]. Thermalising collisions between the hot and cold neutral atom populations increases neutral gas temperature, and in an open ended

plasma source, the flow of hot neutrals increases the momentum of the neutral jet expelled from the source [60], making a device based on these principles a viable electrothermal plasma micro-thruster.

1.4 Thesis Scope

The Pocket Rocket device under development at the Australian National University (ANU) is an electrothermal plasma micro-thruster concept based around neutral gas heating from ion-neutral collisions and is described in depth in Chapter 2. This thesis focusses on the use of experimental and computational techniques as outlined in Chapter 3 to investigate the underlying physical mechanisms of the Pocket Rocket device, especially in regards to neutral gas heating.

Direct experimental measurements of neutral gas temperature are made and discussed in Chapter 4, successfully demonstrating proof of concept for the device. Basic estimates for performance (thrust, specific impulse and efficiency) are made using the measured temperatures to compare with other micro-propulsion devices discussed in Section 1.2. Direct measurement of thrust using a thrust balance or similar device is not included here due to engineering challenges associated with the early experimental design of the Pocket Rocket device.

Spatiotemporal profiles of neutral gas heating in Pocket Rocket are given in Chapter 5, identifying the various gas heating mechanisms involved. Computational Fluid Dynamics (CFD) simulations complement the spectroscopy experiments and are presented in Chapter 6. A preliminary simulation of the Pocket Rocket device operating under standard conditions is initially performed with results compared to previous experimental results where possible for validation. Extension simulations investigating the role of secondary electrons and pressure gradient are then performed to further investigate the application of Pocket Rocket as an electrothermal plasma micro-thruster without the need to adapt the physical experimental device.

Outcomes of this work are demonstrating proof of concept for the Pocket Rocket device and enhancing the understanding of gas heating mechanisms in electrothermal plasma devices. Results can be used in the further development of a flight ready Pocket Rocket prototype, or applied to similar electrothermal devices.

Chapter 2

Apparatus and Diagnostics

An electrothermal plasma micro-thruster device being developed at the Australian National University, known as 'Pocket Rocket' [42, 43] and described completely in Sections 2.1 to 2.3 forms the basis for this work. The Pocket Rocket device has been designed for operation with small satellites, including CubeSats, and must therefore be small, lightweight and low power. As this work does not include the development of a self-contained, fully developed flight prototype, many of the components used during experiments are not suited for satellite operation. However, the setup provides the opportunity to study the Pocket Rocket device using multiple experimental techniques, and gain a better understanding of the operation and physics behind the thruster.

2.1 The Pocket Rocket Device

The Pocket Rocket device, shown in Figure 2.1, consists of an 18-20 mm long, 4.2 mm inner diameter, 6.3 mm outer diameter alumina tube. A 5 mm wide, 12 mm diameter, annular copper powered electrode surrounds the alumina tube at the midpoint, creating an asymmetric weakly ionised ($< 1\%$) capacitively coupled plasma (CCP) inside the tube. Two 3 mm wide sections of the 60 mm outer diameter grounded aluminium thruster housing contact the alumina tube at either end, acting as the grounded electrodes to complete the circuit.

The powered and grounded electrodes are separated by 3 mm on the downstream side and 4 mm on the upstream side, with electrical insulation provided by a 15 mm

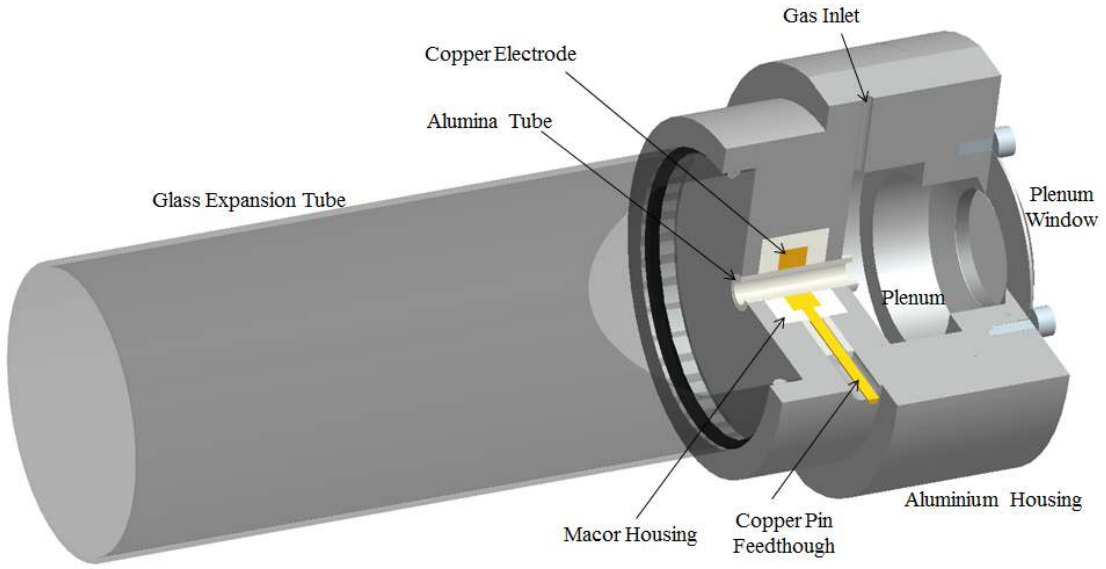

Figure 2.1: The Pocket Rocket device with section cutaway showing electrode detail.

diameter two part Macor housing encasing the powered electrode. Downstream, the grounded electrode has a large exposed surface normal to the alumina tube with a diameter of 50 mm, referred to as the end plate of the device. Upstream, the grounded electrode has an exposed surface normal to the alumina tube with 40 mm diameter and acts as one wall of an upstream plenum chamber.

The plenum chamber is 12 mm deep, with 40 mm inner diameter, 70 mm outer diameter and grounded aluminium walls. When the 20 mm long alumina tube is used, the tube protrudes 2 mm upstream of the thruster housing and electrodes, into the plenum chamber. Operating gas, or the propellant, is introduced to the system through a 2 mm hole on the side of the plenum chamber. A pressure gauge, either a Granville Phillips Convectron gauge for the work in Chapter 4, or an MKS 10 Torr Baratron gauge for the work in Chapter 5, connects to the plenum chamber through a similar 2 mm hole directly opposite the gas inlet. The rear wall of the plenum chamber contains a 20 mm diameter quartz window providing axial optical access to the discharge inside the alumina tube. The window may also be removed, leaving a 30 mm diameter probe access port.

Argon (Ar) [42, 43, 61], nitrogen (N_2) [62–64], hydrogen (H_2) [65, 66] or carbon dioxide (CO_2) may be used as the propellant, with Ar and N_2 the main operating gases used throughout this work. Gas flow into the plenum is through a series of

external plastic and metallic pipes, with flow rates controlled by a either a ball valve, leak valve, 100 sccm MKS flow controller or 500 sccm MKS flow controller, depending on the particular experiment. Both MKS flow controllers are calibrated for N_2 and are controlled by an MKS type 247 four channel readout device, with separate channels calibrated for Ar and N_2.

2.2 Power System and Matching Network

Radio-frequency (RF) power at 13.56 MHz is coupled to the Pocket Rocket discharge through the annular copper powered electrode. Power is produced by an ENI OEM-25 RF generator with 3000 W maximum output power and 50 Ω output impedance for the work in Chapter 4, or an ENI ACG-10 RF generator with maximum output power of 1200 W and 50 Ω output impedance for the work in Chapter 5. Standard operational power is 10 W (generator output), but for experiments powers used range from 5 W to 60 W as required to suit the experimental application.

The use of RF power introduces complexities into the system in regards to impedance matching. The RF generator and all cables used for connecting components are designed with 50 Ω impedance. However, the impedance of a typical laboratory plasma varies widely and an intermediate electrical component known as a matching network must be placed between the generator and Pocket Rocket to make the discharge and matching network combine to give a 50 Ω total impedance. For this work, a π-matching network consisting of four capacitors (two variable and two fixed capacitance) and a hand wound inductor, with schematic shown in Figure 2.2(a), matches the impedance of the plasma to the 50 Ω impedance of the generator and cables.

The load capacitor (C_{load}) is a MEIVAC 0-1000 pF variable vacuum capacitor placed in parallel with a 500 pF fixed capacitor, and the tune capacitor (C_{tune}) is a MEIVAC 0-500 pF variable vacuum capacitor. The hand wound inductor is constructed of 5 mm thick copper wire wound into 4.25 loops with 75 mm diameter and a total length of 85 mm.

A 100 pF bias capacitor (C_{bias}) placed between the output of the matching network and the plasma, protects the power system from any direct current (DC) self-

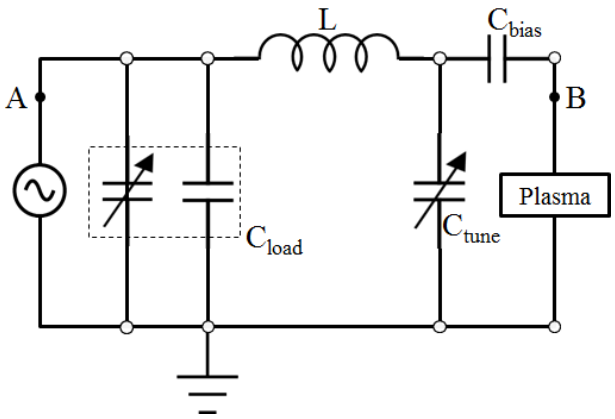

(a)

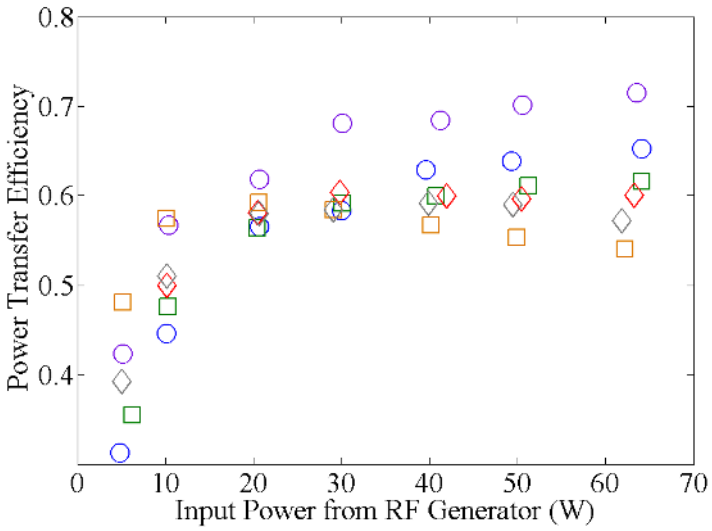

(b)

Figure 2.2: Impedance matching network: (a) circuit diagram of the π-matching network used to match Pocket Rocket to the 50 Ω generator including the locations of two Impedans Octiv probes to measure current and voltage at A and B, and (b) power transfer efficiency through the matching network for N_2 at 4.0 Torr (blue circles), 1.5 Torr (green squares) and 0.5 Torr (red diamonds), and argon at 4.0 Torr (purple circles), 1.5 Torr (orange squares) and 0.5 Torr (grey diamonds).

bias that develops. The Pocket Rocket device is highly asymmetric, with a powered electrode area of ∼1 cm^2 compared to a grounded electrode area encompassing the ground electrode surfaces in contact with the alumina tube, the grounded plenum walls and the grounded end plate of ∼58 cm^2. As discussed in Section 1.3.4, an asymmetric CCP will develop a DC self-bias, and while the dielectric alumina tube carries some of the DC self-bias, the bias capacitor is included for additional protection. This is especially relevant at higher applied voltages when the dielectric tube cannot carry the entire DC self-bias.

Prior to the matching system a Daiwa CN-801 standing wave ratio (SWR) meter inserted in series into the circuit measures the ratio of the forward to reflected power, as a guide to the effectiveness of the match. The SWR is expressed as shown in Equation 2.1 in terms of forward power (P_f) and reflected power (P_r). The closer the SWR value is to 1, the higher the ratio of forward to reflected power, the more effective the match and the better the power transfer is through the matching network and plasma load. Throughout this work, unless otherwise stated, the SWR is less than or equal to 1.2.

$$SWR = \frac{1 + \sqrt{P_r/P_f}}{1 - \sqrt{P_r/P_f}} \tag{2.1}$$

Power transfer efficiency through the matching network for various operating conditions is shown in Figure 2.2(b), measured using two Impedans Octiv 13.56 MHz probes inserted in series into the circuit. One Octiv probe was positioned pre-match (position A in Figure 2.2(a)) and the other positioned post-match (position B in Figure 2.2(a)), to simultaneously measure the power before and after the matching network during operation. For power inputs from the generator of 20 W or higher, power transfer efficiency is approximately 60%, decreasing to 40% for lower input powers down to 5 W. All powers stated in this work represent the forward power measured pre-match at position A.

Post match, an Impedans Octiv 13.56 MHz probe inserted in series into the circuit measures post-match power, current (I_{rms}) and voltage (V_{rms}). Power is fed into the vacuum chamber through a hermetically sealed SMA connector, located at the bottom of the Pocket Rocket housing, in line with the location of the powered electrode. Input power is transferred from the SMA connector into the powered electrode through a specially made copper pin, with approximate dimensions of 3 mm

diameter and 20 mm length. The pin sits within a hole drilled into the aluminium and Macor housings (see Figure 2.1), protected from the grounded housing by a thin sleeve of alumina tubing. One end of the pin is inserted into the female side of the SMA connector and the other end screws into the powered copper electrode.

Within the Pocket Rocket device, the dielectric alumina tube acts as a capacitor and carries at least some of the DC self-bias that develops [43, 61]. The weakly ionised discharge, without considering the annular geometry, constitutes an equivalent electrical circuit comprising a capacitance from the powered electrode sheath, a resistance from the main plasma bulk and another capacitance from the grounded electrode sheath.

2.3 Vacuum Chamber

As previously discussed in Section 1.3.1, the voltage required to initiate breakdown of a gas discharge depends on the operating gas, gas pressure (p) and inter-electrode or characteristic distance (d). Each gas will have a minimum breakdown voltage at a particular pressure-distance (pd), regardless of the other operating parameters. Paschen curves for Pocket Rocket discharges for Ar, N_2, and CO_2, determined by recording the post-match voltage required for breakdown for various operating conditions, measured using an Octiv probe, are shown in Figure 2.3. Using the diameter of the Pocket Rocket tube (4.2 mm) as the characteristic distance, this gives minimum breakdown voltages, hence standard operating pressures, of 1.2 Torr for CO_2, 1.5 Torr for Ar and around 2.5 Torr for N_2.

To achieve the required sub-atmospheric pressures for operation, a six way cross vacuum chamber with 200 mm diameter arms, fitted with a 40 m^3 hr^{-1} flow rate rotary pump is used. The Pocket Rocket device connects to the left arm of the chamber using the 50 mm diameter, 700 mm long glass tube to allow optical access to the exhaust plume. The complete experimental setup including vacuum chamber, Pocket Rocket, gas feed and power systems is shown in Figure 2.4.

Base pressures within the vacuum chamber are on the order of 10^{-3} Torr, measured using a Granville Phillips Convectron gauge mounted on the right arm of the vacuum chamber for the work presented in Chapter 4, or an MKS 20 Torr Bara-

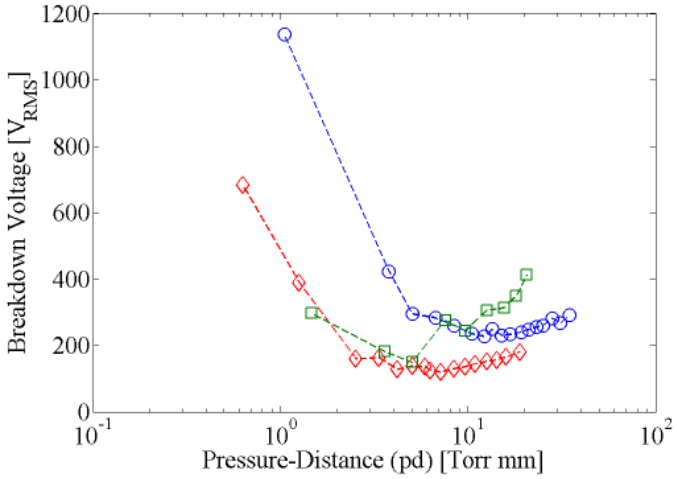

Figure 2.3: Paschen Curves for Pocket Rocket showing argon (red diamonds), N_2 (blue circles), and CO_2 (green squares).

tron gauge mounted on the rear arm of the vacuum chamber for works presented in Chapter 5. During operation of the Pocket Rocket device, the pressure gradient between the plenum chamber and vacuum chamber is between two and four for all operating conditions used.

2.3.1 Pressure Gradient and Choked Flow Criterion

As an electrothermal thruster operating in space, Pocket Rocket will be subjected to significantly higher pressure gradients, with background pressures around 10^{-10} to 10^{-8} Torr in low earth orbit (LEO) giving pressure gradients between 10^8 to 10^{10}. However, as an electrothermal thruster Pocket Rocket operates on the principle of neutral gas flow through a tube expanding into a lower pressure volume. The gas starts in an effective near stagnant state in the plenum with pressure p_{pl}, and accelerates through the discharge tube to expand into the downstream glass tube with background pressure p_{ex}. When the pressure ratio $\frac{p_{pl}}{p_{ex}}$ reaches a critical value given in Equation 2.2, the flow will reach Mach 1 at the tube exit and become choked [67].

$$\frac{p_{pl}}{p_{ex}} = (\frac{\gamma+1}{2})^{\frac{\gamma}{\gamma-1}} \tag{2.2}$$

For all gases the choked flow criterion is reached for values of $\frac{p_{pl}}{p_{ex}}$ less than 2.1 [67], after which the pressure at the tube exit becomes independent of the pressure in the expansion chamber (p_{ex}). Therefore, for pressure gradients higher than approxi-

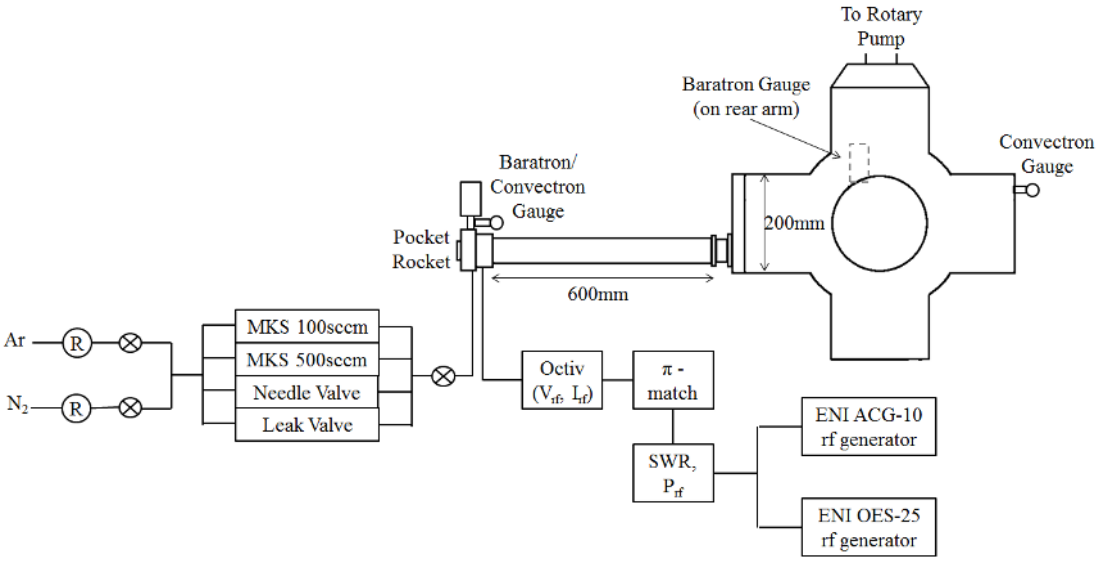

Figure 2.4: Complete experimental setup of the Pocket Rocket apparatus including external power and gas systems

mately 2, the gas flow within the Pocket Rocket discharge tube is unlikely to change significantly, and the preliminary experiments presented here can be performed without the need to introduce additional complexities and costs to the vacuum chamber setup described above by adding a higher pumping capacity.

The flow becoming choked at the exit of the discharge tube makes Pocket Rocket naturally act similar to a de Laval nozzle, where flow converges through a narrow section (the discharge tube) to reach Mach 1 at the throat (the discharge tube exit), before expanding into a divergent section (the expansion tube). In the preliminary experimental design state, as outlined above, the geometric properties of Pocket Rocket in respect to nozzles is completely unoptimised, as noted by the sharp right angle corners on the discharge tube inlet and outlet. For this work, the effects of a nozzle are not important as the focus is on the underlying plasma physics within the discharge tube and not the overall performance of the device as a thruster. For future prototype development, addition of shaped converging and diverging nozzle sections and optimisation of tube length will need to be considered.

Chapter 3

Diagnostics

Understanding main discharge parameters such as plasma potential (V_p), electron temperature (T_e) and plasma density (n_0), is essential to characterise the discharge for any plasma application. For Pocket Rocket, with its application as an electrothermal thruster, it is also important to understand the background neutral flow parameters such as velocity (v) and neutral gas temperature (T_g). To gain an understanding of both the discharge and flow properties within Pocket Rocket, a combination of experimental and computational diagnostic techniques is used.

Experimental diagnostics for discharges are either invasive, where a diagnostic tool is placed directly into the discharge, or non-invasive, where measurements are made remotely without perturbing the discharge. For this work, the majority of experiments are performed using non-invasive optical techniques outlined in Sections 3.2 and 3.3 with simplistic invasive probe experiments also performed as required, outlined in Section 3.1. To complement the experimental diagnostics with a computational diagnostic, Computational Fluid Dynamics (CFD) simulations are also used and are discussed in Section 3.4.

3.1 Langmuir Probe

Electric probes have been used for laboratory plasma diagnostics since the 1920s [68] and a variety of probes now exist to study different plasma parameters. Emissive probes measure plasma potential [38,69] with a resolution around 0.2 eV [70], Langmuir probes can measure V_p, T_e, electron density (n_e), ion density (n_i) and the

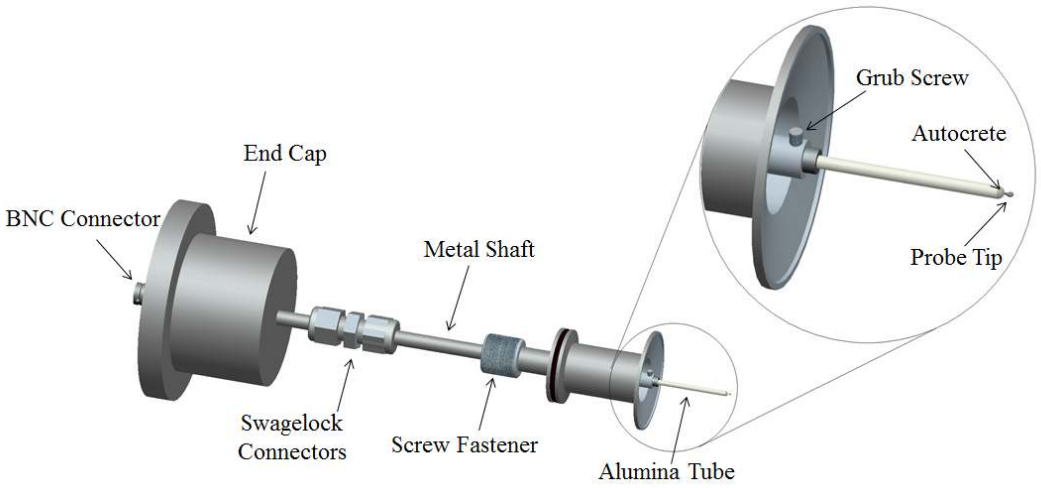

Figure 3.1: Langmuir Probe used for Pocket Rocket diagnostics

electron energy distribution function (EEDF) [45, 71, 72], and more advanced probe configurations such as the retarding field energy analyser (RFEA) measure directed current and infer energy distribution, n_0 and local V_p [73, 74].

Only Langmuir probe diagnostics are used in this work. Langmuir probes consist of a metal wire, disk or ball inserted into the discharge that may be biased with an electric potential [45, 71]. A biased probe tip will draw a current from either ions or electrons (depending on applied bias voltage), from which V_p, T_e, n_e, n_i and the EEDF can be inferred. When unbiased, the probe tip floats to the floating potential, such that no net current is drawn by the probe tip.

The Langmuir Probe used in Pocket Rocket is shown in Figure 3.1. The end cap provides the termination point for internal probe wiring, with a vacuum BNC connection fitted to allow bias voltages to be applied to the tip and the collected signal returned to an external reading device (multimeter or oscilloscope). The end cap connects to the metal shaft, passing through the vacuum feed-through, designed to be installed in place of the rear plenum viewport, allowing the probe to be inserted and moved axially down the alumina tube of Pocket Rocket, without needing to break vacuum.

The probe head is a planar disc with 1 mm diameter, separated from the metal shaft by a 30 mm long, 2 mm diameter alumina tube. The probe tip protrudes from the end of the alumina tube, held in place by Autocrete high temperature vacuum safe ceramic paste, which also provides a seal against plasma entering the

shaft of the probe and perturbing the measurements. The alumina tube is inserted telescopically inside the metal shaft, held in place by a small grub screw and sealed with Autocrete, and provides an electrical separation between the grounded shaft and the probe tip. For all measurements in this work, the probe is inserted through the plenum probe port such that the probe tip lies on the central axis of the device, at the axial midpoint of the tube in line with the centre of the powered electrode.

The plasma density is measured by applying a negative bias greater than the floating potential to the Langmuir probe tip using a series of 9 V batteries, such that probe tip collects positive ions but repels any negatively charged electrons. The resulting net current, measured using the voltage drop across a 10 kΩ resistor, is the ion saturation current (I_{sat}). For a 1D planar probe, I_{sat} is related to n_i through Equation 3.1 [75–77], where v_b is the Bohm velocity and A_s is the collecting area of the probe including the sheath. The constant 0.368 is to account for the shape of a 1D planar probe presheath [77].

$$I_{sat} = 0.368 e n_i A_s v_b \tag{3.1}$$

Further probe measurements of the Pocket Rocket discharge are not feasible as the small diameter of Pocket Rocket combined with the invasive nature of Langmuir probes results in plasma perturbation and flow constriction, and restricts the use of RF compensation [78, 79]. Instead, non-invasive optical techniques are used for further measurements.

3.2 Optical Emission Spectroscopy

Plasma discharges are naturally luminous, which means non-invasive emission spectroscopy diagnostics are a powerful tool for analysing plasma discharges. The light emitted from a plasma arises from the continual excitation and de-excitation of electrons to different electrical levels within the discharge atoms. Within an atom, electrons are confined to orbitals defined by a wavefunction ψ, which is essentially a probability function, and are therefore restricted to orbitals that form a standing wave around the nucleus. Otherwise, over successive electron orbits, the wavefunction goes to zero at every point, the probability of finding the electron anywhere goes to zero and the orbital cannot exist.

The wavefunctions of electron orbitals are eigenfunctions found through solving the time independent Schrödinger equation [80], given in Equation 3.2.

$$H\psi = E\psi \tag{3.2}$$

The Hamiltonian (H), defines the total energy of the electron. The eigenvalues of the wavefunction (E), are the allowed energy levels of orbitals, with each orbital (with wavefunction ψ) having a single allowed energy.

Transitions between any two orbitals with E' and E'' (where $E' > E''$) will correspond to a discrete energy difference given by $\Delta E = E' - E''$. For an electron to move to a higher energy orbit, energy equal to ΔE must be absorbed. This energy may be gained through collisions or photon absorption. Absorption spectroscopy uses this principle, where a laser is tuned to a specific energy to excite a certain transition within a particle for the study of a resulting excited state [81, 82].

Conversely, emission spectroscopy utilises naturally occurring photon emission from an electron in an upper or excited state spontaneously returning to a lower state. During this transition, a photon with energy exactly equal to ΔE is emitted. From Planck's law, $E = h\nu$, and the frequency (hence wavelength) of the emitted radiation is constant for a particular transition, as given by Equation 3.3.

$$\frac{1}{\lambda} = \frac{\nu}{c} = \frac{(E' - E'')}{hc} \tag{3.3}$$

The wavelength of the emitted photons are often within the visible spectrum, allowing for optical emission spectroscopy (OES) diagnostics. The simplest OES diagnostics can be performed with just the human eye. Depending on the discharge gas used, light emission will be weighted towards a set range of wavelengths, giving different gases varying colours [46, 83]. For example, argon (Ar) appears purple, nitrogen (N_2) appears orange/pink and carbon dioxide (CO_2) appears violet/blue, as demonstrated by Figures 3.2(a), 3.2(b) and 3.2(c), capturing the Pocket Rocket discharge as viewed through the plenum window for Ar at 10 W and 1.5 Torr, N_2 at 10 W and 2.5 Torr and CO_2 at 20 W and 1.0 Torr.

Sputtering of solid objects within the discharge may also be visible to the naked eye. Figure 3.2(d) shows an argon discharge in Pocket Rocket at 10 W and 1.5 Torr with the alumina tube removed, exposing the copper electrode to the plasma. Sput-

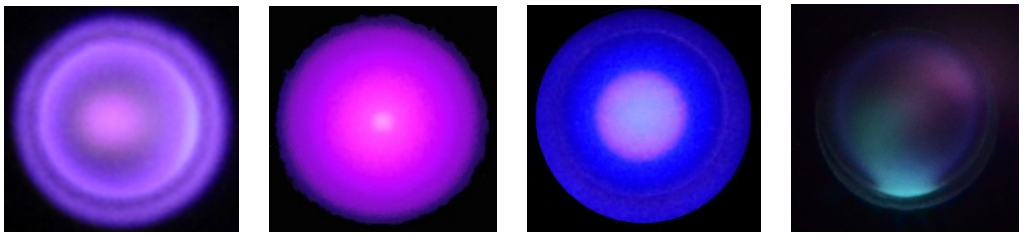

(a) (b) (c) (d)

Figure 3.2: (a) 10 W, 1.5 Torr Argon (b) 10 W, 2.5 Torr N_2 (c), 20W, 1.0 Torr CO_2 and (d) 10 W 1.5 Torr Argon with alumina tube removed displaying copper sputtering.

tering of the copper electrode by the plasma results in a green glow in addition to the purple of argon.

More precise identification of the species within a discharge can be quickly obtained using a spectrometer to record low-resolution spectra over a wide wavelength range. Comparing experimentally observed wavelengths with published values for atomic or molecular transitions, ion and neutral species present within the discharge can be identified. Throughout this work, the *Handbook of Basic Atomic Spectroscopic Data* by Sansonetti and Martin [84] is used for atomic species identification, and *The Identification of Molecular Spectra* by Pearse and Gaydon [85] is used for molecular species identification.

Low resolution spectra are captured using an Ocean Optics QE65000 scientific grade spectrometer, simultaneously recording from 200-990 nm with a resolution of 2 nm. Light enters the spectrometer through a 1 mm diameter fused silica optic fibre, where a collimating mirror directs the light onto a diffraction grating before being focussed by another mirror onto a 24.5 by 1.4 mm charge coupled device (CCD) detector.

Example low resolution spectra captured using the Ocean Optics spectrometer are shown in Figure 3.3 for Ar and N_2. Identification of species using these spectra show that Ar and Ar^+ are present, as are N_2 and N_2^+, but atomic nitrogen (N) is not observed so significant dissociation is not occurring. There are also no aluminium or oxygen species identified demonstrating voltages used are sufficiently low that sputtering of the alumina tube is not significantly occurring. No hydroxyl or oxygen species are present demonstrating there are no significant leaks within the system.

As the discharge emission spectra are not continuous but are comprised of many

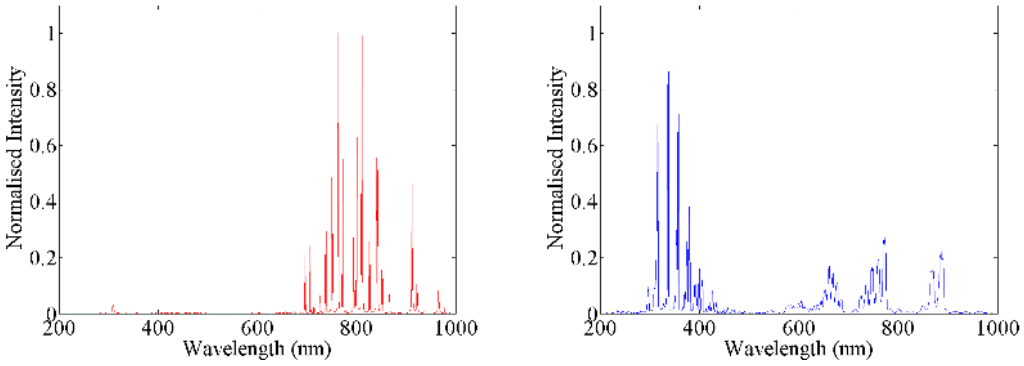

(a) (b)

Figure 3.3: Low resolution, wide band spectra of the Pocket Rocket discharge for (a) argon at 1.5 Torr and 10 W and (b) N_2 at 1.5 Torr and 10 W.

discrete transition lines, a single transition can be isolated for further analysis using a bandpass filter. Using the simple coronal model, which is based on the low electron density (n_e), high electron temperature (T_e) non-equilibrium (low temperature) plasma found in the solar corona, it can be assumed excitation only occurs through electron impact (due to high T_e) and de-excitation is only through spontaneous radiative decay (due to low n_e for collisional de-excitation) [83]. Given these assumptions, the intensity (I) of light emission from a plasma is proportional to neutral gas density (n_g), n_e, and a function of T_e and σ ($f(T_e, \sigma)$), as shown in Equation 3.4. For a quasi-steady state plasma, n_g, T_e and σ can be assumed constant, and I is directly related to n_e.

$$I \propto n_g n_e f(T_e, \sigma) \tag{3.4}$$

Placing an optical bandpass filter between the emitting discharge and a standard digital camera captures a 2D map of the intensity of an isolated emission line. The intensity is proportional to n_e if a neutral species transition is imaged, or ${n_e}^2$ for imaging of a singly ionised species transition, essentially giving a 2D map indicating qualitative electron density variation. It is possible to calibrate the recorded intensity against a known light source to give quantitative electron density data, but in this work the technique is used only to give qualitative indications of spatial electron density variation (see Section 4.2), hence calibration is not performed.

3.3 Rovibrational Spectroscopy

For application of Pocket Rocket as an electrothermal thruster, the main focus of this work is to measure the neutral gas temperature. A metallic thermocouple placed directly into the discharge will perturb the plasma, forming sheaths and producing extraneous currents within the thermocouple system that will affect the results and make them unreliable. Instead, a non-invasive advanced branch of OES known as rovibrational spectroscopy is used.

Rovibrational spectroscopy focuses on the study of diatomic or molecular species with excited rotational and vibrational states. Rotational and vibrational states within a molecule add additional excitation channels for electrons, and the resulting spectra are quite different from that of an atomic element.

For an atomic element, the difference in electron energy levels depends only on the electronic state of the atom, resulting in a spectrum of sharp narrow peaks. Separation of electronic energy levels is of the order of 10^4 J mol^{-1} [86], so successive peaks in most cases do not overlap. A molecular species has multiple rotational modes and one or more vibrational modes, so within an electronic transition the electron may move between different vibrational states, identified by vibrational quantum number (v), and rotational states, identified by rotational quantum number (J), and there is no longer a single well defined energy difference.

Compared to the 10^4 J mol^{-1} of electronic energy level separation, vibrational energy level separation is on the order of 10^3 J mol^{-1} and rotational energy level separation is of the order of 1 J mol^{-1} [86]. So a molecular spectra of a single electronic transition will not be a single well defined peak but will instead consist of a series of moderately spaced vibrational bands, each with a series of tightly spaced rotational bands within it.

3.3.1 Neutral Gas Temperature Estimates

For certain rovibrational band systems, such as the nitrogen second positive and carbon Swann bands, it is possible to simulate the intensity profile of a band using well published equations and constants. The relative intensities of the vibrational and rotational bands are dependent on the distribution of particles within the vi-

brational and rotational states, and hence the vibrational temperature (T_v) and rotational temperature (T_r). So estimates for T_v and T_r of an experimental discharge can be found using rovibrational spectroscopy band fitting, by iteratively comparing experimentally recorded spectra with simulated spectra of known T_r and T_v until a good fit is found. The temperatures used in the fitted simulated spectra are then approximately T_r and T_v of the experimental discharge [87].

Under certain conditions, rovibrational band fitting can be extended to estimate neutral gas temperature (T_g) as well as T_r and T_v. Having higher energy level separation, excitation energy for vibrational modes is higher than for rotation and translation, and T_v is often much higher than T_g, but T_r and T_g may be in thermal equilibrium. For T_r and T_g to be in equilibrium, the lifetime of the ground rotational state must be longer than the time between collisions [88] allowing for molecules in the rotational ground state to thermalise. Additionally, during rovibrational spectroscopy experiments, the light analysed is from emission from an upper rotational state, not the ground state, so it is also a requirement that the upper and ground rotational states are in thermal equilibrium. Assuming that the ground state is a single Boltzmann distribution, then the excited state of interest must also be a single Boltzmann distribution [88, 89]. This can be safely assumed if the lifetime of the excited state is shorter than the time between heavy particle collisions, such that the excited state is created mainly from electron collisions. Electrons having low mass do not significantly alter the molecular rotational moment during a collision and the ground states distribution effectively maps onto the upper state distribution [90].

A variety of rovibrational bands within a variety of molecules in various discharges have been used previously for gas temperature determination from rovibrational fitting. The temperature of an atmospheric pressure air plasma was estimated using oxygen (O_2) and nitrogen ion (N_2^+) bands, in agreement with each other to within 2.4% [91]. Temperature of an inductively coupled CF_4 plasma was found to range from 1250 K to 1800 K using C_2, CF, CN and CO bands [92]. The Swann bands of carbon (C_2) have been used to determine a neutral gas temperature of a high power transformer coupled fluorocarbon plasma [93], and hydroxyl (OH) bands have been used to estimate temperatures in a 10 kV gliding arc discharge at atmospheric pressure [94].

Nitrogen gas is the most common gas used for temperature estimates from rovibrational band fitting. The N_2^+ first negative system has been used to find gas temperature in a gliding arc discharge at atmospheric pressure [94], a pulsed direct current (DC) hollow cathode discharge [95], and a low pressure dual frequency capacitively coupled plasma (CCP) [96]. The N_2 first positive system has been used for temperature estimates in a low pressure helicon plasma [97, 98], for a high pressure DC slot discharge [99], a radio-frequency (RF) inductively coupled plasma (ICP) at low pressure [100], and a high power, low pressure microwave discharge [101].

The second positive system (SPS) of neutral nitrogen ($C^3\Pi_u \rightarrow B^3\Pi_g$) is the most common N_2 band used, with gas temperature estimates made for CCPs and ICPs [82,90,96,102,103], an RF helicon discharge [104], and low pressure glow or positive column discharges [105, 106]. Temperatures of higher pressure and atmospheric pressure discharges have also been analysed with the N_2 SPS [107–109], as have temperatures during the first 400 ns of spark breakdown for an N_2 discharge [87]. This technique has also been used previously to determine neutral gas temperatures in a microwave electrothermal thruster [31] and a low power arcjet [110].

For N_2 at pressures of a few Torr (as found in Pocket Rocket) the time between collisions for heavy particles, calculated using Equation 1.15, with hard body sphere cross section estimated at 5×10^{-16} cm^2, is approximately 2 μs. The lifetime of the N_2 $C^3\Pi_u$ state is $\sim$37 ns [111], hence the $C^3\Pi_u$ state can be assumed to be a single Boltzmann distribution from electron excitation. This is supported by the rate coefficient from electron excitation being several orders of magnitude greater than other excitation channels [88]. Additionally, the rotational constants of the ground and $C^3\Pi_u$ states are similar, so even if the collisional condition is not completely satisfied, the $C^3\Pi_u$ should still be representative of the ground state [112].

The lifetime of the ground rotational state has not been measured exactly here but is expected to be significantly longer than 2 μs due to the inherent stability of N_2 molecules and the low ionisation degree, so it can be safely assumed that $T_r \approx T_g$ for the N_2 SPS under the conditions found in Pocket Rocket.

3.3.2 Application to Atomic Species

Atomic species do not produce rovibrational bands, so alternative methods to measure temperature must be explored. For example, it is possible to infer the temperature of an atomic species using OES by measuring the thermal Doppler broadening of spectral lines. Atomic velocities are related to the gas temperature (see Equation 1.2), so as atoms move relative to the optic capture device, the wavelength of light captured is Doppler shifted, and the atomic spectral line becomes broadened.

The half-width, half-maximum broadening of a spectral line from Doppler shifts ($\Delta\lambda_D$) is given by Equation 3.5, where λ_0 is the frequency of the spectral line of interest, c is the speed of light in a vacuum and m is the mass of the atom [113].

$$\Delta\lambda_D = \frac{2\lambda_0}{c}\sqrt{\frac{2kT_g ln2}{m}} \tag{3.5}$$

However, using the strong 750 nm line as a guide, the Doppler broadening is only 0.1 pm for argon at 1000 K, two orders of magnitude below the resolution of the available OES equipment of 0.2 Å (see Section 3.3.3) and the temperature of argon cannot be determined directly from thermal Doppler broadening here.

Alternatively, addition of trace amounts of a diatomic gas to an atomic element discharge allows for the same rovibrational spectroscopy method described above in Section 3.3.1 to be used to estimate temperature. This has been previously done with trace amounts of N_2 in chlorine gas (Cl_2) [82, 102], hydrogen gas (H_2) [33, 110] and for noble gas discharges of helium [105, 108, 114] neon (Ne) [107], argon (Ar) [31, 89, 90, 93, 99, 103, 104, 108] and krypton (Kr) [90]. For this work, argon gas temperatures are estimated by adding trace amounts of N_2 to an argon discharge and fitting the N_2 SPS system.

For this technique to be valid for atomic temperature determination additional requirements must be met, being that the atomic and diatomic species are in thermal equilibrium and that the main excitation channel for the upper state remains as electron impact to retain the Boltzmann distribution. Further discussion on these additional requirements in relation to the Pocket Rocket discharge specifically is included in Section 4.1.

3.3.3 Experimental Setup

Observed bands of the SPS range from 281.4 nm to 497.6 nm [85] with persistent strong bands occurring at 337,1 nm, 357.7 nm, 371.1 nm, 375.5 nm, 380.5 nm, 394.3 nm, 399.8 nm and 405.9 nm. For this work, the wavelength region 365 nm - 381 nm is used, capturing the persistent strong bands at 380.5 nm, 375.5 nm and 371.1 nm corresponding to the (0,2), (1,3), (2,4) vibrational transitions, as well as the slightly weaker (3,5) band at 367.2 nm. Additionally, this region contains only a few weak argon lines to minimise argon interference during the argon-nitrogen mixture experiments [84].

For this technique individual rotational bands may be unresolved [87], but it is desirable to resolve the band head and tail region which is not possible with the 2 nm resolution provided by the Ocean Optics spectrometer. Instead, a SPEX 500M monochromator with 500 mm focal length, 1200 groove/mm grating, and 50 μm entrance slit width is used in conjunction with a 3.5 mm diameter fused silica fibre optic cable positioned to capture light emitted through the plenum window.

An Ames Photonics Garry 3000S charge coupled device (CCD) array is placed at the exit plane of the monochromator. The CCD array is 21 mm long with 3000 pixels which when combined with a dispersion of 1.6 nm/mm in the monochromator simultaneously captures a 34 nm wavelength range spectra with a resolution of 0.02 nm. A higher resolution can be achieved by using an exit slit and a photomultiplier tube (PMT) tube in place of the CCD array. However, only one wavelength can be measured at a time so to scan through the entire 16 nm region of interest of the N_2 SPS takes several minutes during which time the discharge characteristics may change affecting the results.

The monochromator is aligned so that the 16 nm wavelength range of interest is located between pixels 750 and 2250 of the CCD array. The response function of the CCD array over this central range is essentially flat, so no intensity correction is needed. The response function was tested by scanning a constant intensity argon line across the full pixel range of the CCD and recording the change in intensity. A slight decrease in measured intensity was noted for pixels near both ends of the CCD array, but this is well outside the 750-2250 pixel range used to capture the rovibrational spectra.

To process the experimental spectra for fitting, background noise spectra captured at the start of each experiment are subtracted from the discharge spectra. In the case of the argon-nitrogen mixture experiments, the background spectra are pure argon discharge spectra to remove any interference from argon lines, otherwise they are spectra recorded with the discharge off. The spectra are then smoothed using a Golay smoothing function to reduce any remaining noise effects and trimmed to the 16 nm region of interest from 365 nm to 381 nm.

3.3.4 Simulating Rovibrational Spectra

To artificially create the spectra required for fitting to the experimental data, the wavelengths and intensities for each possible transition between the various rotational, vibrational and electronic states must be calculated. This is achieved by first calculating the energy of each rotational and vibrational state of interest by analysing the molecule as a anharmonic oscillating, non-rigid rotor.

The vibration of a diatomic molecule comes from the repelling force of the positively charged nuclei and the attracting force of the electron swarm causing oscillatory motion of the two atoms, analogous to two point masses connected by a spring. The bounds for diatomic vibration are given by the limits of the molecular potential energy curve, a generic example of which is shown in Figure 3.4, representing the balance between the repulsion of the nuclei and the attraction of the electron swarm. The horizontal axis shows interatomic distance (r) with the lowest point of the curve representing the equilibrium bond length (r_e), and the vertical axis shows the potential energy (U).

The wavefunction of each vibrational mode must form a standing wave within the bounds of the curve, otherwise the wavefunction annihilates and the vibrational mode cannot exist. Example wavefunctions are included in Figure 3.4 for the ground and first three excited states, with an additional four vibrational levels shown without wavefunctions. Although many more vibrational states exist within diatomic molecules, these few only are included as examples for clarity.

The potential energy (U) of a molecular bond is approximated by Equation 3.6, where D_e is dissociation energy and β represents the narrowness of the well.

$$U(r) = D_e(1 - e^{-\beta r - r_e})^2 \tag{3.6}$$

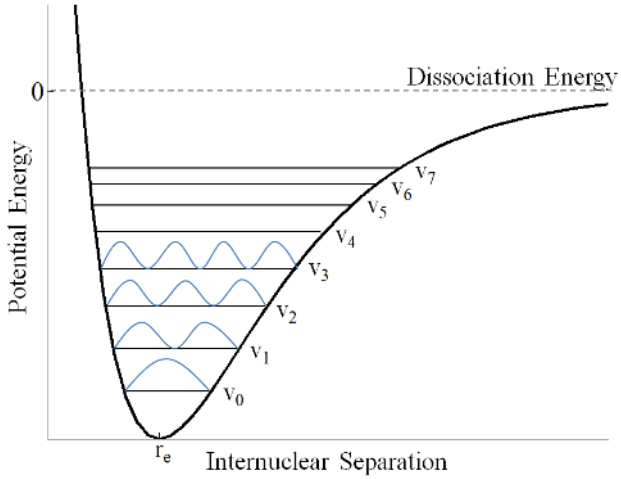

Figure 3.4: Potential energy curve for a diatomic molecule.

For low vibrational quantum numbers, only oscillations near the bottom of the well are considered so potential energy can be estimated as a Maclaurin series expansion about r_e, given in Equation 3.7 where r is instantaneous bond length.

$$U(r) = U_{r_e} + r(\frac{dU}{dr})_{r_e} + \frac{1}{2}r^2(\frac{d^2U}{dr^2})_{r_e} + \frac{1}{6}r^3(\frac{d^3U}{dr^3})_{r_e}... \tag{3.7}$$

Arbitrarily taking the potential energy at the equilibrium bond length (r_e) to be 0 and given that $(dU/dr)_{r_e} = 0$ makes the first two terms in Equation 3.7 zero. Retaining only the r^2 term gives a solution identical to the classical Hooke's law spring treatment. However, the asymmetry of the potential energy curve is better represented as an anharmonic oscillator by retaining both the r^2 and r^3 terms in Equation 3.7, giving $U(r) = \frac{1}{2}r^2(\frac{d^2U}{dr^2})_{r_e} + \frac{1}{6}r^3(\frac{d^3U}{dr^3})_{r_e}$. An approximate solution of the Schrödinger equation with this $U(r)$ is found using a perturbation method [115] and leads to an expression of allowed vibrational energy levels given in Equation 3.8 where $\bar{\omega}_e$ and $\omega_e\bar{x}_e$ are molecular constants found in references [115,116] for example.

$$E_v = \bar{\omega}_e(v + \frac{1}{2}) - \omega_e\bar{x}_e(v + \frac{1}{2})^2 \tag{3.8}$$

Rotational motion of a molecule is approximated as a non-rigid rotor, as the changing bond length from vibration can affect the rotational modes. The total energy (E) of a non-rigid rotor, given by Equation 3.9, is a combination of the kinetic energy $T = \frac{1}{2}I\omega^2$ where I is the moment of inertia and ω is the angular velocity, and potential energy from stretching of the bond $U = \frac{1}{2}k(r - r_e)^2$ where k is the spring constant.

$$E = \frac{1}{2}I\omega^2 + \frac{1}{2}k(r - r_e)^2 \tag{3.9}$$

Throughout the molecule's rotation, the stretching of the bond is balanced by centrifugal force $mr\omega^2$, as shown in Equation 3.10.

$$\frac{1}{2}k(r - r_e) = mr\omega^2 \tag{3.10}$$

Combining Equations 3.9 and 3.10, and assuming the nuclei act as point masses such that angular momentum is given by $I = mr^2$ gives Equation 3.11.

$$E = \frac{1}{2}\frac{(I\omega)^2}{mr^2} + \frac{1}{2}\frac{(I\omega)^4}{m^2r^4k} \tag{3.11}$$

Rotational angular momentum ($I\omega$) of a molecule is quantised as $\sqrt{J(J+1)}\frac{h}{2\pi}$ [115, 117]. Substituting this into Equation 3.11 gives Equation 3.12, the allowed rotational energies of a diatomic molecule.

$$E_J = \frac{h^2}{8\pi^2 mr_e^2}J(J+1) - \frac{h^4}{32\pi^4 m^2 r_e^6 k}J^2(J+1)^2 \tag{3.12}$$

Often, Equation 3.12 is written in the simplified form shown in Equation 3.13 where $B_e = \frac{h^2}{8\pi^2 mr_e^2}$ and $D_e = \frac{4B_e^3}{\omega_e^2}$ are the rotational constants, found in references [115, 116] for example.

$$E_J = B_e J(J+1) - D_e J^2(J+1)^2 \tag{3.13}$$

For this work, all nitrogen second positive system vibrational and rotational constants (ω_e, $\omega_e x_e$, B_e and D_e) are taken from Herzberg and Huber ([115] pg 552)

The wavelength (λ) of an electronic transition within a diatomic molecule is still related to the change in energy as given in Equation 3.3 for an atomic species, but the addition of the rotational and vibrational energies adds complexity. The wavelengths for transitions from an upper state ($n'v'J'$) to lower state ($n''v''J''$) in a diatomic molecule are given by Equation 3.14 [87].

$$\lambda^{n'v',J'}_{n''v'',J''} = [n_a \sum_{pq} Y^{n'}_{pq}(v' + \frac{1}{2})^p[J'(J'+1)]^q - Y^{n''}_{pq}(v'' + \frac{1}{2})^p[J''(J''+1)]^q]^{-1} \tag{3.14}$$

In Equation 3.14, n_a is the refractive index of air, included to convert the calculated wavelength from the vacuum state to the adjusted wavelength for propagation in air and Y_{pq} are Dunham coefficients [118] with subscripts p and q referring to the powers of the vibrational and rotational quantum numbers, respectively. Dunham coefficients are essentially reduced versions of various combinations of ω_e, $\omega_e x_e$, B_e

and D_e to simplify the wavelength equation, taken for this work for values of p from 0 to 5 and q from 0 to 2 from equations published in Dunham [118].

The intensity (I) of an electronic transition with wavelength λ is given by Equation 3.15, dependent on the number of molecules in the upper state ($N_{n'v'J'}$), and the transition probability ($A^{n'v',J'}_{n"v",J"}$).

$$I^{n'v',J'}_{n"v",J"} = \frac{hc^2}{\lambda} N_{n'v'J'} A^{n'v',J'}_{n"v",J"} \tag{3.15}$$

The number of molecules in the upper state can be estimated using a Maxwell-Boltzmann distribution as long as the temperature is significantly higher than the difference between vibrational and rotational energy levels. In general, the difference between vibrational levels is 0.01 eV [86], whereas temperature is 0.03 eV (300 K) or higher. Hence, the number of molecules in the upper vibrational state (v') is given by Equation 3.16a, where N_{v0} is the number of molecules in the vibrational ground state and T_v is vibrational temperature. The number of molecules in the upper rotational state (J') is given by Equation 3.16b, where N_{r0} is the number of molecules in the rotational ground state and T_r is the rotational temperature.

$$N_{v'} \approx N_0 e^{-\frac{E_v}{kT_v}} \tag{3.16a}$$

$$N_{J'} \approx N_0 e^{-\frac{E_J}{kT_r}} \tag{3.16b}$$

The probability of a vibrational transition is dependent on the overlap of the wavefunctions of the upper and lower vibrational levels [119]. The internuclear separation of a diatomic molecule immediately after an electronic transition is the same as immediately prior to the transition [120]. However, often this no longer is the equilibrium position for the new vibrational level and the molecule will begin to vibrate more. The most probable transitions involve a minimum change in equilibrium internuclear distance. The resulting vibrational transition probabilities are known as Franck-Condon factors ($q_{v'v"}$) [115,117] and are always constant for a given transition [121]. For this work, values for $q_{v'v"}$ are taken from Zare *et al.* [122].

Transition probabilities for rotation depend on the selection rules for allowed rotational transitions. The total angular momentum ($\vec{J}$) of a molecule is a combination of electron spin, electron orbital angular momentum and angular momentum of nuclear rotation, and must be conserved during a rotational transition. The component of $\vec{J}$ along the internuclear axis of a diatomic molecule is denoted by $\vec{\Lambda}$, and

is given values of 0,1,2,... for states designated as Σ, Π, Δ,... [115], hence $\vec{\Lambda} = 1$ for both the upper and lower states of the N_2 SPS. For a transition where $\vec{\Lambda} \neq 0$ in either the upper or lower state, the selection rule for J is given by Equation 3.17 [115].

$$\Delta J = J' - J'' = 0, \pm 1 \tag{3.17}$$

This results in three branches: the $\Delta J = 1$ or R branch, the $\Delta J = -1$ or P branch, and the $\Delta J = 0$ or Q branch. The transition probabilities, hence relative line strengths between the three branches, are determined by Hönl-London factors (S_J). Calculation of S_J depends on the coupling of the angular momentum of rotational and electronic motion given by the Hund's coupling case, of which there are five possible cases in total ((a)-(e)) [115], two of which are relevant here.

Hund's case (a) occurs when the angular momentum of nuclear rotation interacts only weakly with electron angular momentum effects, so electron motion occurs mostly on the axis joining the nuclei. The treatment of a molecule in Hund's case (a) is that of a simple vibrating rotator (as described above). For Hund's case (b), spin is only weakly or not at all coupled to the internuclear axis in which case total orbital angular momentum excluding spin may become slightly magnetically coupled leading to a slight splitting into triplet states occurring.

The N_2 SPS is Hund's case (a) for low J, transitioning to Hund's case (b) for higher J [87]. However, at high J values the difference between the (a) and (b) cases is small, and case (a) can be assumed throughout. Also, the separation of triplet splitting is 0.08 nm, less than the difference in rotational separation and can safely be neglected [87]. Another splitting effect, known as Λ-type doubling, occurs at high rotational speeds when $\Lambda \neq 0$. For the N_2 SPS, splitting from Λ-type doubling is less than 0.04 nm [87], again lower than the rotational separation and can be neglected.

Assuming Hund's case (a), and neglecting the various splitting effects, the relevant equations to calculate the Hönl-London factors for the N_2 SPS are shown in Equation 3.18 [115].

$$S_J^R = \frac{(J' + \Lambda')((J' - \Lambda')}{J'} \tag{3.18a}$$

$$S_J^Q = \frac{(2J' + 1)\Lambda'^2}{J'(J' + 1)} \tag{3.18b}$$

$$S_J^P = \frac{(J' + 1 + \Lambda')((J' + 1 - \Lambda')}{J' + 1} \tag{3.18c}$$

Substituting the Hönl-London factors (Equations 3.18), the Franck-Condon factors ($q_{v'v''}$) and Maxwell-Boltzmann population distributions (Equations 3.16) into Equation 3.15, gives Equation 3.19, the intensity of a spectral line in the N_2 SPS, where D is an arbitrary scaling constant accounting for constants collected throughout the analysis and experimental equipment sensitivity.

$$I^{n'v',J'}_{n''v'',J''} = \frac{D}{\lambda^4} q_{v',v''} e^{\frac{-E_{v'}}{kT_v}} S_{J',J''} e^{\frac{-E_{J'}}{kT_r}} \tag{3.19}$$

Using Equation 3.14 for wavelength and Equation 3.19 for intensity, the rovibrational spectrum of a diatomic molecule can be simulated, for fitting to an experimental spectrum for temperature estimation.

3.3.5 Rovibrational Band Fitting

Before fitting the theoretical and experimental spectra, the simulated lines must be artificially broadened to match the natural experimental broadening effects, such as Doppler broadening and equipment broadening. Here, a Gaussian convolution kernel, described in Equation 3.20, is used on λ to match the experimental broadening. The value of σ determines the magnitude of the broadening and is chosen based on the shape of the sharp mercury 546 nm line, produced by a mercury lamp and recorded using the same equipment as outlined in Section 3.3.3.

$$g(\lambda) = \frac{1}{\sqrt{2\pi}\sigma} e^{-\frac{(\Delta\lambda)^2}{2\sigma^2}} \tag{3.20}$$

The iterative fitting procedure between the experimental and simulated spectra is performed using Monte Carlo Markov Chains (MCMC) over 50000 iterations, with the first 10000 iterations binned. This results in a range of credible values output for T_r and T_v from which a 95% confidence range for the temperature is stated. It should be noted that the fitting code used here is adapted from software previously developed by the Inversion Laboratory (ilab) that employed the same MCMC technique and is not written directly by the author.

Example fits between the experimental data and corresponding simulated spectrum for a 10 W, 1.5 Torr plasma in N_2 and argon with 1 % N_2 addition are shown in Figure 3.5. Validation of the fitting procedure was performed by comparison of temperature results with two other independently developed fitting codes from

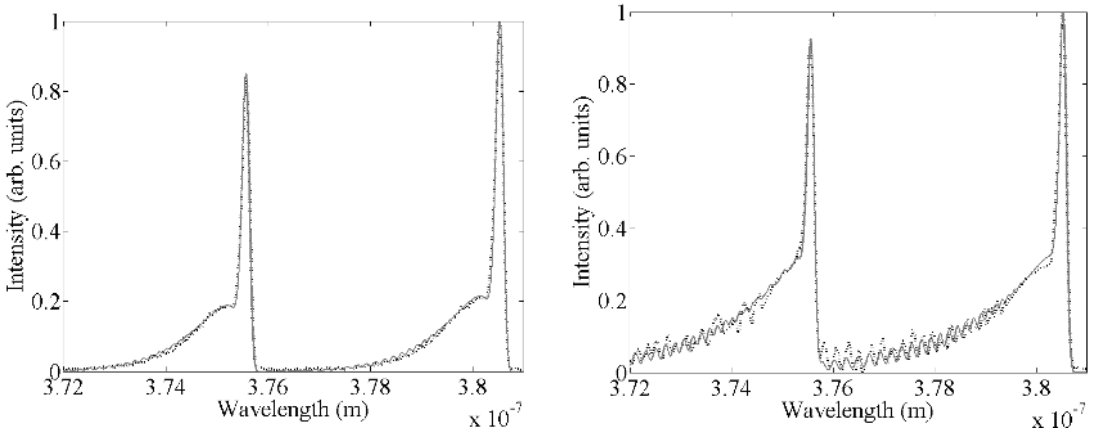

(a) (b)

Figure 3.5: Example rovibrational band fitting for a 10 W, 1.5 Torr plasma in (a) N_2 and (b) argon with 1% N_2. The experimental spectra are shown as dotted black lines with the simulated spectra overlayed as solid grey lines.

Open University and the York Plasma Institute. The experimental spectrum used was produced by a 10 W, 1.5 Torr argon plasma with 10 % N_2 addition captured using the PMT placed at the exit slit of the monochromator, noting this is a different data set than the example fit shown in Figure 3.5. A summary of the three results is shown in Table 3.1.

Table 3.1: Comparison of results from rovibrational band fitting codes.

Code	T_r	T_v
SP3	1605±15 K	3905±200 K
Open University	1570±75 K	4050 K
York Plasma Institute	1530±25 K	-

All three independent codes produced corresponding values for T_r with uncertainties taken into account. The values for T_v produced by the code used in this work and the Open University code are also in agreement. The York Plasma Institute code employed a slightly different technique to that outlined above and did not produce values for T_v for comparison.

Using the rovibrational band fitting technique outlined and validated in this section allows for direct measurement of the neutral gas temperatures within the Pocket Rocket discharge. This is used to infer proof of concept and estimate rough

thruster performance values in Chapter 4, then to investigate the heating mechanisms through spatiotemporal analysis of gas temperature in Chapter 5.

3.4 Computational Fluid Dynamics

Complementary to experiment diagnostics, computer based modelling of plasma discharges provides an alternative method for analysing plasma discharges. Particle-In-Cell (PIC) simulations involve tracking individual particles, or super particles representing millions of individual particles, over physical and velocity space. Fully kinetic PIC simulations of RF CCP discharges have previously been performed for one [55, 57, 123, 124], two [52, 125] and three [126] spatial dimensions. However, as particles are simulated directly, high dimension, high pressure PIC simulations become very computationally expensive.

Computational Fluid Dynamics (CFD) simulations are a continuum modelling alternative to PIC simulations, where fluid equations are solved using numerical methods, rather than directly simulating particles. The use of continuum equations limits the use of CFD to fully collisional regimes but significantly reduces computational times. For the use of a continuum approximation to be valid, the Knudsen number of the flow needs to be less than ∼0.1 [127]. The Knudsen number (Kn) is a dimensionless parameter relating the mean free path (λ_{mfp}) and characteristic length scale (L). For a Boltzmann gas Kn is given by Equation 3.21, and is dependent on neutral gas temperature (T_g), pressure (p) and hard shell diameter of the gas particles (d).

$$Kn = \frac{\lambda_{mfp}}{L} = \frac{kT_g}{\sqrt{2}\pi d^2 pL} \tag{3.21}$$

Within Pocket Rocket, the characteristic length scales of interest are the plenum diameter (40 mm), the discharge tube diameter (4.2 mm) and the expansion tube diameter (50 mm). Assuming a temperature of 300 K throughout the flow, with pressures of 1.5 Torr in the plenum, 1 Torr in the discharge tube and 0.75 Torr in the expansion tube, the corresponding Knudsen numbers are 0.015, 0.105 and 0.024. Although the flow in the discharge tube is on the limit of the continuum approximation, it is suitable to use CFD to examine the Pocket Rocket discharge.

For this work, the commercial Computational Fluid Dynamics Advanced Com-

putational Environment (CFD-ACE+) package from the ESI Group is utilised to perform a transient, 2D simulation of the Pocket Rocket device. The CFD-ACE+ software has been previously used to simulate a DC N_2 microplasma [128], xenon dielectric barrier discharge (DBD) [129], a 2D argon DC glow discharge [130, 131], 2D and 3D ICP etching reactors [132, 133] and CCP etching reactors in 2D and 3D with argon and hydrocarbon discharges [133, 134].

3.4.1 Fluid Model

Simulations of CCPs, like that within Pocket Rocket, require background gas flow and turbulence, heating, electric fields, space charges, collisions and plasma kinetic effects to be included. The equations and techniques used to simulate these effects are outlined below. The governing equations for heavy particle flow parameters are mass conservation and the Navier-Stokes equation, given in Equations 3.22 and 3.23 respectively, where ρ is density, $\vec{V}$ is velocity, μ is viscosity and S_M represents momentum added from any defined source, such as the inlet.

$$\frac{\delta\rho}{\delta t} + \nabla.(\rho\vec{V}) = 0 \tag{3.22}$$

$$\frac{\delta(\rho\vec{V})}{\delta t} + \nabla.(\rho\vec{V}u) = -\nabla.p + \nabla.(\mu\nabla u) + S_M \tag{3.23}$$

The total pressure, p, is given by Equation 3.24, and is the sum of the static partial pressures (p_i) for all heavy species, calculated from the ideal gas law, and the electron pressure ($p_e = n_e k T_e$, where n_e is electron density, k is Boltzmann's constant and T_e is the electron temperature).

$$p = \sum_i p_i + n_e k T_e \tag{3.24}$$

A standard $k - \epsilon$ turbulence model is included for all heavy species (refer to Launder and Spaulding [135] for full details of this model). However, the low pressure in the system results in little difference ($\sim$2.4%) between fully laminar and turbulent simulations.

A transport equation of the form shown in Equation 3.25 is solved for each species (k) including ions, where Y_k is the species mass fraction, defined as the mass of the k^{th} species per mixture unit mass, $\vec{D}_k^c$ is diffusion from concentration gradients, M_k

is the molecular weight of the species, and ω_k is the production rate from reactions.

$$\frac{\delta \rho Y_k}{\delta t} + \nabla . \rho \vec{V} Y_k = -\nabla . \vec{D_k^c} + M_k \omega_k \tag{3.25}$$

For ions, the effect of ion drift must be considered, with ion mass flux $\vec{J_i}$ given by Equation 3.26, where $\vec{V}_{di}$ is ion drift velocity, and $\vec{J_i^c}$ is a correction/source term to account for ion creation and loss and ensures species flux conservation holds. The ion diffusion coefficient (D_i) is taken to be the same as that of the corresponding neutral particle.

$$\vec{J_i} = -\rho D_i \nabla Y_i + \rho \vec{V_{di}} Y_i + \vec{J_i^c} \tag{3.26}$$

The pressures used in Pocket Rocket are around a few Torr, so it is assumed that the collision frequency of ions is sufficiently high to use the drift diffusion approximation for ion drift velocity ($\vec{V_{di}} = q_i \mu_i \vec{E}$, where q_i is the charge of the ion and $\vec{E}$ the electric field), rather than solving directly for ion momentum. Ion mobility (μ_i) is solved for using Einstein's relation, $\mu_i = \frac{D_i}{T_i}$, where ion temperature (T_i) is approximated as the neutral gas temperature.

The applied RF field and space charge effects from ions and electrons are solved using Poisson's equation (Equation 3.27) for the electrostatic potential (ϕ), where ϵ is the permittivity of the local medium, e is electron charge, q_i is the charge on the i^{th} ion and n_e and n_i are the electron and ion densities, respectively.

$$-\nabla . \epsilon \nabla \phi = e(\sum_i q_i n_i - n_e) \tag{3.27}$$

Heavy particle surface reactions are invoked, such that on collision with a wall an ion or excited neutral will return to the neutral ground state. Particle fluxes normal to the wall for both ions ($\Gamma_{i,n}$) and electrons ($\Gamma_{e,n}$) are used to calculate space charge (σ) accumulation on the surface of the alumina (dielectric) tube as shown in Equation 3.28.

$$\frac{\delta \sigma}{\delta t} = e \sum_i (q_i \Gamma_{i,n} - \Gamma_{e,n}) \tag{3.28}$$

Ion flux normal to the wall ($\Gamma_{i,n}$) is given by Equation 3.29, where α_i is the sticking coefficient, C_i^w is the concentration of the species of interest at the wall and $\vec{V}_{ch,i}$ is the characteristic velocity given by the drift velocity (V_{di}) for ions and $\vec{V}_{ch,i} = \sqrt{\frac{RT}{2\pi m_i}}$ for neutrals, where R is the universal gas constant.

$$\Gamma_{i,n} = m_i \alpha_i \vec{V}_{ch,i} C_i^w \tag{3.29}$$

Electron flux normal to the wall ($\Gamma_{e,n}$) is given by Equation 3.30 where m_e is the mass of an electron and γ is the ion induced secondary electron emission coefficient.

$$\Gamma_{e,n} = n_e(\frac{kT}{2\pi m_e})^{\frac{1}{2}} - \gamma \sum_i (q_i \Gamma_{i,n}) \tag{3.30}$$

Electron transport behaviour within the bulk plasma is modelled using the electron drift diffusion approximation given in Equation 3.31 where $\vec{\Gamma_e}$ is electron density flux and μ_e is electron mobility, and the electron particle balance equation given in Equation 3.32 where S_e accounts for electrons produced or consumed in chemical reactions.

$$\vec{\Gamma_e} = \mu_e n_e \nabla\phi - D_e \nabla n_e \tag{3.31}$$

$$\frac{\delta n_e}{\delta t} + \nabla.\vec{\Gamma_e} = S_e \tag{3.32}$$

Electron diffusivity (D_e) is calculated using Equation 3.33, where ϵ_k is electron kinetic energy and C is the Maxwellian distribution scaling factor. The electron collision frequency (ν_m) is a function of T_e assuming a single temperature Maxwellian distribution ($f_0(T_e)$), as shown in Equation 3.34.

$$D_e = T_e \mu_e = \frac{2e}{3 m_e n_e} \int_0^\infty \frac{C \epsilon_k^{\frac{3}{2}}}{\nu_m(\epsilon_k)} e^{(\frac{-\epsilon_k}{T_e})} \delta\epsilon_k \tag{3.33}$$

$$\bar{\nu_m} = \frac{3}{2n_e} \int_0^\infty \nu_m(T_e) T_e^{\frac{1}{2}} f_0(T_e) d\epsilon \tag{3.34}$$

The electrons are assumed to follow a single temperature Maxwellian distribution due to high collision frequencies within the high pressure discharge, hence the electron temperature (T_e) is calculated using the electron energy balance equation (Equation 3.35).

$$\frac{3}{2}\frac{\delta}{\delta t}(n_e T_e) + \frac{5}{2}\nabla(T_e \vec{\Gamma_e} - n_e D_e \nabla T_e) = P - n_e \sum_k N_k c_k \epsilon_k \tag{3.35}$$

Energy loss from collisions is equated by the sum term on the right hand side (RHS) with N_k, c_k and ϵ_k being the number density, coefficient of collisional energy loss and kinetic energy of the collisional species, respectively. Power density (P) includes Joule heating and stochastic sheath heating, given in Equations 3.36 and 3.37, respectively.

$$P_{Joule} = e\Gamma_e.(\nabla\phi) \tag{3.36}$$

$$P_{stoch} = 0.61(\frac{m_e}{e})^{\frac{1}{2}}\epsilon_0\omega^2 T_e^{\frac{1}{2}}V \tag{3.37}$$

Stochastic heating is considered only in the sheath region near the powered electrode, dependent on the angular driving frequency at the RF electrode (ω) and the potential difference between the RF electrode and current grid point (V). Higher operating pressures in Pocket Rocket and the self-bias that develops on the alumina tube from the large asymmetry of the device means stochastic heating effects are small and the majority of electron heating comes from Joule heating.

Heavy particle heat transfer is expressed using the energy equation in terms of gas temperature (T_g), given by Equation 3.38, where c_p is specific heat and k is thermal conductivity.

$$c_p(\frac{\delta\rho T_g}{\delta t} + \nabla.\rho\vec{V}T_g) - \nabla.(k\nabla T_g) = \sum_m \Gamma_m C_m p_k.\nabla T_g - \sum_n \epsilon_n\dot{\omega}_n + \dot{Q} \tag{3.38}$$

The two terms on the left hand side (LHS) represent the convective and conductive heat transfer respectively, and the first term on the RHS the concentration (C) and temperature gradient driven diffusive flux. The last two terms on the RHS represent heating from electron and ion effects, respectively.

Electron elastic collisions result in the release of heat ϵ_n through non-electronic reactions and momentum transfer collisions with collision rate $\dot{\omega}_n$. For non-electronic reactions, ϵ_n is given by Equation 3.39 where h_i is enthalpy and v''_{ir} and v'_{ir} are the stoichiometric coefficients for the products and reactants. For momentum transfer collisions with Maxwellian electrons, ϵ_n is given by Equation 3.40.

$$\epsilon_{n_{non-elec}} = \sum_i (v''_{in} - v'_{in})h_i \tag{3.39}$$

$$\epsilon_{n_{mtm}} = \frac{3m_e e}{M}(T_e - T_g) \tag{3.40}$$

Volumetric heat addition from ion Ohmic heating and ion surface recombination ($\dot{Q}$ in Equation 3.38) is denoted by Equations 3.41 and 3.42, respectively.

$$\dot{Q}_{ion} = \sum_{q_i>0} q_i n_i \mu_i \vec{E}.\vec{E} \tag{3.41}$$

$$\dot{Q}_{wall} = \sum_{i=heavy} \Gamma_{i,n} h_i + \sum_{i=ions} \Gamma_{i,n}\epsilon_{k,i} \tag{3.42}$$

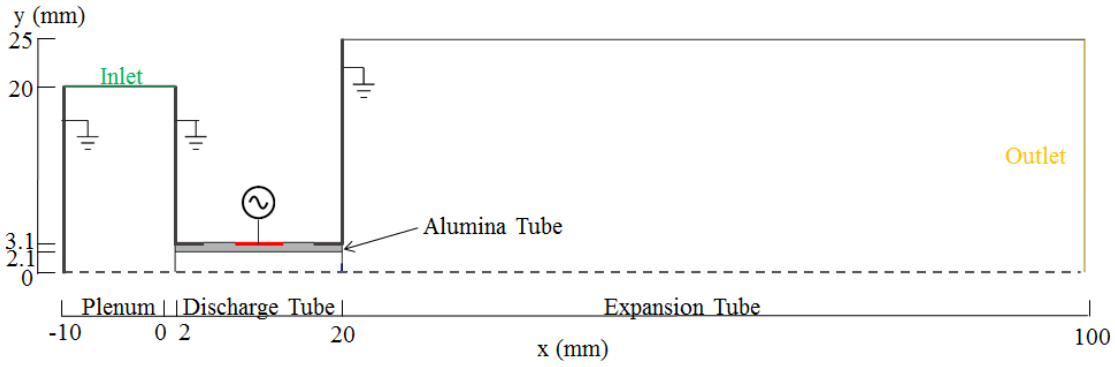

Figure 3.6: 2D axisymmetric Pocket Rocket model used for CFD simulations

Ion surface heating constitutes chemical heat released during ion neutralisation on the surface (first term on the RHS of Equation 3.42) and heat released from ion kinetic energy (second term on the RHS of Equation 3.42, with ion kinetic energy $\epsilon_{k,i} = \frac{1}{2} m_i \vec{V}_i^2$, with $\vec{V}$ the potential gain of the ion across the sheath.

3.4.2 Pocket Rocket Model

The equations described above to simulate the various gas flow and plasma effects are solved on a grid representing the geometry of the Pocket Rocket device, known as the mesh. To minimise the simulation run time without losing any geometric aspects of the device, the cylindrical symmetry of Pocket Rocket is exploited. The CFD model used, shown in Figure 3.6, is the top half of an axial 2D cross section including the plenum chamber, discharge tube and expansion tube. An axisymmetry condition applied around the central axis of the discharge tube (the dashed line in Figure 3.6) reduces the total number of mesh points while retaining all geometric features.

The plenum chamber, discharge tube, and glass expansion tube are defined as joined fluid domains, with the alumina tube (shaded grey in Figure 3.6) defined as a solid domain with dielectric properties. The main thruster housing is not included to reduce simulation complexity and simulation time, and instead all boundaries around the fluid volumes and alumina solid, including the electrodes, are modelled as thin walls. The location of the powered RF electrode is shown as a thick red line on the outer surface of the alumina tube, and the grounded walls including the grounded electrodes, end plate and plenum walls are shown as thick black lines.

Although the inlet of the experimental device is a small 2 mm diameter hole through the side wall of the plenum as outlined in Section 2.1, the simulation inlet is defined as the entire upper edge of the plenum chamber cross-section, as shown in Figure 3.6 in green. During experiments, the plenum pressure is used to define the upstream conditions rather than a specific flow rate, therefore the simulation inlet is defined using only a fixed pressure and not a flow rate. The use of a constant pressure inlet rather than a flow rate means the larger simulation inlet will not change the result, allowing for a simpler geometry to be modelled. The outlet corresponds to the end of the glass tube adjoining the vacuum chamber, and is the complete right hand side edge of the model geometry as shown in yellow in Figure 3.6.

To solve the continuous form partial differential equations (PDEs) defined in Section 3.4.1 over the mesh, the equations must first be discretised to allow stepping between temporal grid points (n) and spatial grid points (i). Discretisation over the time domain is performed using the backwards Euler method, which assuming the PDE is in the form $\frac{\partial f}{\partial x} = 0$, is given by Equation 3.43, where n is the current time step and i is the current spatial mesh point.

$$\frac{f_i^{n+1} + f_i^n}{\Delta t} + O(\Delta t) = \frac{f_{i+1}^n - 2f_i^n + f_{i-1}^n}{\Delta x^2} + O(\Delta x^2) \tag{3.43}$$

To ensure both heavy particles and electron kinetics are correctly captured by the simulation, a dual time-step approach is implemented. The heavy particle parameters are solved using a time step of 7.382 μs, longer than the period of one RF cycle ($\sim$72 ns), as the larger masses do not move sufficiently within an RF period to affect the results. Electrons, having much smaller mass, will exhibit sufficient movement within an RF cycle that must be resolved, therefore electron kinetics are solved using a time scale of $\frac{1}{20}$th of an RF period.

Spatial discretisation is performed using the first order upwind scheme, which assuming the PDE is in the form $\frac{\partial f}{\partial x} = 0$, is denoted by Equation 3.44.

$$\frac{f_i^n - f_{i-1}^n}{\Delta x} + O(x) = 0 \tag{3.44}$$

The first order upwind scheme is the most stable scheme in that it only uses one other grid point to solve for the current point. However, this results in errors of the first order ($O(x)$), so the solution may take longer to converge.

Starting points for the discretised solution are input by the user in the form of boundary and initial conditions. Initial conditions (ICs) are approximate values applied to each mesh point to give the solver a starting point for the first iteration and have no effect of the final solution, except that poorly chosen ICs may result in the simulation taking longer to converge. Boundary conditions (BCs) exist at the spatial limits of the mesh including walls, inlets and outlets, and can have a significant effect of the solution so must be as close to reality as possible.

The finer the spatial mesh of the model geometry the more accurate the final solution but the longer the computational time required. Conversely, a coarse mesh results in a solution far from the actual solution. For faster processing without losing accuracy the mesh can be weighted to be finer in important regions. In the case of a CCP discharge for example, the mesh should be weighted to be finer in regions expected to produce sheaths to better capture electron kinetics. The small mass of electrons gives them higher velocities than the heavy particles, so to correctly capture movement in the sheath the mesh needs to be finer in those regions.

To determine the best mesh density to use, a mesh convergence study was performed by running a simple flow only simulation of the Pocket Rocket device using various mesh densities and recording results of certain parameters. The mesh is independent of the result and no longer affects the solution when increasing the number of grid points does not change the solution results. Mesh densities tested are 1335, 2054, 4586, 11075, 19242 and 45812 total grid points, with the mesh weighted to be finer in regions expected to produce sheaths in all cases.

Inlet pressure is fixed at 1.5 Torr, outlet pressure is fixed at 0.75 Torr and the operating gas is defined as argon. The ideal gas law is used to calculate density, and dynamic viscosity is set as a constant 2.06×10^{-6} kg m^{-1} s^{-1}. All walls are defined as isothermal at 300 K with a no-slip condition invoking fluid boundary layers.

Maximum global axial velocity (blue circles), maximum global radial velocity (blue squares) and local pressure at the centre of the discharge tube (red diamonds) for each mesh density are shown in Figure 3.7(a). For clarity, the radial velocity values have been multiplied by 20 so they are displayed on a similar scale to the axial velocity. The total solution time for each run is shown in Figure 3.7(b). The mesh affects the result less than 1% above 11075 grid points but the solution time

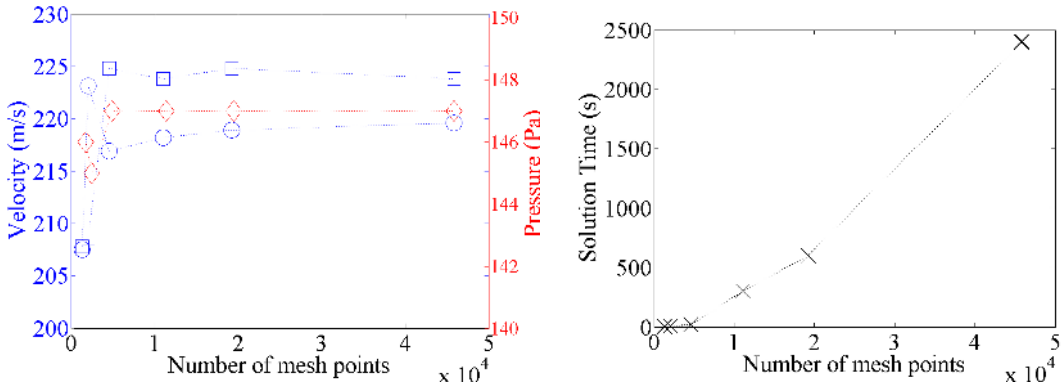

(a) (b)

Figure 3.7: Mesh convergence results for (a) maximum values for axial (blue circles) and radial velocity multiplied by 20x for clarity (blue squares) and the pressure at MP1 (red diamonds) and (b) total solution time.

increases sharply for mesh densities higher than this, so to balance computational time and accuracy, the 11075 grid point mesh is used for all further simulations.

A complete 2D axisymmetric simulation of Pocket Rocket produces 2D results for all main plasma parameters (plasma potential (V_p), n_e, ion density (n_i), T_e, etc) and all main background flow parameters (velocity (v), pressure (p), density (ρ), T_g, etc). Here, a simulation of the standard operating condition for a 10 W, 1.5 Torr argon plasma is performed (see Chapter 6) to validate the results against experimental data and develop a better understanding of the operation of Pocket Rocket. After the simulation results are validated, further simulations investigating various geometric and operational changes can be performed, to enhance the understanding of Pocket Rocket operation without the need for time consuming and potentially expensive adaptations to the experimental setup.

Chapter 4

Direct Measurement of Gas Temperature

Electrothermal thruster principles are based around high temperature gases expanding and cooling through a nozzle to provide thrust to the associated spacecraft. Within a plasma discharge based electrothermal thruster, neutral gas heating arises from energetic ions undergoing charge-exchange collisions with the background gas or propellant, as outlined in Section 1.3.6. To demonstrate that the Pocket Rocket concept has potential applications as an electrothermal plasma thruster, the neutral gas temperature (T_g) within Pocket Rocket is measured using the rovibrational band fitting technique outlined in Section 3.3.

Standard operating propellant for Pocket Rocket is argon (Ar) which is an atomic element, so to use the rovibrational band fitting technique trace amounts of nitrogen (N_2) are added to the Ar discharge, allowing the N_2 second positive system ($C^3\Pi_u \rightarrow B^3\Pi_g$) to be used for analysis. Pure N_2 discharges are also analysed as an alternate propellant for comparison. Addition of N_2 to an Ar discharge opens additional excitation channels for the $C^3\Pi_u$ state, introducing complications to the rovibrational band fitting method which are discussed in Section 4.1. Steady state volume averaged neutral gas temperatures in N_2 and Ar (with trace N_2) for various powers and pressures are measured and discussed in Section 4.2. The chapter finishes with a discussion summarising these temperature measurements and the resulting application of Pocket Rocket as an electrothermal thruster in Section 4.3.

4.1 Argon Metastable Influence

Rovibrational band fitting to determine T_g from rotational temperature (T_r) of a diatomic molecule outlined in Section 3.3 is only relevant if the single excitation channel to the upper measured state (here the $C^3\Pi_u$ state) is from electron impact. Being very low mass in comparison to N_2 molecules an electron collision has little effect on the rotational distribution, and the upper rotational distribution can be considered to be identical to the ground state rotational distribution, giving correct values for T_r and hence T_g.

For discharges involving mixtures of N_2 and Ar, resonance energy transfer between argon metastable atoms (Ar_m^*) and N_2 molecules introduces a second excitation channel that does not necessarily map the ground rotational state onto the $C^3\Pi_u$ state and enhances high rotational levels of the $C^3\Pi_u$ state [136, 137]. If the excitation channel from Ar_m^* and N_2 collisions is a significant process, the T_r estimated from the rovibrational spectroscopy method may be incorrect, and any resultant estimates of T_g will also be incorrect.

4.1.1 Metastable Resonance Energy Transfer

The Ar_m^* states, $^3P_2$ and $^3P_0$, have lifetimes in the order of seconds [123], due to the spin and rotation selection rules ($\Delta S = 0$ and $\Delta J = 0, \pm 1$, respectively) preventing spontaneous radiative transitions to the ground state. The long lifetimes mean Ar_m^* density can become a significant proportion of the neutral density population.

Excitation energies for the $^3P_2$ and $^3P_0$ states are 11.72 eV and 11.54 eV, respectively [98, 138], similar to the threshold excitation energy for the N_2 second positive system (SPS) of 11.1 eV [139]. Collisions between Ar_m^* and N_2 results in deactivation of the metastable atom with resonance energy transfer to the N_2 $C^3\Pi_u$ state through the process shown in in Equation 4.1, where $N_2(X^1\Sigma_g)$ is the N_2 ground state.

$$N_2(X^1\Sigma_g) + Ar_m^* \rightarrow N_2(C^3\Pi) + Ar \tag{4.1}$$

Excess energy from the collision is transferred into high rotational levels of the N_2 SPS resulting in enhanced tail structures within the rovibrational bands [136, 137]. Deactivation of Ar_m^* by an N_2 molecule has a cross-section 100 times larger than for

deactivation by another Ar atom [136], making it a significant process within Ar-N_2 discharges.

The rate of reaction for resonant energy transfer (r_{N_2,Ar^*}) is given by Equation 4.2 [103], where $n_{Ar_m^*}$ is the metastable Ar density and n_{N_2} is the N_2 density. The rate of reaction for electron impact excitation of the $C^3\Pi_u$ state ($r_{N_2,e}$) is given by Equation 4.3, where T_e is electron temperature and n_e is the electron density [103].

$$r_{N_2,Ar_m^*} = 2.9 \times 10^{-14} \sqrt{\frac{T_g}{300}} n_{Ar_m^*} n_{N_2} \; cm^{-3} s^{-1} \tag{4.2}$$

$$r_{N_2,e} = 1.36 \times 10^{-8} T_e^{0.138} e^{\frac{-11.03}{T_e}} n_e n_{N2} \; cm^{-3} s^{-1} \tag{4.3}$$

To identify the dominant excitation process in Pocket Rocket, Equations 4.2 and 4.3 are used to calculate r_{N_2,Ar_m^*} and $r_{N_2,e}$ for varying percentages of N_2 in a 1.5 Torr total pressure Ar discharge. Electron temperature (T_e) is estimated as 2.5 eV based on previous experimental and global model results for Pocket Rocket [43]. Electron density (n_e) is estimated as 2×10^{12} cm^{-3} for pure Ar and 1×10^{12} cm^{-3} for pure N_2 based on ion saturation current (I_{sat}) measurements of 10 W discharges, made with the Langmuir probe as described in Section 3.1 biased at -28 V. A linear decrease in n_e was assumed between pure Ar and pure N_2 [100, 140].

In the absence of experimental data for Ar_m^* density, a value of 2×10^{13} cm^{-3} is used for pure Ar, based on previous works demonstrating Ar_m^* density can be up to an order of magnitude higher than n_e [123, 140]. Density of Ar_m^* is assumed to decrease by two orders of magnitude by 90% N_2 addition [140]. Using these approximations, estimates for $r_{N_2,e}$ and r_{N_2,Ar^*} for both 300 K and 1000 K with varying percent N_2 in Ar are as shown in Figure 4.1.

The electron impact excitation rate is consistently two orders of magnitude higher than excitation from quenching of Ar_m^*, supported by previous findings [88, 90]. However, electron impact excitation may be from the ground state (Equation 4.4) or from the $N_2(A^3\Sigma_u)$ metastable state (Equation 4.5), with excitation from the metastable state usually dominant over excitation from the ground state.

$$e + N_2(X^1\Sigma_g) \rightarrow e + N_2(C^3\Pi_u) \tag{4.4}$$

$$e + N_2(A^3\Sigma_u) \rightarrow e + N_2(C^3\Pi_u) \tag{4.5}$$

In discharges where the $N_2(X^1\Sigma_g)$ density is significantly higher than the $N_2(A^3\Sigma_u)$ density, then excitation through Ar_m^* quenching may become dominant over electron

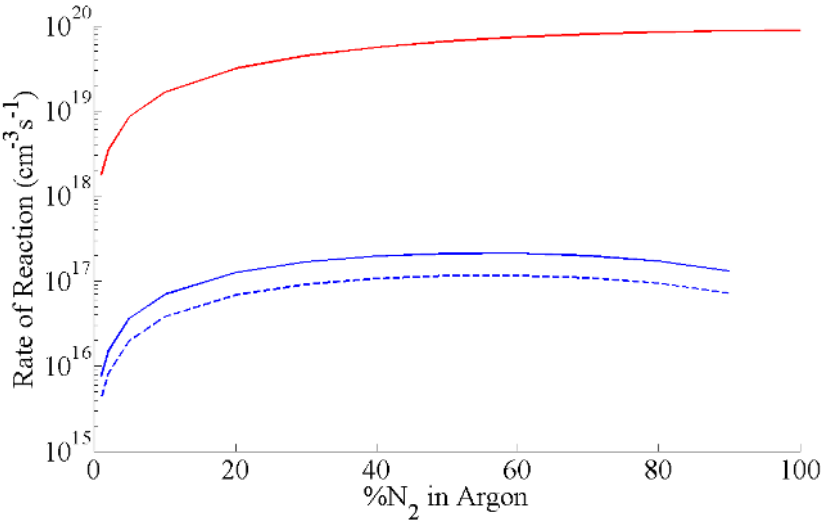

Figure 4.1: Reaction rates for excitation of N_2 $C^3\Pi_u$ state by quenching of Ar_m^* at 300 K (dashed blue line) and 1000 K (solid blue line) calculated from Equation 4.2, and electron impact (solid red line) calculated from Equation 4.3.

impact excitation. Even if that is not the case, the enhanced rotational tail from Ar_m^* quenching may still affect T_g estimated by rovibrational band matching of the N_2 SPS. The effect of this in Pocket Rocket is tested experimentally by measuring T_g of Ar discharges with varying percentages of N_2 added.

4.1.2 Experiment Parameters

Pocket Rocket is attached to a six-way vacuum chamber as described in Chapter 2. Plenum pressure is measured using a Convectron gauge and is held constant at a total pressure of 1.5 Torr for all mixtures tested. Chamber pressure, also measured with a Convectron gauge, is ~0.75 Torr for all mixtures tested giving a pressure gradient of two across the system. The percent of N_2 added to Ar is given by the partial pressures in the plenum and ranges from 1% to 100%. Nitrogen flow is controlled using a leak valve and Ar flow is controlled using a ball valve. Pre-match power is held constant at 10 W, with standing wave ratio (SWR) values around 1.1 recorded for all gas mixtures tested.

Experimental spectra used to match the simulated spectra are recorded using the monochromator and charge coupled device (CCD) setup as described in Section 3.3.3. The discharge is turned on and left to run for 20 to 30 s prior to starting the

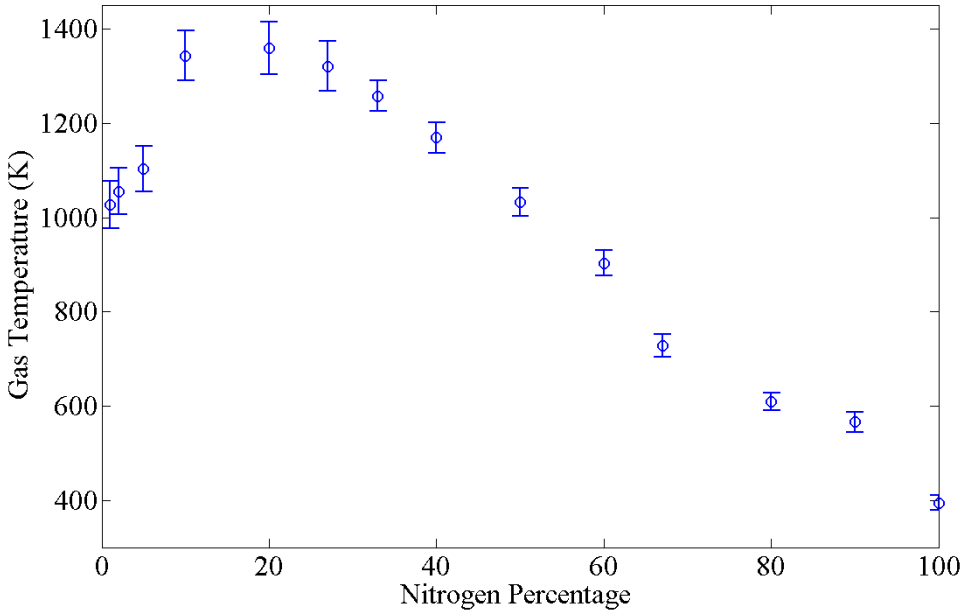

Figure 4.2: Measured gas temperature estimates using rovibrational band matching of the N_2 SPS with varying N_2 percent in an Ar discharge.

first integration to ensure steady state has been reached. Integration times range from 1000 ms for argon with 1% nitrogen (Ar with 1% N_2) to 60 ms for pure N_2, decreasing as the percentage of N_2 increases and the rovibrational signal increases. To assist in reducing noise while ensuring a sufficient rovibrational signal is captured, 30 spectra are recorded and averaged.

4.1.3 Experiment Results

Results for neutral gas temperature (T_g) measured in Ar with varying percentages of N_2 added are shown in Figure 4.2, with error bars based on a 95% confidence interval from the fitting procedure. Errors bars are larger for lower N_2 percentages as the reduced rovibrational signal results in a lower signal to noise ratio.

For 1% N_2 addition, the lowest percent addition of N_2 tested, T_g is 1030 K. Increasing N_2 to 20% increases T_g to 1360 K, the highest temperature measured. At 100% N_2, T_g has decreased to 400 K giving an asymmetric inverted parabolic trend. Previous work has shown increases in gas temperature for increasing percentages of N_2 added to Ar, with addition of 0%, 3% and 45% N_2 giving temperatures of 400-700 K in a 100 W capacitively coupled plasma (CCP) using a combination of Doppler

broadening and N_2 SPS rovibrational band fitting [103]. Enhanced thermionic emission from a titanium nozzle in a radio-frequency (RF) hollow cathode discharge with low percentage N_2 addition in Ar, caused by a small population of hot N_2 in the discharge creating Ar^*_m quenching, has also been previously noted [138].

The intensity of an Ar-N_2 spectrum is highest with 10% N_2 addition [136, 141], roughly corresponding to the highest measured T_g here at between 10% and 20% N_2. Additionally, above ∼10% N_2 the density of nitrogen ion (N_2^+) does not significantly change, but below 10% N_2, density of N_2^+ is significantly lower and is almost negligible below 5% [140]. These results suggest that the increased temperatures measured between ∼5% N_2 and 50% N_2 are enhanced by metastable quenching.

Dilute values of N_2 addition, such as 1% or 2%, produce lower gas temperature estimates than between 5% and 50% N_2. The gas temperature estimates for trace N_2 addition in argon are still higher than the values produces for pure N_2. For trace addition of N_2 in argon, the majority of ion-neutral collisions within the discharge are between argon neutrals and argon ions. Argon ion-neutral collisions are expected to produce higher hot neutral temperatures than N_2, as N_2 has six degrees of freedom for energy to be distributed between (three translational, two rotational and one vibrational), whereas argon has only three (translational) degrees of freedom. High vibrational temperatures have been noted for N_2 discharges in Pocket Rocket [63].

With a dominant, hot, population of argon neutrals within the discharge, most Ar-N_2 collisions will be thermalising neutral collisions. Resonant energy transfer collisions between Ar* and N_2 are occurring, but due to the dilute amount of N_2 will form only a small proportion of total collisions, thereby reducing the effect on the gas temperature. This is supported by the temperature increasing with N_2 addition where the Ar*-N_2 collisions become more dominant. At even higher percentages of N_2 addition, the temperature begins to decrease again as the temperature of the hot neutral population decreases due to the additional degrees of freedom in N_2 molecules.

4.1.4 Analytic Model of Ion-Neutral Charge Exchange Collisions

To confirm that the apparent higher temperature of Ar with 1% N_2 than pure N_2 measured here is a true representation of T_g and not an artefact of trace amounts of N_2 in the discharge, a simplistic model of charge exchange collisional heating is developed. The simplistic model formulated by analysing the energy exchange processes during ion-neutral charge exchange (I-N CEX) collisions is used to estimate expected T_g for pure Ar and pure N_2 discharges at 1.5 Torr and 10 W, for comparison to experimental results. The experimental results of interest are 400 K for pure N_2 at 1.5 Torr and 10 W, and 1030 K for Ar with 1% N_2 at 1.5 Torr and 10 W.

The ionisation energies of Ar and N_2 are 15.76 eV and 15.58 eV, respectively, giving 0.18 eV of excess energy during an Ar-N_2 I-N CEX collision, three orders of magnitude lower than the ion translational kinetic energy. With only 1% N_2 in the discharge the resulting effects are expected to be negligible and the pure Ar model can be compared directly to Ar with 1% N_2 experimental results.

During an I-N CEX collision with a low energy ion, it is assumed that half the kinetic energy (KE) is transferred on average from the hot ion to the cold molecule [142, 143], with KE= $\frac{1}{2}mv^2$ where m and v are the molecules mass and velocity, respectively. The initial KE of the ions is based on the Bohm velocity (v_B), calculated using Equation 1.8 as $v_{B_{Ar}} = 2450\,\mathrm{m\ s^{-1}}$ and $v_{B_{N_2}} = 2930\,\mathrm{m\ s^{-1}}$ using a T_e of 2.5 eV [43].

For an n-degree of freedom molecule, KE is related to T_g by Equation 4.6, where k is the Boltzmann constant.

$$\mathrm{KE} = \frac{n}{2}kT_g \tag{4.6}$$

Argon, being an atomic element, has three translational degrees of freedom ($n_{Ar} = 3$), whereas N_2, being a diatomic molecule, has one vibrational and two rotational degrees of freedom in addition to three translational degrees of freedom ($n_{N_2} = 6$). Using Equation 4.6, the temperature of a hot neutral particle (T_H) after an I-N CEX collision is therefore $T_{H_{Ar}} = 4980$ K and $T_{H_{N_2}} = 2640$ K.

In Pocket Rocket, the discharge is only weakly ionised (<1%) [43], so not all neutrals undergo a charge exchange collision with an ion. The fraction of cold neutrals that do undergo a charge exchange collision with a hot ion depends on the

ionisation degree and mean free path for I-N CEX collisions. Ionisation degrees ($\frac{n_i}{n_g}$) are calculated using Equation 3.1, with I_{sat} measured using the Langmuir probe as described in Section 3.1 biased at -28 V, and are $(\frac{n_i}{n_g})_{Ar} = 0.44\%$ and $(\frac{n_i}{n_g})_{N_2} = 0.19\%$.

The mean free path (λ_{mfp}) for an I-N CEX collision is given by Equation 1.14, inversely related to neutral gas density (n_g) and ion-neutral charge exchange collision cross section (σ_{CE}), taken for this work from Phelps [144] as 45 Å^2 for Ar and 40 Å^2 for N_2. Calculated λ_{mfp} is 46 μm in Ar and 40 μm in N_2, giving 90 total collisions across the discharge diameter in Ar and 80 in N_2. However, the cross sections for elastic and I-N CEX collisions are approximately equal for both Ar and N_2, meaning half the collisions are elastic, resulting in estimates of 45 and 40 I-N CEX collisions across the discharge diameter for Ar and N_2, respectively. Combining this with the measured ionisation degrees, an estimated 20% and 8% of neutrals for Ar and N_2, respectively, undergo an I-N CEX collision and become hot neutrals.

The hot and cold populations will thermalise if a sufficient number of collisions occur between hot and cold molecules in the discharge. Using Equation 1.2 for average velocity of the hot molecules (v_H) with the calculated values of T_H above gives $v_{H_{Ar}} = 1760$ m s^{-1} and $v_{H_{N_2}} = 1533$ m s^{-1}. Similarly, average velocities of the cold population molecules (v_C), assuming a temperature of 300 K, are $v_{C_{Ar}} = 432$ m s^{-1} and $v_{C_{N_2}} = 516$ m s^{-1}. Assuming the majority of neutrals become heated at the midpoint of the tube, in line with the RF electrode, there is 10 mm to travel before exiting the discharge volume, giving transit times without collisions of the hot neutrals of t_{tr}=5 ms.

The number of thermalising neutral-neutral collisions is calculated using Equation 4.7, where σ_n is the neutral-neutral collision cross section estimated as hard body sphere cross sections.

$$\tau_{n-n} = 2(v_H + v_C)n_g\sigma_n t_{tr} \tag{4.7}$$

Approximately sixty neutral-neutral collisions occur in the downstream half of the discharge tube for both Ar and N_2 which is sufficient to assume thermalisation occurs. Thermalised temperatures are $T_{Ar} = 1240$ K and $T_{N_2} = 480$ K. These values are slightly higher than, but in agreement with the measured temperature values of 1030 K and 400 K. The slight overestimates result from the broad approximations made throughout the model, particularly in regard to the fraction of energy

transferred during each collision. Importantly, the model predicts the difference in temperature between Ar and N_2 of ∼700 K and confirms experimental T_g values measured for Ar with 1% N_2 are indicative of pure Ar temperatures.

4.1.5 Alternate Rovibrational Bands

The resonant energy transfer between Ar_m^* and N_2 is confined to the SPS because of the similarity in excitation potentials. The excitation energy of the N_2 first positive system (FPS) is 3-4 eV below the Ar metastable energy, so the transfer is not resonant and is much slower than electron impact excitation. The N_2^+ first negative system (FNS) has an excitation energy of 18.7 eV, significantly higher than the Ar metastable energy. Therefore, both the N_2 FPS and N_2^+ FNS are potential alternatives to use for rovibrational band fitting to estimate T_g.

When using the N_2^+ FNS, it is required that the ion and neutral temperatures are in thermal equilibrium, which is reasonable in a highly collisional discharges as the ion-neutral mean free path is small [145]. Previous rovibrational experiments have used the N_2^+ FNS as an indication of T_g [95, 96, 105]. However, for a 1 Torr positive column discharge enclosed in an oven to provide limits for T_g estimates, values for T_g using the N_2^+ FNS were consistently 150 K too high [105]. Comparatively, values for T_g using the N_2 SPS were found to lie within the bounds given by the oven temperature. Similarly, for a dual frequency CCP at 20 mTorr, the N_2^+ FNS gave 493 K whereas the N_2 SPS gave a lower temperature of 379 K [96].

The higher temperatures estimated from the N_2^+ FNS are caused by there being two excitation channels at low pressures, being electron impact excitation of the ground state and collisions between ground state N_2^+ and neutral N_2 molecules in high vibrational states [146]. Through electron impact excitation, the light mass of the electron means the rotational distribution remains essentially the same and $T_r \approx T_g$, but collisions between heavy particles changes the rotational distribution giving a higher T_r that does not reflect T_g.

Rovibrational band fitting has also been performed using the N_2 first positive system (FPS) [98, 99, 101]. Excitation channels for the N_2 FPS are from electron impact excitation of the ground state ($N_2(X^1\Sigma_g)$ or the $N_2(A^3\Sigma_u)$ metastable state, and radiative decay from the $N_2(C^3\Pi_u)$ state [147]. The rate coefficient for popu-

lation through radiative decay is an order of magnitude lower than from electron impact excitation, and $T_r \approx T_g$.

Good agreement between T_r (and hence T_g) estimates obtained with the N_2 SPS and FPS has been demonstrated for a 1.0 Torr microwave discharge at 600 W [101]. Measured vibrational temperature (T_v) using the N_2 FPS are lower than with the N_2 SPS, as quenching and predissociation processes affect the number density of the upper vibrational states in the first positive system. The N_2 SPS is not affected as the quenching and predissociation processes occur too slowly.

When simulating a FPS rovibrational band spectrum for fitting, the triplet state fine structure must be resolved and a change from Hund's case (a) to (b) at high rotational states must be considered [98, 101]. Calculated wavelengths may have up to 0.04 nm errors which is significant in relation to the wavelength separation of the fine structure of the triplet states [97], and experimentally predetermined wavelengths are required to be used instead. This introduces additional complexity and potential sources of error when compared to simulating the N_2 SPS.

While the N_2^+ FNS and N_2 FPS may provide adequate alternatives to estimating T_g, especially in regards to Ar-N_2 discharges, the simplicity of the N_2 SPS is preferred. Based on results from Sections 4.1.3 and 4.1.4 trace amounts ($\sim$1%) of N_2 added to an Ar discharge do not significantly affect estimates for T_g, and the SPS continues to be used for temperature estimates here.

4.2 Neutral Gas Temperature Measurements

The performance of Pocket Rocket as an electrothermal thruster depends on the neutral gas temperatures reached by the propellant. To estimate performance without the need to place Pocket Rocket directly on a thrust balance, rovibrational band fitting of the N_2 SPS is used to estimate the neutral gas temperature (T_g) of N_2 and Ar with 1% N_2 discharges. The addition of 1% N_2 to the Ar discharge is required for the use of the rovibrational band fitting technique on the atomic element discharge, but has little effect on the measured temperature as discussed in Section 4.1.

4.2.1 Experiment Parameters

Measurements are performed with Pocket Rocket attached to a six-way vacuum chamber as described in Chapter 2. Plenum pressures are measured using a Convectron gauge and range from 0.5 Torr to 4.5 Torr. Chamber pressure is also measured using a Convectron gauge and a pressure gradient of two occurs across the system for all pressures tested. Pre-match power ranges from 5 W to 40 W, with SWR values around 1.1 for all runs. Nitrogen flow rates are controlled using a leak valve and Ar flow rates are controlled with a ball value. Mass flow rates are not measured directly and plenum pressures are used to parameterise the discharge.

Experimental spectra are captured using the monochromator and CCD setup described in Section 3.3. Thirty spectra are recorded and averaged to reduce noise using integration times of 200 ms for N_2 and 1000 ms for Ar with 1% N_2, where the N_2 signal is diluted. Total spectrum capture time is around 20 s for N_2 and 60 s for Ar with 1% N_2. The discharge is turned on and left to run for 20 to 30 s prior to starting the first integration to ensure steady state has been reached.

4.2.2 Nitrogen Results

Steady state volume averaged rovibrational spectroscopy results for T_v and T_r (hence T_g) for N_2 discharges ranging from 5 W to 40 W and 0.5 Torr to 4.5 Torr are shown in Figure 4.3. Errors in the measurements, based on a 95% confidence interval from the fitting procedure are $\pm$20 K for T_g and $\pm$100 K for T_v.

Measured T_g range from 350 K at 5 W and 4.5 Torr to 520 K at 40 W and 0.5 Torr. Previously, N_2 gas temperatures have been measured as $\sim$500 K for a 25 W, 1 Torr discharge at 55 kHz [82], 379 K for a 40 mTorr dual frequency CCP with high and low frequency powers of 100 W and 30 W, respectively [96], and 595 K for a 1 Torr RF glow discharge at 1 kW input power [106], in agreement with gas temperatures measured here.

Increasing the power input into the discharge increases T_g as more power is deposited in the ions resulting in more neutral gas heating. A similar increase in T_g with increasing power has also been noted in other experiments [96,101,148,149]. A slight increase in T_g with decreasing pressure is observed and is more pronounced at higher powers. Decreasing pressure is caused by a decrease in mass flow rate, which

increases the residence time of the gas in the tube. The power deposited per molecule in the discharge is therefore higher and T_g will increase slightly with decreasing pressures [150]. This has previously been noted in experiments by Huang *et al.* [96], but other experiments have noted no change in T_g with pressure [101, 148, 149]. Power deposition will saturate eventually, after which point a change in pressure will result in no change in T_g [150].

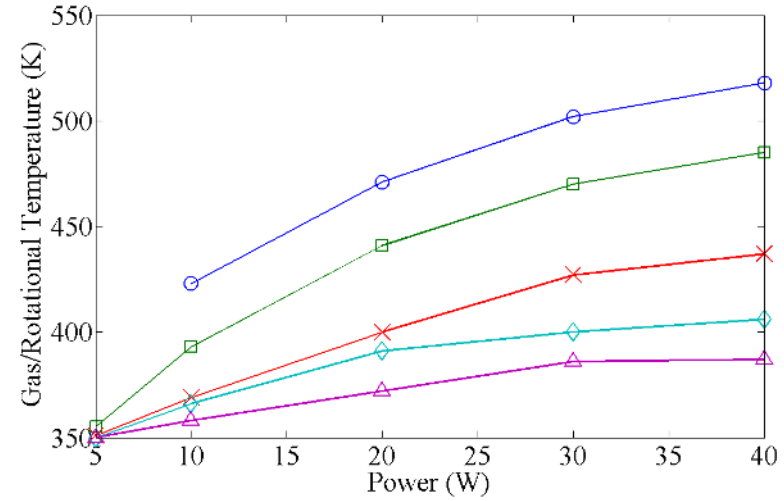

(a)

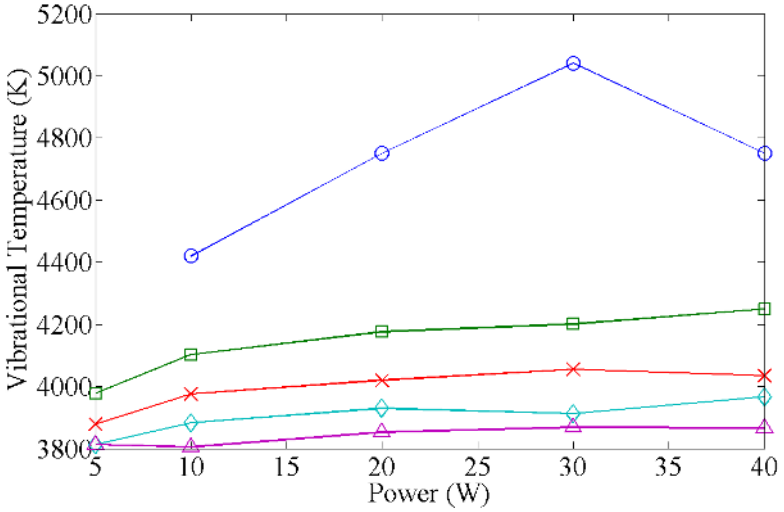

(b)

Figure 4.3: Rovibrational spectroscopy results for (a) rotational (gas) temperature and (b) vibrational temperature for N_2 discharges from 5 W to 40 W for plenum pressures of 0.5 Torr (blue circles), 1.5 Torr (green squares), 2.5 Torr (red crosses), 3.5 Torr (aqua diamonds) and 4.5 Torr (purple triangles).

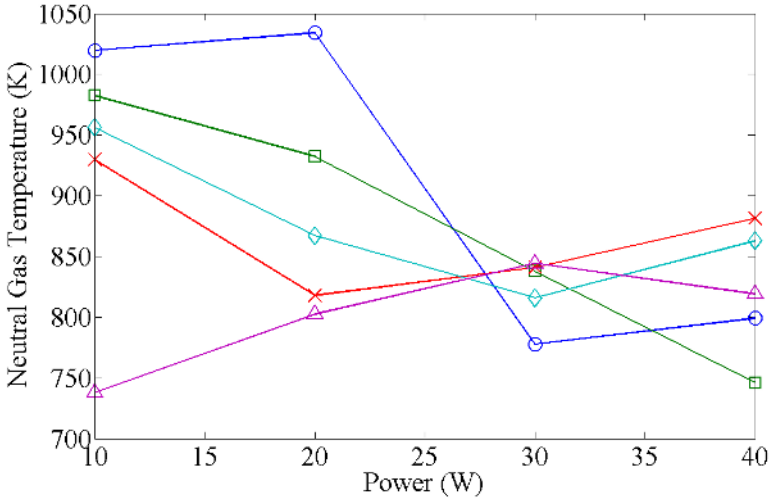

Figure 4.4: Rovibrational spectroscopy results for neutral gas temperature for Ar with 1% N_2 from 10 W to 40 W for plenum pressures of 0.5 Torr (blue circles), 1.5 Torr (green squares), 2.5 Torr (red crosses), 3.5 Torr (aqua diamonds) and 4.5 Torr (purple triangles)

Vibrational temperature (T_v) ranges from 3800 K at 5 W and 4.5 Torr to 5040 K at 30 W and 0.5 Torr. Previously, T_v in N_2 has been measured as 6000 K in a 10 mTorr helicon discharge at 600 W [97], and 3000 K for a 40 mTorr dual frequency CCP with high and low frequency powers of 100 W and 30 W, respectively [96].

Taking errors into account, increasing power has no discernible effect on T_v, while increasing pressure decreases T_v but only slightly. Decreasing T_v with increasing pressure has also been noted by Huang *et al.* [96] in a dual frequency CCP discharge. Increasing pressure decreases residence time of N_2 within the tube, potentially decreasing the amount of power deposited in the vibrational states, resulting in a decrease in T_v.

4.2.3 Argon with 1% N_2 Results

Steady state volume averaged rovibrational spectroscopy results for T_g in Ar with 1% N_2 for powers ranging from 10 W to 40 W and pressures from 0.5 Torr to 4.5 Torr are shown in Figure 4.4. Rovibrational signal strength is too low at 5 W power with only 1% N_2 for a sufficient signal to noise ratio, hence results for 5 W are not included as they are for N_2. Errors in the measurements are estimated as $\pm$75 K based on a 95% confidence interval from the fitting procedure and repeatability of experimental results in terms of variation in the percentage of N_2 added.

Neutral gas temperature (T_g) ranges from 745 K at 10 W and 4.5 Torr to 1040 K at 20 W and 0.5 Torr. Previously, Ar gas temperatures have been measured up to 1000 K in a high pressure slot discharge with 0.05% N_2 at 200-300 Torr [99] and in a 75 Torr microwave microdischarge at 6 W with 2% N_2 [31], at 600 K for a 100 W inductively coupled plasma (ICP) for pressures on the order of 0.1 Torr with 3% N_2 addition [103], and at 1900 K in a 1 Torr transformer coupled discharge (power on the order of kW) with 2.5% N_2 [93].

Large error bars in the Ar with 1% N_2 measurements (±75 K) makes identifying trends more difficult than in pure N_2, but it appears there is no discernible trend with pressure, corroborated by previous studies [99,103]. There is also no discernible trend with power suggesting power deposition into the plasma has saturated and T_g is no longer dependent on input power. A computational study of an Ar microdischarge at 30 Torr found power deposited into the plasma saturated at only 1 W [150]. Nitrogen power deposition saturates at higher powers than Ar due to the availability of rotational and vibrational levels for power to be deposited into.

4.2.4 Comparison with Analytic Model

The presence of rotational and vibrational levels in N_2 gives lower T_g than in Ar that has no rotational or vibrational states, confirmed using an simplistic analytical model in Section 4.1.4. The above results for pure N_2 and Ar with 1% N_2 also show distinctly lower gas temperatures in N_2. For completeness, rovibrational estimates for T_g are made for additional pressures between 0.5 Torr and 4.5 Torr at 10 W, and are compared to estimated values for T_g using the analytic model.

Experimental results for T_g for N_2 and Ar with 1% N_2 discharges at 10 W over a range of pressures from 0.5 Torr to 4.5 Torr are shown in Figure 4.5 with Ar with 1% N_2 shown as blue circles and N_2 shown as red squares. Error bars are included in the results and are ±15-20 K for N_2 based on a 95% confidence interval from the fitting procedure and ±75-80 K for Ar with 1% N_2 based on a 95% confidence interval from the fitting procedure and repeatability of experimental results in terms of variation in the percentage of N_2 added.

Temperature estimates from the analytic model are overlayed of Figure 4.5 as black plus symbols for Ar and grey crosses for pure N_2. Measurements of I_{sat} for

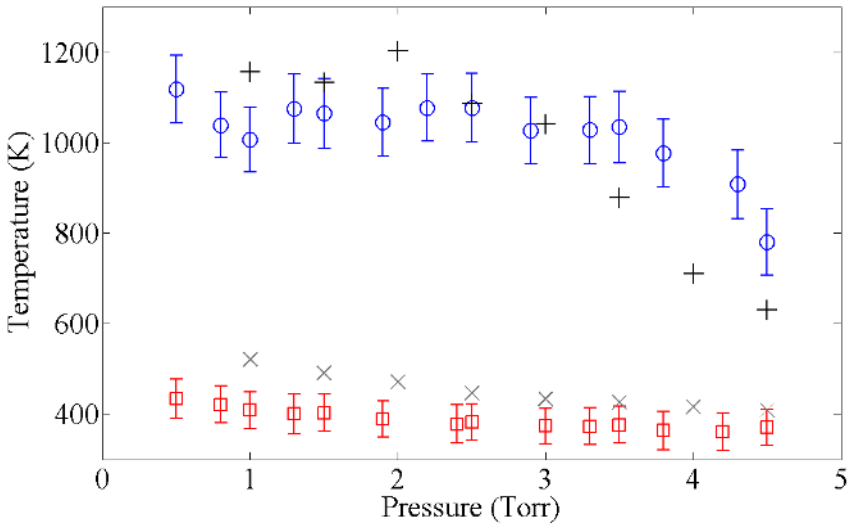

Figure 4.5: Experimental neutral gas temperature results with pressure for Ar with 1% N_2 (blue circles) and N_2 (red squares) compared to estimated neutral gas temperatures using a simplistic ion-neutral charge exchange collision model for Ar (black plus symbols) and N_2 (grey crosses) at 10 W power input.

pressures less than 1 Torr are not possible in Ar as the discharge cannot be maintained at lower pressures with the Langmuir probe in place. For N_2, the discharge cannot be maintained for pressures under 2 Torr with the Langmuir probe in place. Instead, I_{sat} for 1 Torr and 1.5 Torr in N_2 are estimated using the trend of the remaining results to allow the model to be extended down to 1 Torr for both discharge gases. Predicted T_g values are similar to the experimental results for all pressures with Ar temperatures consistently just over two times higher than the N_2 temperatures.

Predicted T_g for Ar decrease rapidly from 1200 K at 3 Torr to 780 K at 4.5 Torr. Ar discharges in Pocket Rocket with pressures less than 3 Torr have a radial electron profile with a single peak on the central axis, but as pressures increase to over 3 Torr the radial electron profile changes to an annular configuration [43]. Measurements of I_{sat} are made with the Langmuir probe inserted such that the probe tip lies on the central axis. For pressures over 3 Torr, the majority of ions are located in the annular ring with the majority of electrons and not on the central axis, resulting in underestimates of I_{sat}, hence underestimates of T_g by the model.

To confirm a similar issue is not occurring in the N_2 model, intensity profiles

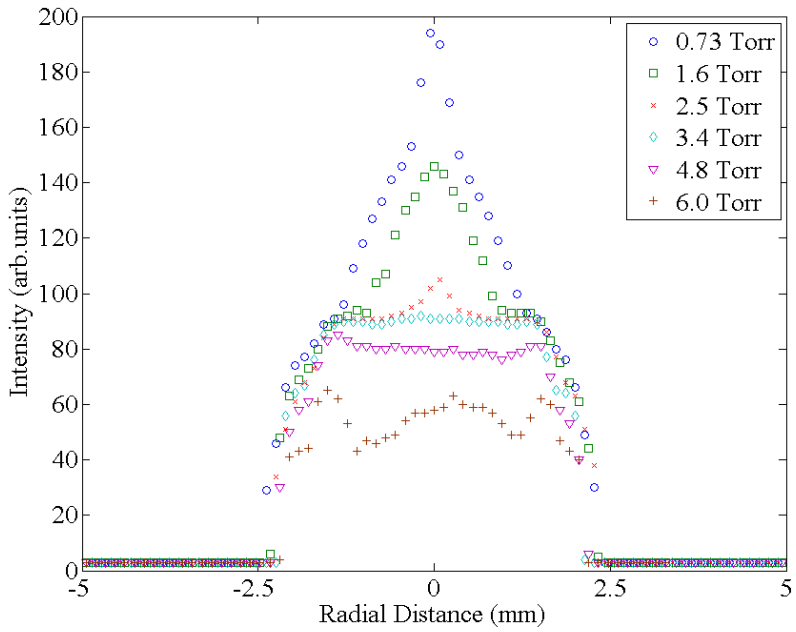

Figure 4.6: N_2^+ 391 nm emission line intensity imaged with the digital camera as a function of radial distance (from centreline) of an N_2 plasma for plenum pressures ranging from 0.73 Torr to 6 Torr at 20 W input power.

of the N_2^+ 391 nm line across the discharge diameter are measured using a digital camera in conjunction with a 390 nm filter with 10 nm bandwidth, using the method described in Section 3.2. Radial intensity profiles for a 20 W N_2 plasma are shown in Figure 4.6, and are proportional to n_e^2, where n_e is the electron density. A mode change from a central peak electron density profile to an annular electron density profile occurs at pressures above ~6.0 Torr. This is higher than pressures used for the gas temperature experiment and analytic model comparison, therefore the mode change does not affect results for N_2 discharges.

4.3 Thruster Performance Estimates

Preliminary performance estimates for thrust (T), specific impulse (I_{sp}) and efficiency (η) of Pocket Rocket are made using the measured neutral gas temperatures from Section 4.2. This is done using standard operating power of 10 W, with plenum pressures corresponding to the Paschen minimum for each propellant, being 1.5 Torr for argon and 2.5 Torr for N_2 (see Section 2.3), achieved using flow rates of 110 sccm

(3.3 mg s^{-1}) and 270 sccm (5.6 mg s^{-1}), respectively.

Measured neutral gas temperature (T_g) is used to calculate exhaust velocity (v_{ex}) using Equation 1.2, from which T and I_{sp} are calculated from Equations 1.1 and 1.4, respectively. Efficiency is calculated as $\frac{P_{rf}}{P_{pl}}$, where P_{rf} is the pre-match input RF power (10 W) and P_{pl} is the plume power. Plume power is estimated as the plume jet kinetic energy, given in Equation 4.8, where $\dot{m}$ is the mass flow rate.

$$P_{pl} = \frac{1}{2}\dot{m}v_{ex}^2 \tag{4.8}$$

A summary of the calculated performance values, and other values of interest used during calculations, are given in Table 4.1. Thrust estimated for argon is 2.4 mN and for N_2 is 3.0 mN, with specific impulses of 76 s and 55 s, respectively. The higher thrust produced by N_2 is due to the higher mass flow rate ($\dot{m}$) compared to argon to maintain the Paschen minimum pressure. This is reflected in the lower I_{sp} for N_2 when compared with argon.

Table 4.1: Preliminary performance values for Pocket Rocket calculated from measured neutral gas temperatures.

	T_g (K)	$\dot{m}$ (mg s^{-1})	v_{ex} (m s^{-1})	I_{sp} (s)	T (mN)	P_{pl} (W)	η (%)
Argon	1060	3.3	750	76	2.4	0.9	9.2
Nitrogen (N_2)	385	5.6	540	55	3.0	0.8	8.2

The substantially lower temperature of N_2 when compared with argon translates into a lower v_{ex}, but as N_2 is a lighter molecule than argon (28 g mol^{-1} compared to 40 g mol^{-1}) the difference is not as pronounced as the difference in temperatures. The plume power and efficiency of both argon and N_2 are similar, with N_2 slightly lower in each case.

Based on the above values, argon is a better propellant than N_2, as it has similar performance values for thrust and efficiency but at a lower flow rate, hence a higher I_{sp}. Lower performance from N_2 comes from power deposited in the plasma lost to internal vibrational and rotational modes, reducing the power in the plume (kinetic energy) useful for producing thrust.

For comparison, a cold gas thruster with the same dimensions as Pocket Rocket operating with argon at a flow rate of 3.3 mg s^{-1} produces 1.3 mN of thrust with an I_{sp} of 35 s. In comparison to other micro-thruster concepts, as outlined in Table 1.1, Pocket Rocket has similar thrust and specific impulse to a microwave electrothermal thruster operating with argon [31, 32], and a RF electrothermal thruster operating with argon [34]. Thrust and specific impulse values for resistojets are higher than those estimated from Pocket Rocket, but the power input requirements for resistojets are at least an order of magnitude higher [26, 27]. Performance compared to hydrazine monopropellant thrusters is substantially lower in regards to both thrust and specific impulse, but Pocket Rocket operates on green propellants.

Calculated performance estimates for thrust and I_{sp} from T_g measurements demonstrate that the Pocket Rocket concept is viable as an electrothermal plasma micro-thruster. These results are based on a preliminary, unoptimised design and could no doubt be improved upon. For optimisation of the Pocket Rocket concept, an understanding of the gas heating mechanisms is required, so that maximum propellant temperatures, hence maximum thrust and I_{sp} can be achieved.

4.4 Chapter Summary

Direct measurement of neutral gas temperature (T_g) in Pocket Rocket is made using rovibrational spectroscopy band fitting for both pure nitrogen (N_2) and argon with 1% nitrogen (Ar with 1% N_2) discharges. The following observations are noted:

- Resonant energy transfer between argon metastable atoms (Ar^*_m) atoms and N_2 molecules may affect temperature measurements for Ar-N_2 mixtures involving between 5% and 50% N_2.

- Argon gas temperatures are higher than N_2 gas temperatures as argon has only the three translational degrees of freedom for kinetic energy distribution, whereas N_2 has two rotational and one vibrational mode in addition to three translational modes for kinetic energy to be distributed between.

- Measured gas temperatures in N_2 increase with power and decrease slightly with pressure. Both increasing the power and decreasing the pressure result in

higher power deposition per molecule and higher gas temperatures. Measured gas temperatures in argon have no discernible trend with either power or pressure, with power deposition likely saturated.

- Thruster performance estimates made using the measured gas temperatures show argon is a preferable propellant over N_2, producing both higher thrust and specific impulse. Pocket Rocket operating on argon has improved performance over a cold gas thruster, and similar performance to other microwave and radio-frequency electrothermal thrusters.

Chapter 5

Spatiotemporal Study of Gas Heating Mechanisms

Neutral gas heating within the Pocket Rocket discharge was confirmed in Chapter 4 using rovibrational band fitting for both nitrogen (N_2) and argon with 1% nitrogen (Ar with 1% N_2) discharges. For standard operating conditions of 1.5 Torr plenum pressure and 10 W pre-match radio-frequency (RF) power input, the neutral gas temperature (T_g) for N_2 is 430 K, and for Ar with 1% N_2 is 1060 K. An analytic model of ion-neutral charge exchange collisions confirms that the Ar with 1% N_2 temperature is indicative of pure argon, and the difference in temperatures between N_2 and argon is attributed to a lower ionisation percent in N_2 combined with fewer internal degrees of freedom for argon atoms compared with N_2 molecules.

These results confirm neutral gas heating is occurring, but give no indication of the heating mechanisms involved. Different heating mechanisms occur over different timescales and in different physical locations within the discharge, and are therefore identifiable by performing a spatiotemporal analysis of T_g. The volume averaged temporal evolution of T_g is analysed in Section 5.2, and a full spatiotemporal study of T_g is discussed in Section 5.3. Heating of the thruster housing is analysed with a lumped thermal model in Section 5.4 and is discussed in relation to electrothermal thruster applications.

5.1 Theory of Gas Heating in a Plasma Discharge

Gas heating mechanisms within plasma discharges include both volume and surface effects. Volume heating results from energy absorbed by the plasma from the external RF field being redistributed between the electronic, translational, rotational and vibrational states of the molecules. Redistribution of energy occurs through elastic collisions [151, 152], ion-neutral charge exchange (I-N CEX) collisions [34, 36, 153], quenching of excited states [112,154], electron-ion recombination [112,151] and chemical reactions between heavy species [151]. Additionally, for diatomic molecules dissociation [112,151,152], and vibration-vibration and vibration-translation relaxation may occur [151, 154].

Being collisional effects, volume heating occurs on similar timescales to the collisional processes involved. Collisional timescales in Pocket Rocket for a 1.5 Torr discharge, calculated using Equation 1.15 using cross-section data from Phelps [144], are on the order of 100 ns for neutral-neutral collisions and 10 ns for ion-neutral collisions. Heating from collisional effects is therefore expected to occur on timescales a few orders of magnitude longer than this to allow thermal equilibrium, on the order of tens to hundreds of microseconds.

Surface or wall heating results from ion neutralisation [45], metastable quenching [151, 154] and vibrational de-excitation [151, 154] through collisions with the walls. Excess energy from the collision is transferred to the wall increasing the temperature of the surface. The heat is then transferred into the neutral gas through convection and conduction processes. As surface heating is a direct result of the temperature increase of a solid object, timescales of surface heating are substantially longer than volumetric heating, and can be on the order of tens or hundreds of seconds.

Within Pocket Rocket it is expected both volumetric and surface heating mechanisms contribute to neutral gas heating. Expected surface heating comes from ion bombardment, metastable quenching, and in the case of an N_2 discharge, vibrational deactivation on the walls. Dominant collisional mechanisms are expected to be from I-N CEX collisions, elastic collisions and momentum transfer collisions, as both N_2 and argon are inert so chemical reactions are not occurring, and for N_2 there is no

significant dissociation apparent (see Section 3.2).

Vibrational relaxation is the transfer of energy between upper vibrational and lower vibrational or translational states of a molecule. The vibrational relaxation time constant (τ_v) of simple systems can be reasonably estimated using Equation 5.1 [155], where p is the pressure in atmospheres, μ is the reduced mass of the molecule ($\mu = 14$ for N_2), and θ is the characteristic vibrational temperature (θ=3395 K for N_2 [155]).

$$\ln(p\tau_v) = (1.16 \times 10^{-3})\mu^{\frac{1}{2}}\theta^{\frac{4}{3}}(T_g^{-\frac{1}{3}} - 0.015\mu^{\frac{1}{4}}) - 18.42 \tag{5.1}$$

Using Equation 5.1 with a temperature of 1000 K, $\tau_v \approx 30$ s. However, transit time of the gas through the tube is on the order of 100 ms based on the gas travelling at the sound speed (343 m1s^{-1}). Therefore any relaxation effects occur on timescales much longer than the time the gas spends in the tube and resultant heating effects are expected to be minimal.

5.2 Temporal Evolution of Gas Temperature

The large difference in time scales between volumetric and surface heating means the overall contribution from each effect can be determined by recording the temporal evolution of temperature to extract the time constants of heating. The time constant (τ) of heating is the time taken for the temperature to rise to $1 - \frac{1}{e}$ of the final value for heating, or conversely for cooling, the time taken for the temperature to decrease by $\frac{1}{e}$, assuming uniform heating or cooling of a body. By measuring the temporal evolution of temperature, then fitting lines of the form shown in Equation 5.2a for heating and Equation 5.2b for cooling, where T_0 is the initial temperature and ΔT is the total temperature change, the relative contributions from volumetric and surface heating can be separated and identified.

$$T = T_0 + \Delta T(1 - e^{-\frac{t}{\tau}}) \tag{5.2a}$$

$$T = T_0 + \Delta T e^{-\frac{t}{\tau}} \tag{5.2b}$$

5.2.1 Experiment Parameters

The temporal evolution of temperature within Pocket Rocket over the first 300 s of operation is measured using the same rovibrational spectroscopy technique described in Section 3.3 and used throughout Chapter 4. The discharges analysed are pure N_2 and argon with 10% nitrogen (Ar with 10% N_2) at 1.5 Torr total plenum pressure with pre-match input power of 60 W. The higher input power of 60 W provides stronger light emission from the plasma, reducing integration times and giving better temporal resolution. Similarly, 10% N_2 is added to argon, rather than 1% as in Section 4.2, as 1% does not provide sufficient rovibrational signal for fitting at high temporal resolution. This means the effect of argon metastable atoms may influence the results as discussed in Section 4.1 and the absolute values of temperature recorded may not be entirely accurate; however, assuming the metastable argon population density is constant over time the evolution of temperature is still able to be analysed correctly.

Temporal evolution is captured through the use of a specially written Labview program to simultaneously control the RF power generator and charge coupled device (CCD) array and synchronise the initiation and duration of the discharge with the integration timing of the CCD array. Two different timing techniques are used to capture temporal evolution over seven orders of magnitude, from 50 μs to 300 s.

From 50 μs to 20 ms light intensity from a single pulse gives insufficient rovibrational signals for fitting. Instead, the CCD array is integrated continuously for 500 ms while the discharge is pulsed for the duration of interest, capturing light output from multiple pulses. A 2.5% duty cycle ensures no residual heat is left in the system between pulses, confirmed by recording the plenum pressure with a 10 Torr range Baratron gauge over multiple pulses, as shown in Figure 5.1. The plenum pressure returns to the original level after each pulse, confirming residual heat is not left in the system.

For the 50 ms to 300 s time range, the discharge is operated in continuous mode while the CCD array records short duration integrations at 168 set times. The procedure is repeated ten times, averaging the recorded spectra to reduce the effect of noise. The Labview program ensures the 300 s pulse is initiated simultaneously with the first CCD integration window to maintain constant timing throughout each

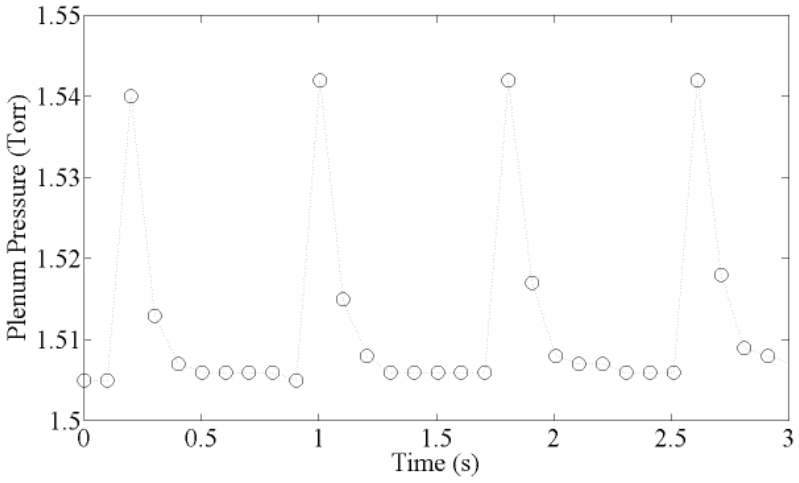

Figure 5.1: Plenum pressure recorded at 100 ms intervals during 10 ms pulses with a duty cycle of 2.5% for a 1.5 Torr, 60 W argon with 10% N_2 discharge.

repetition.

Integration time is chosen to be 8 ms for pure N_2 and 100 ms for Ar with 10% N_2. The longer integration time for Ar with 10% N_2 is necessary as the diluted amount of N_2 produces a significantly weaker rovibrational signal than a pure N_2 discharge. Spectrum capture times are weighted to be more frequent during the early stages of discharge operation where it is expected temperature will change more rapidly, ranging from every 50 ms for N_2 or every 200 ms for Ar with 10% N_2 during the first second of operation, to every 5 s after 60 s of operation for both gas mixtures.

5.2.2 Temporal Results

Results for the temporal evolution of T_g (blue circles - taken to be the same at rotational temperature (T_r)) and vibrational temperature (T_v) (red squares) in a 1.5 Torr, 60 W, N_2 discharge are shown in Figure 5.2 using a log scale for time to clearly show the full seven order of magnitude captured. The times represent the length of time from the commencement of the RF generator ramping, and not from plasma breakdown. Using this timescale, plasma breakdown occurs at approximately ∼40 μs, shown in Figure 5.2 as a dashed black line. Error bars included in Figure 5.2 for both T_g and T_v are based upon 95% confidence intervals from the fitting procedure.

An increase in T_v to ∼3900 K occurs within the first 10 ms before remaining at a

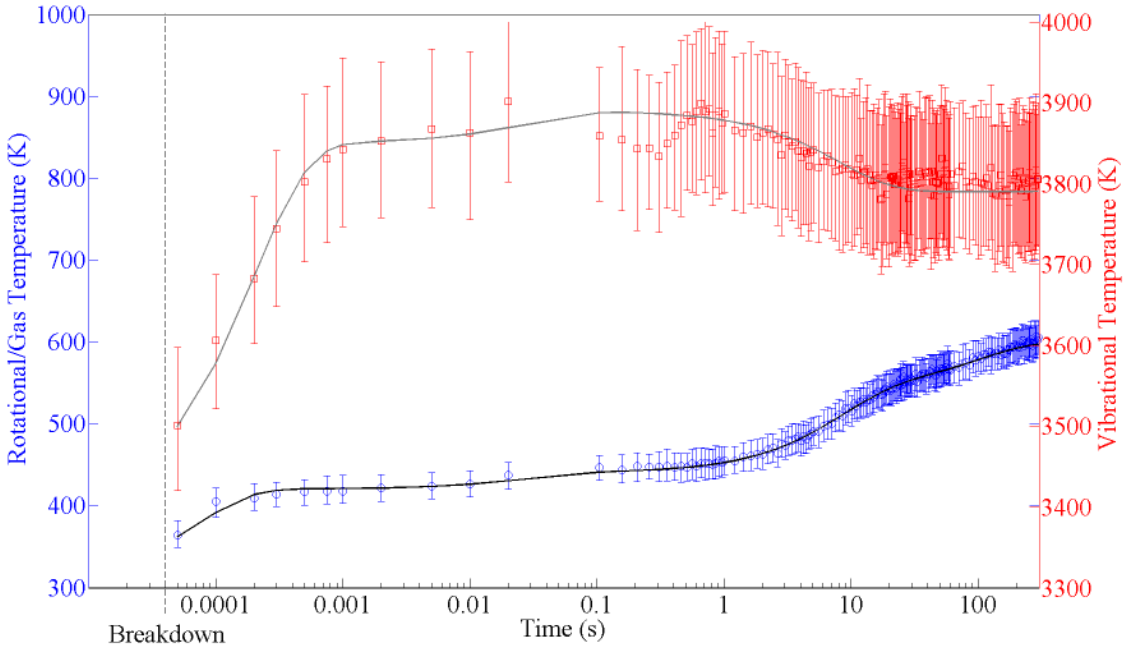

Figure 5.2: Temporal evolution of T_g (or T_r) (blue circles) and T_v (red squares) for a 60 W, 1.5 Torr N_2 discharge. Overlayed on the data are fit lines for T_g (solid black line - Equation 5.4) and T_v (solid grey line - Equation 5.3).

similar temperature for the remainder of the 300 s operation, with a possible slight decrease of ∼100 K between 1 and 10 seconds. The time constant fit equation for T_v is given by Equation 5.3 and is shown in Figure 5.2 as a solid red line overlayed on the experimental data. A temperature of 3395 K is taken for T_{v0} (first term of the right hand side (RHS) of Equation 5.3) to match the characteristic ground state vibrational temperature of N_2 [155].

$$T_v = 3395 + 450(1 - e^{-\frac{t}{2\times10^{-4}}}) + 100(e^{-\frac{t}{8}}) \tag{5.3}$$

Temporal evolution of T_v exhibits one heating period with $\Delta T_{v1} = +450$ K and $\tau_{v1} = 2 \times 10^{-4}$ s or 200 μs (second term of the RHS of Equation 5.3) and one cooling region with $\Delta T_{v2} = -100$ K and $\tau_{v2} = 8$ s (last term of the RHS of Equation 5.3). Electron impact excitation of the vibrational states results in the initial fast heating with $\tau_{v1} = 200$ μs. The cooling is possibly due to vibrational relaxation, although as discussed in Section 5.1 is unlikely to be a noticeable effect here due to transit time in the tube being significantly shorter than the relaxation timescales. Error bars for T_v are large enough that the apparent decrease in temperature occurs entirely within the error scale, and may not actually exist.

A sharp increase in T_g to ∼420 K occurs within the first 200 μs, followed by a slower increase to the final measured T_g of 580 K at 300 s. These results are in agreement with previous results that measured a steady state N_2 gas temperature of ∼480 K for 40 W input power (see Section 4.2). This experiment was performed at higher power (60 W) to give sufficient signal strength with shorter integration times, explaining the slightly higher temperature measured here.

The time constant fit equation for T_g in N_2 is given by Equation 5.4 and is overlayed on the data in Figure 5.2 as a solid black line. Ambient temperature (300 K) is chosen for T_{g0} (first term of the RHS of Equation 5.4).

$$T_g = 300 + 140(1 - e^{-\frac{t}{8\times10^{-5}}}) + 100(1 - e^{-\frac{t}{8}}) + 60(1 - e^{-\frac{t}{100}}) \tag{5.4}$$

Neutral gas temperature in N_2 exhibits three heating periods, the first with $\Delta T_{g1} = 140$ K and $\tau_{g1} = 8 \times 10^{-5}$ s or 80 μs (second term of the RHS of Equation 5.4), the second with $\Delta T_{g2} = 100$ K and $\tau_{g1} = 8$ s (third term of the RHS of Equation 5.4), and the third with $\Delta T_{g3} = 60$ K and $\tau_{g3} = 100$ s (fourth term of the RHS of Equation 5.4). As with the fast heating of the vibrational states, the fast gas heating ($\tau_{g1} = 80$ μs) is likely from collisional processes within the discharge.

The initial rise in T_g in Pocket Rocket occurs approximately three times faster than the initial increase in T_v from electron impact vibrational excitation. The cross section for I-N CEX collisions between a nitrogen ion (N_2^+) and N_2 molecule is $\sim10^{-14}$ cm^2 [144], and the cross section for vibrational excitation of N_2 by electron impact is $\sim10^{-20}$ cm^2 [156]. Therefore the collision frequency of I-N CEX collisions will be higher than that for vibrational excitation by electron impact and the resulting heating will occur faster as demonstrated.

The rise time of the RF generator used here is ∼70 μs with plasma breakdown occurring approximately 45 μs into the RF pulse. This is seen in Figure 5.3, showing the normalised RF voltage envelope measured post-match during an 800 ms pulse (panel (a)), corresponding photodiode signal of discharge light emission (panel (b)) and ion saturation current (I_{sat}) measured with the Langmuir Probe as discussed in Section 3.1 biased at -29 V (panel (c)). The measured fast initial increase in T_g occurs on the same timescale as the rise time of the RF generator. So although heating is likely caused by elastic and I-N CEX collisions within the discharge occurring on timescales at or below that of the RF generator rise time, the exact time constant

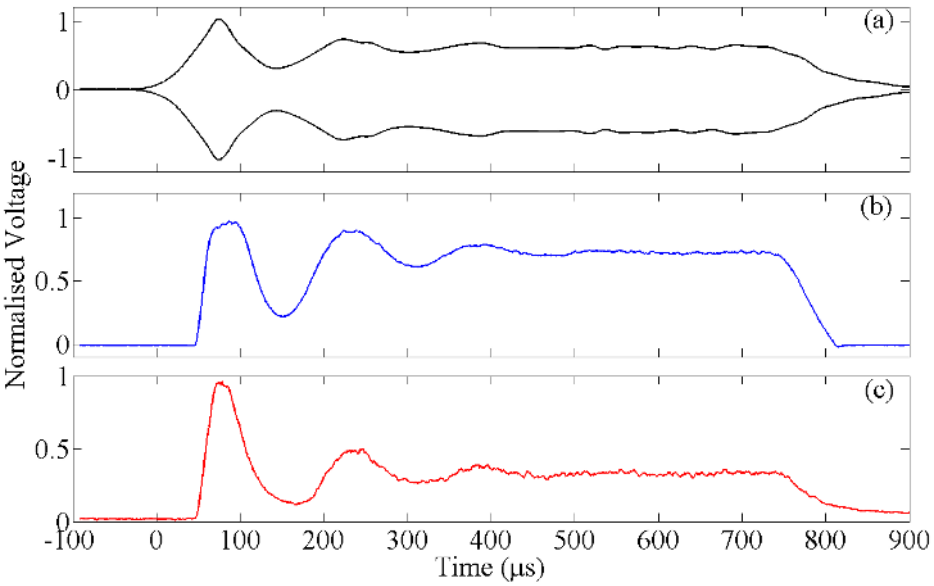

Figure 5.3: Breakdown in the Pocket Rocket device during an 800 μs pulse showing (a) normalised RF voltage envelope post match, (b) normalised photodiode signal of discharge light emission and (c) normalised ion saturation current measured with a Langmuir Probe.

is impossible to determine with the current experimental setup.

The intermediate heating with $\tau_{g2} = 8$ s, corresponds with the decrease in T_v of 100 K with $\tau_{v2} = 8$ s (third term of the RHS of Equation 5.3), seemingly supporting a transfer of energy from vibrational to translational states. However, as the transit time through the tube is much shorter than this, any correspondence is likely a coincidence. Both the intermediate heating and slow heating mechanisms ($\tau_{g2} = 8\ s$ and $\tau_{g3} = 100\ s$, respectively) have time constants longer than the transit time of the gas in the tube (∼100 ms) and are likely from heating of the thruster tube and housing or related effects. A similar increase on these slower time scales is not seen for T_v, as vibrational states are excited only through electron impact processes and not from surface heating effects.

Results for the temporal evolution of T_g in Ar with 10% N_2 are shown in Figure 5.4 with error bars estimated from a 95% confidence interval from the fitting procedure and repeatability of experimental results in terms of variation in the percentage of N_2 added. Conversely to the pure N_2 results, a decrease in temperature

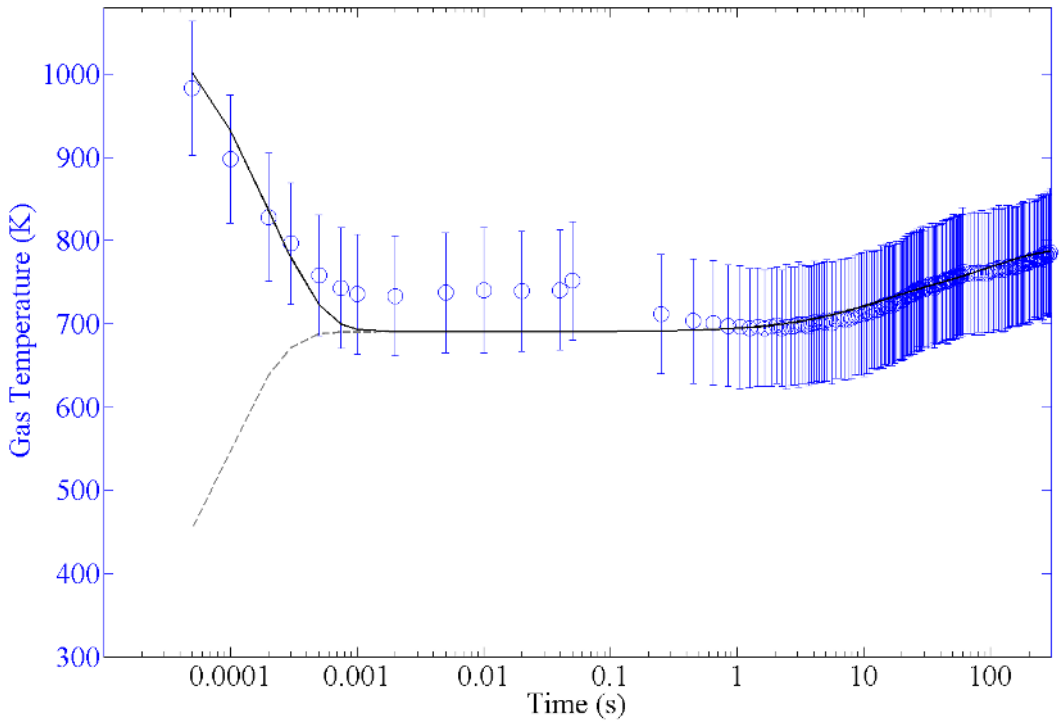

Figure 5.4: Temporal evolution of T_g for a 60 W, 1.5 Torr argon with 10% N_2 discharge. Overlayed on the data are fit lines given in Equation 5.5 (solid black line) and Equation 5.6 (dashed grey line).

from 1000 K to around 700 K occurs within the first millisecond, followed by a slow increase in T_g similar to that seen in pure N_2. The final temperature measured after 300 s is 790 K, consistent with previous T_g measurements from Section 4.2 of an Ar with 1% N_2 discharge at 1.5 Torr.

Although the decrease in T_g within the first millisecond is a repeatable experimental result, no logical explanation can be provided as to why this might be physically occurring, and instead it is assumed to be an aberration of the rovibrational band fitting method, possibly related to a settling time for electron impact and metastable resonant energy transfer balance, or the metastable population density changing significantly within the first millisecond. A spike in impedance, hence post-match voltage, is observed during breakdown for Ar with 10% N_2, which is not as pronounced in pure N_2 discharges, but this is still not enough to account for the reversal in trend for T_g in the first millisecond.

The time constant fit line for T_g in Ar with 10% N_2 is given in Equation 5.5 and

is overlayed on the data in Figure 5.4 as a solid black line. The initial temperature of 690 K (first term on the RHS of Equation 5.5) is chosen arbitrarily to allow for the initial decrease in temperature to be fitted, and the second term on the RHS accounts for the initial decrease in T_g.

$$T_g = 690 + 380e^{-\frac{t}{1\times10^{-4}}} + 40(1 - e^{-\frac{t}{10}}) + 60(1 - e^{-\frac{t}{100}}) \tag{5.5}$$

A second time constant fit line for T_g in Ar with 10% N_2 ignoring the initial increase in temperature in the first millisecond is given in Equation 5.6 and is overlayed on the data in Figure 5.4 as a dashed grey line. Here, the initial temperature is assumed to be ambient T_0=300 K (first term on the RHS) and a fast increase in temperature with the same time constant as the fast heating in pure N_2 of 80 μ s is assumed.

$$T_g = 300 + 390(1 - e^{-\frac{t}{8\times10^{-5}}}) + 40(1 - e^{-\frac{t}{10}}) + 60(1 - e^{-\frac{t}{100}}) \tag{5.6}$$

Regardless of the treatment of the initial settling period, T_g in Ar with 10% N_2 exhibits similar behaviour to T_g in pure N_2 after $\sim$1 ms. There are two distinct heating periods with time constants $\tau_2 = 10$ s and $\tau_3 = 100$ s, respectively (last two terms in Equations 5.5 and 5.6). This suggests that after the initial settling period, the Ar* density is not changing significantly and the temporal evolution results at longer times are unaffected.

Being a mostly atomic element discharge, heating from vibrational relaxation should not be significant here, confirming that the intermediate heating is not from relaxation processes within the discharge, supporting the hypothesis that the intermediate and slow heating processes are surface heating effects. To further investigate the heating mechanisms and confirm if the intermediate and slow heating are surface effects, a spatiotemporal profile of temperature in Pocket Rocket is captured and analysed.

5.3 Spatiotemporal Gas Temperature

The spatial profile of temperature indicates in which physical locations each heating mechanism is dominant. Volumetric processes should occur uniformly throughout the volume, whereas surface heating processes are localised to regions near hot walls.

Here, spatiotemporal studies of T_g, T_r and T_v in a 1.5 Torr, 60 W, N_2 discharge, and T_g in a 1.5 Torr, 60 W, Ar with 10% N_2 discharge in Pocket Rocket are performed to confirm the suggested heating mechanisms identified in the volume average temporal study in Section 5.2.

5.3.1 Experiment Parameters

The experimental setup used is the same as previously described for the temporal evolution study in Section 5.2, with a set of baffles used to restrict the optical image and separate heating mechanisms occurring in the central bulk discharge region and near the thruster walls. Three regions of interest are analysed to allow temperature measurements both in the centre of the discharge and near the walls. Using the convention of the axial centreline of the thruster as r=0 mm the three regions are (1) the centre of the discharge (r_1=0-1.1 mm), (2) a broad annular region near the walls encompassing the sheath and some of the plasma bulk (r_2=0.8-2.1 mm), and (3) a narrow annular region near the walls (r_3=1.4-2.1 mm) encompassing just the sheath region based on previous estimates for sheath width of 0.6 mm [64]. The broad wall region is used in addition to the narrow region for comparison, as the brightness of the discharge in the sheath region is significantly lower than in the plasma bulk, and noise in the rovibrational spectra may introduce errors in the temperature estimates.

To isolate the regions of interest opaque disks constructed from thin (∼1-2 mm thick) aluminium with (1) a 0.5 mm diameter central hole, (2) an annular ring with 1 mm inner diameter and 1.5 mm outer diameter, and (3) an annular ring with 1.5 mm inner diameter and 2.25 mm outer diameter are placed over the plenum viewport. When used in conjunction with the 4 mm diameter optical fibre placed 13 cm to the rear of the plenum window, these disks isolate the discharge regions of interest as shown in Figure 5.5 (drawn to scale but resized in the vertical direction here for clarity). The discharge volume is spatially resolved across the radius, but it is not resolved axially. However, the main plasma bulk forms a peak with a full width half maximum of less than 0.5 mm [43, 61] at the axial mid-point of the discharge tube (4 cm from the opaque disks as noted in Figure 5.5), and the majority of the light emission is expected to come from this relatively narrow axial region.

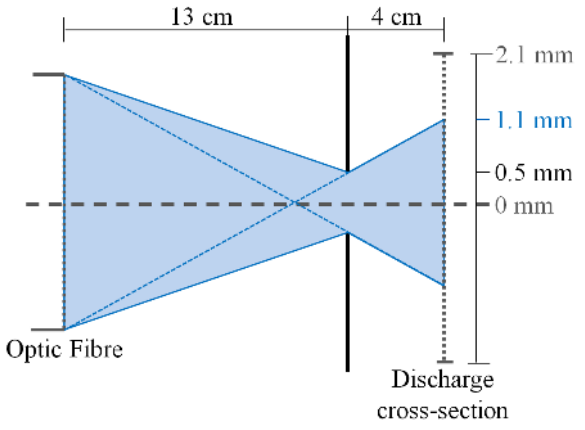

(a)

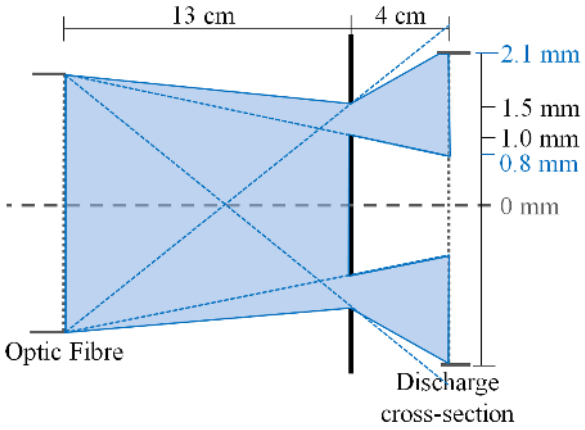

(b)

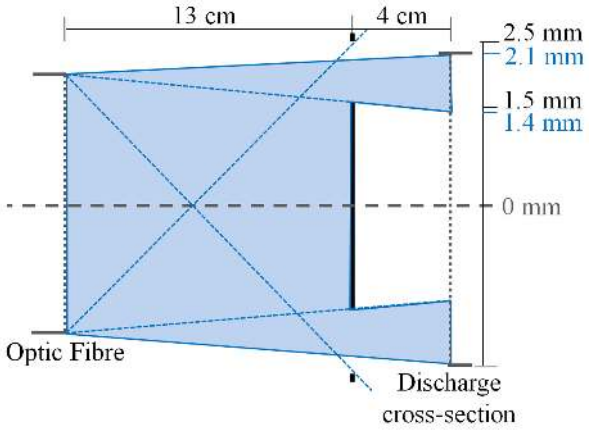

(c)

Figure 5.5: Optical ray diagrams showing spatial regions of interest for (a) 0-0.5 mm radius circular mask giving a region of interest $r_1 = 0 - 1.1\ mm$, (b) 1-1.5 mm radius annular mask giving a region of interest $r_2 = 0.8 - 2.1\ mm$ and (c) 1.5-2.25 mm radius annular mask giving a region of interest $r_3 = 1.4 - 2.1\ mm$ (drawn to scale but resized in the vertical direction for clarity here).

Temporal evolution is captured using the same Labview control program described in Section 5.2, but reduced light emission from blocking part of the discharge requires longer integration times and reduces temporal resolution. Spectra are recorded every 5 seconds for the first 100 seconds of continuous mode operation, with an integration time of 1 s to allow sufficient light to be collected. The procedure is repeated eight times and averaged to reduce noise. Temperature data on the order of microseconds is not achievable due to diminished light from blocking large sections of the discharge emission.

5.3.2 Spatiotemporal Results

Spatiotemporal results for T_v and T_g (taken to be the same as T_r) in N_2 are shown in Figures 5.6(a) and 5.6(b), respectively, and for T_g in Ar with 10% N_2 in Figure 5.6(c). Measured temperatures at each spatial and temporal co-ordinate recorded are shown as filled circles, with corresponding error bars based on a 95% confidence interval from the fitting procedure shown as thin black lines. Each region is given a single spatial co-ordinate for the purposes of plotting, and are defined as 0 mm for the central circular region of interest (r_1), and half the difference between the inner and outer diameters for the annular regions of interest, being 1.45 mm for r_2 and 1.75 mm for r_3. Colours indicating temperature and an extrapolated grid connecting the measurement points are also included as visual aids.

Vibrational temperatures for N_2, shown in Figure 5.6(a), range from 3810 K to 3980 K in agreement with previous volume averaged temporally resolved T_v measurements in Section 5.2 (see Figure 5.2) where T_v ranged from 3780 K to 3900 K between 1 s and 100 s. Taking uncertainties into account, T_v is approximately constant over the entire spatiotemporal profile. Excitation of vibrational states of N_2 in this system occurs only through electron impact excitation so T_v is expected to be reasonably constant throughout the discharge volume, and after one second has reached the equilibrium temperature. The lack of a decrease in T_v near the walls when compared to the central bulk of the discharge suggests that vibrational de-excitation on the walls is not a dominant process. This is supported by a low accommodation coefficient for vibrational de-excitation for N_2 on alumina of 1.2×10^{-3} [157].

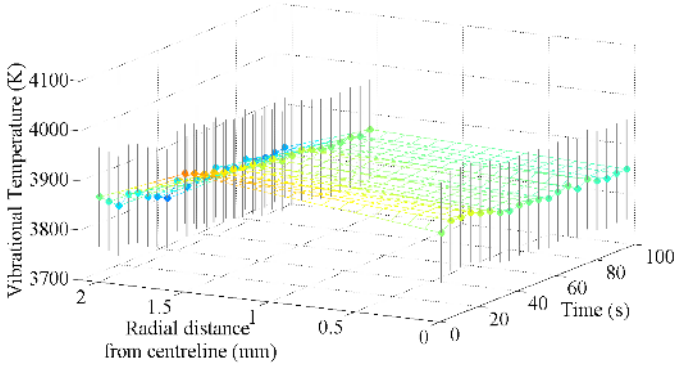

(a)

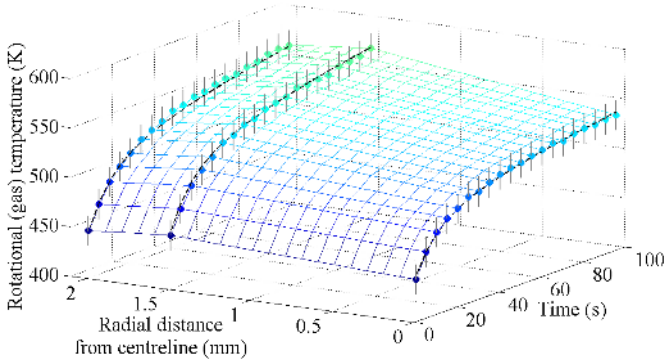

(b)

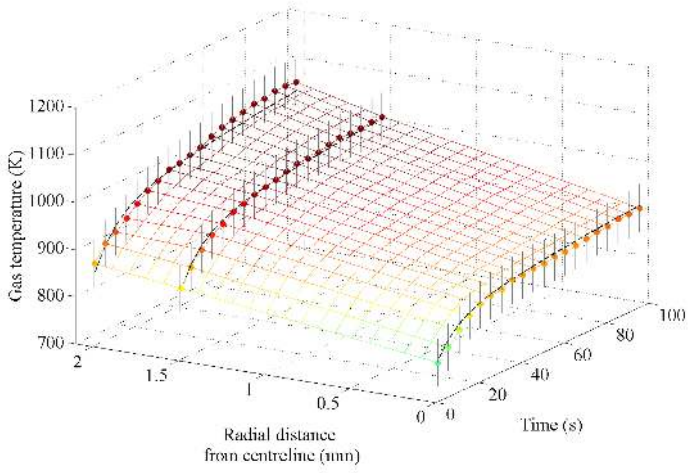

(c)

Figure 5.6: Spatiotemporal profiles of (a) T_v in N_2, (b) T_g in N_2 and (c) T_g in argon with 10% N_2, during the first 100 s of operation at 60 W and 1.5 Torr. Measured temperatures are filled circles with colouring indicative of temperature. Error bars are shown as thin black lines and an extrapolated grid is included for clearer visualisation of the data. Thicker dashed black lines in (b) and (c) represent fit lines for T_g given in Equations 5.4 and 5.5, respectively.

Neutral gas temperature (T_g) for N_2, taken to be the same as T_r, is shown in Figure 5.6(b). Within the first 1 s of operation, T_g rises to between 440 K and 460 K across the entire radius, in excellent agreement with the volume averaged result of 450 K after 1 s of operation (see Figure 5.2). After 100 s, the temperature near the walls has risen to 570 K, while the temperature in the centre of the discharge has risen to a lower value of 535 K. Both these results are slightly lower than the volume averaged result of 580 K at 100 s (see Figure 5.2) but are still in reasonable agreement.

For argon with 10% N_2 the spatiotemporal profile of T_g is shown in Figure 5.6(c). During the first 1 s of operation the temperature has risen to between 790 K and 860 K across the entire radius. The measurements are in good agreement with each other to within uncertainties but are slightly higher than the volume averaged temporal result of 700 K after 1 s of operation (see Figure 5.4). After 100 s, the temperature near the walls has risen to 1060 K, while the temperature in the centre of the discharge has risen to a lower value of 910 K, again higher than the volume averaged result of ∼800 K.

The contribution to T_g from each heating mechanism is estimated by fitting lines of the form shown in Equation 5.2 to the data for each spatial region of interest. Fit lines are not included for T_v in N_2 as the only heating is from electron impact excitation of vibrational states, occurring on timescales faster than 1 s which is not resolved here.

For N_2, the fit lines for T_g are given in Equation 5.7 and are overlayed on the experimental data in Figure 5.6(b) as dashed black lines, with T_{g1-N_2} the gas temperature in region r_1, T_{g2-N_2} the gas temperature in region r_2 and T_{g3-N_2} the gas temperature in region r_3. Fast heating (<1 s) cannot be resolved using the present experimental data as the first measurement occurs at 1 s, so the same values as previously measured in the volume averaged temporal evolution study ($\tau_{1_{N_2}} = 80$ μS and $\Delta T_{1_{N_2}} = 140$ K) from Equation 5.4 is assumed for all three regions instead.

$$T_{g1-N_2} = 300 + 140(1 - e^{-\frac{t}{8\times10^{-5}}}) + 50(1 - e^{-\frac{t}{10}}) + 80(1 - e^{-\frac{t}{100}}) \quad (5.7a)$$

$$T_{g2-N_2} = 310 + 140(1 - e^{-\frac{t}{8\times10^{-5}}}) + 60(1 - e^{-\frac{t}{10}}) + 100(1 - e^{-\frac{t}{100}}) \quad (5.7b)$$

$$T_{g3-N_2} = 300 + 140(1 - e^{-\frac{t}{8\times10^{-5}}}) + 60(1 - e^{-\frac{t}{10}}) + 100(1 - e^{-\frac{t}{100}}) \quad (5.7c)$$

Similar fit lines for each spatial region in Ar with 10% N_2 are shown in Equation

5.8 and are overlayed on the experimental data in Figure 5.6(c) as dashed black lines, with T_{g1-Ar} the gas temperature in region r_1, T_{g2-Ar} the gas temperature in region r_2 and T_{g3-Ar} the gas temperature in region r_3. Again, fast heating below 1 s is not directly resolved here, and $\tau_{1_{Ar}} = 80\ \mu s$, is approximated from volume averaged temporal data in Section 5.2 (Equation 5.6) for all three spatial regions.

$$T_{g1-Ar} = 300 + 480(1 - e^{-\frac{t}{8\times10^{-5}}}) + 80(1 - e^{-\frac{t}{10}}) + 90(1 - e^{-\frac{t}{100}}) \quad (5.8a)$$

$$T_{g2-Ar} = 300 + 540(1 - e^{-\frac{t}{8\times10^{-5}}}) + 120(1 - e^{-\frac{t}{10}}) + 100(1 - e^{-\frac{t}{100}}) \quad (5.8b)$$

$$T_{g3-Ar} = 300 + 540(1 - e^{-\frac{t}{8\times10^{-5}}}) + 120(1 - e^{-\frac{t}{10}}) + 130(1 - e^{-\frac{t}{100}}) \quad (5.8c)$$

In both N_2 and Ar with 10% N_2, there are three distinct gas heating mechanisms for each spatial region, identified by the time constants $\tau_1 = 80\ \mu$s, $\tau_2 = 10$ s and $\tau_3 = 100$ s, from the second, third and last terms, respectively, on the RHS of Equations 5.7 and 5.8. The intermediate and slow time constants, (τ_2 and τ_3) are similar to those previously found for the volume averaged temporal results of $\tau_2 = 8$ s and $\tau_3 = 100$ s in N_2 (see Equation 5.4) and $\tau_2 = 10$ s and $\tau_3 = 100$ s in Ar with 10% N_2 (see Equation 5.6). The time constants are the same for all spatial co-ordinates as expected, as the same three dominant heating mechanisms are present throughout the volume. The change in temperature associated with each mechanism varies slightly depending on location, as different heating mechanisms may be dominant in certain physical locations.

Volume heating from I-N CEX is expected to be fairly uniform over the discharge volume, which is demonstrated in both N_2 and Ar with 10% N_2 by the uniform radial profile of temperature at 1 s and similarity in ΔT_1 and τ_1 for each of the fit lines applied (second terms on the RHS of Equations 5.7 and 5.8), confirming the fast heating is from collisions within the discharge. Both the intermediate and slow heating mechanisms with τ_2=10 s and τ_3=100 s are more pronounced near the wall regions in both N_2 and Ar with 10% N_2 supporting the surface heating hypothesis.

5.4 Heating of the Thruster Housing

Various components of the thruster and housing are constructed from different materials with different density (ρ), specific heat (c_p) and thermal conductivity (k)

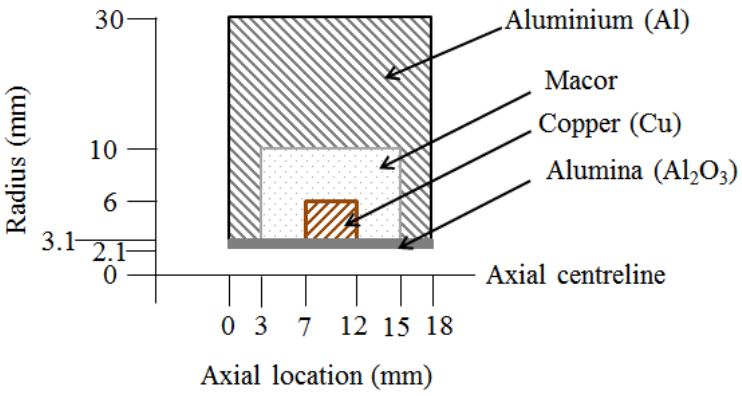

Figure 5.7: Component dimensions for Pocket Rocket housing used to calculate the heating time constants.

Table 5.1: Thermal properties of Pocket Rocket component materials.

	Al_2O_3	Cu	Macor	Al
ρ [kg m^{-3}]	3950	8960	2520	2700
c_p [J/kg-K]	880	386	790	900
k [W/m-K]	30	400	2	230

that may heat at different rates. To investigate heating of the thruster housing and the resulting effect on propellant (gas) heating, a lumped thermal model approach is used. Thruster housing dimensions are shown in Figure 5.7, and the associated material properties are listed in Table 5.1.

There are three possible thermal paths for heat flow from the inner alumina tube surface through the housing to the external environment. These are (1) through the alumina tube, copper electrode, Macor casing and aluminium housing, (2) through the alumina tube, Macor casing and aluminium housing, or (3) through the alumina tube and aluminium housing directly.

The majority of the heat will flow through the path with the least thermal resistance. Thermal resistance is given by Equation 5.9, where k is thermal conductivity, and L is the length and A is the cross-sectional area through which the heat flows [158].

$$R = \frac{L}{kA} \tag{5.9}$$

Thermal resistances in series add in the same manner as electrical resistances, so the total thermal resistance through each of the three possible paths is the sum

of the resistance through each individual component. Using the dimensions given in Figure 5.7 and thermal conductivities given in Table 5.1, total thermal resistances are $R_1 = 4.7$ K W^{-1}, $R_2 = 28.3$ K W^{-1} and $R_3 = 0.22$ K W^{-1} for paths one, two and three above, respectively. The thermal resistance through path three is significantly lower than the other two paths that involve passing through Macor which is an excellent thermal insulator, hence the majority of the heat flow through the housing will be through the alumina tube and aluminium housing directly. The lumped thermal model of the housing is therefore simplified to consider only the alumina to aluminium path. The thermal model is deconstructed into two nodes, being the alumina tube (node 1) and the aluminium housing (node 2).

At node 1, the power input onto the inner tube wall by the plasma (Q_{in}) is balanced by the increase in temperature (internal energy) of the alumina tube with density ρ_1, volume V_1 and specific heat c_{p1}, the heat transfer through convection to the neutral gas over area A_g with heat transfer coefficient h_g, and the loss through conduction to the aluminium housing over contact area A_c with thermal conductance coefficient h_c. No data is available for h_g, so an estimate of 100 W m^{-2} K^{-1} is used based on a low pressure flowing gas [158].

$$Q_{in} = m_1 c_{p1} \frac{dT_1}{dt} + h_g A_g (T_1 - T_g) + h_c A_c (T_1 - T_2) \tag{5.10}$$

The thermal conductance coefficient h_c depends on contact pressure and surface roughness of the alumina tube and aluminium housing, and as no data is available must be estimated. An estimate for h_c can be made from the heat flow (Q_{in}) from the inner alumina tube surface to the outer housing surface, as represented by Equation 5.11 [159], where L_1 and k_1 are the width and thermal conductivity of the alumina tube, respectively, and L_2 and k_2 are the width and thermal conductivity of the aluminium housing, respectively. The temperature difference between the inner alumina tube surface and outer housing surface (ΔT) is estimated as the difference between the gas temperature from steady state experimental results in Section 4.2 and ambient (300 K).

$$Q_{in} = \frac{\Delta T}{\frac{L_1}{k_1 A_c} + \frac{1}{h_c A_c} + \frac{L_2}{k_2 A_c}} \tag{5.11}$$

At node 2, power input (Q_{in}) is balanced by the increase in temperature of the aluminium housing with density ρ_2, volume V_2 and specific heat c_{p2} and the

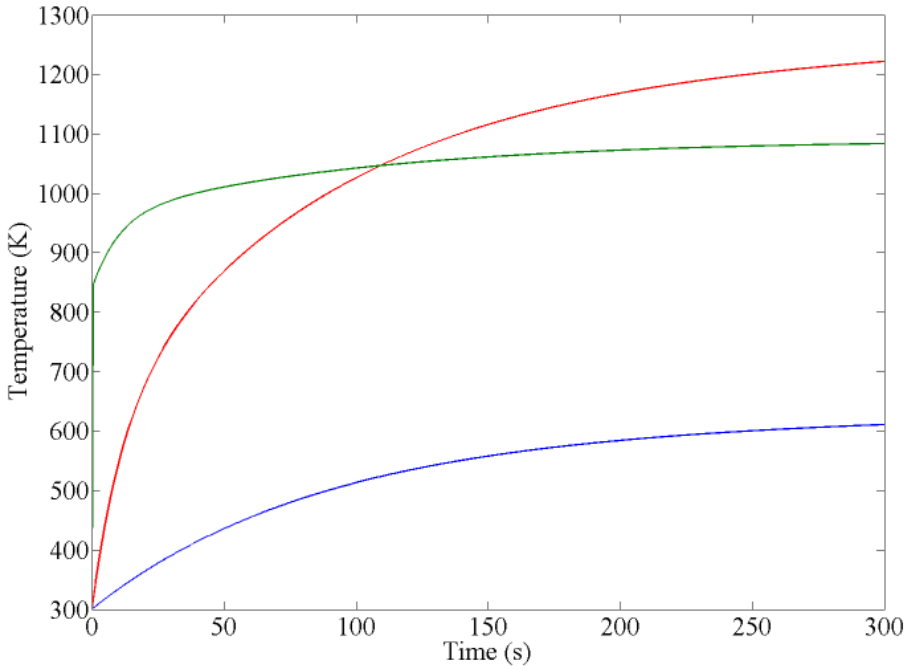

Figure 5.8: Lumped thermal model results for temporal heating in Pocket Rocket, showing temperature of the alumina tube (node 1 - solid red line), aluminium housing (node 2 - solid blue line), and the measured gas temperature by the wall (solid green line) for the first 300 s of operation.

heat loss through convection to the ambient air over area A_a with heat transfer coefficient h_a, as shown in Equation 5.12. No data is available for h_a, so an estimate of 300 W m^{-2} K^{-1} is used based on still atmospheric air [158].

$$Q_{in} = h_a A_a (T_2 - T_{inf}) + m_2 c_{p2} \frac{dT_2}{dt} \tag{5.12}$$

Results of the lumped thermal model are shown in Figure 5.8. The temperature of node 1 (alumina tube) is shown as a solid red line, the temperature at node 2 (aluminium housing) shown as a solid blue line, and for reference, the measured argon gas temperature by the wall from Section 5.3 is shown as a solid green line. At 300 s the wall temperature is higher than the gas temperature, which has previously been noted for a low temperature plasma discharge [82].

The results show that while the aluminium housing has a steady heating rate throughout, the alumina tube has a period of faster heating followed by a steady rate approximately equal to that of the aluminium housing. This is also obvious from Equations 5.10 and 5.12, where the alumina tube (node 1) has two convective

heating terms, while the aluminium housing (node 2) only has one, resulting in two heating rates for the alumina and one for the aluminium.

The heating rate or time constant of heating for a solid with volume (V) and heat transfer surface area (A) is given by Equation 5.13 [158], assuming the solid heats uniformly throughout the volume.

$$\tau = \frac{\rho c_p V}{hA} \tag{5.13}$$

Using the dimensions given in Figure 5.7 and thermal property values listed in Table 5.1, the heating time constant for the alumina is $\tau_{Al_2O_3} \approx 10$ s, and the heating time constant for the aluminium is $\tau_{Al} \approx 100$ s. These values match the time constants found during the spatiotemporal studies for the intermediate and slow heating ($\tau_2 = 10$ s and $\tau_3 = 100$ s), confirming that heating of the alumina tube and thruster housing accounts for both the intermediate and slow neutral gas heating measured in Pocket Rocket.

The lumped thermal model assumes that each node has a uniform temperature throughout the volume. In reality, thermal gradients develop across different housing components, with the magnitude of the gradient dependent on the thermal conductivity of the material. A low thermal conductivity material resists heat flow and a large thermal gradient will develop between the inner and outer surfaces, whereas a high thermal conductivity allows heat to flow readily and little or no thermal gradient will develop.

For a cylindrical system with length L and thermal conductivity k, the temperature difference (ΔT_{1-2}) between two points at radius r_1 and r_2 for a total heat flow of Q is given by Equation 5.14 [159].

$$\Delta T_{1-2} = \frac{Q}{2\pi k L} ln \frac{r_2}{r_1} \tag{5.14}$$

Using Equation 5.14, the thermal gradient through the Pocket Rocket housing after 10 s of operation is shown in Figure 5.9. The temperature gradient across the alumina tube (the region between the two dotted lines) is significantly sharper than the temperature gradient across the aluminium housing, due to the lower thermal conductivity of alumina compared to aluminium.

Combining the thermal gradient results from Figure 5.9 and spatiotemporal results from Section 5.3, it is concluded that in Pocket Rocket a power input from the

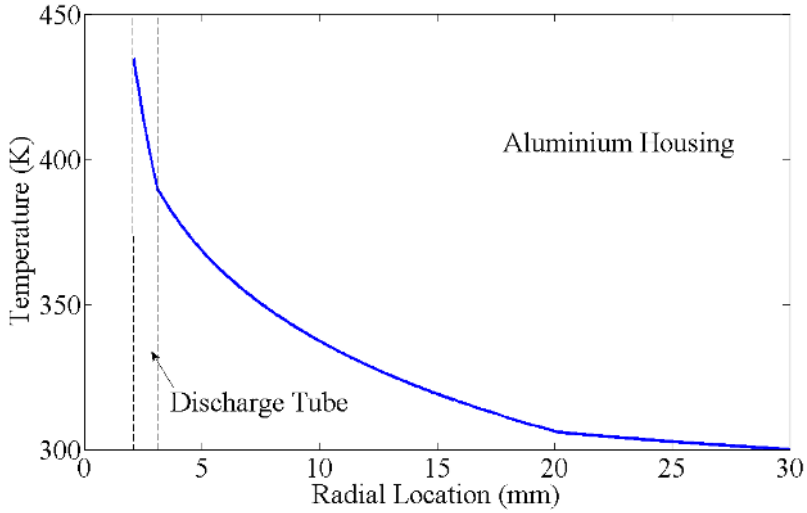

Figure 5.9: Radial temperature profile for Pocket Rocket housing after 10 s of operation

plasma to the alumina tube through ion bombardment and metastable quenching results in heating of the alumina tube (with $\tau \approx 10\ s$) and a thermal gradient developing across the alumina tube radius. Once the thermal gradient develops fully, the temperature of the inner surface of the alumina tube becomes limited by the outer surface of the alumina tube being in contact with the cold aluminium housing. As the bulk aluminium housing begins to slowly heat (with $\tau \approx 100\ s$), the outer alumina tube surface temperature increases, the thermal gradient across the alumina is no longer limiting and the inner discharge tube surface continues to increase in temperature (with $\tau \approx 100\ s$). This results in two distinct time scales for neutral gas heating of the propellant, as noted by the spatiotemporal results presented in Sections 5.2 and 5.3.

5.4.1 Housing Material Optimisation

To maximise the efficiency of surface heating on propellant heating in Pocket Rocket, the inner surface of the discharge tube should heat to the highest possible temperature as quickly as possible. Heating of the main thruster housing bulk should be limited and slow, as in the vacuum of space, radiation is the only mechanism available to remove heat and problems with thermal expansion and stress may arise if the housing heats significantly [9].

A high inner discharge tube surface temperature and slow bulk housing heating

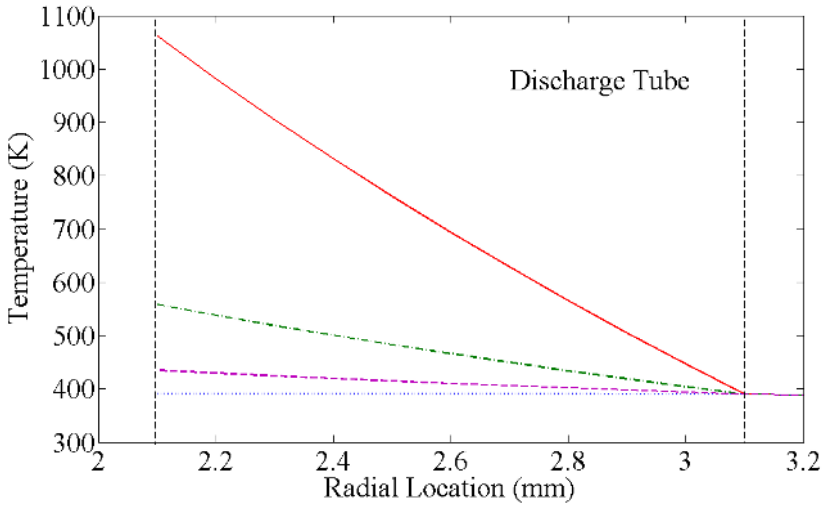

Figure 5.10: Temperatures across the discharge tube volume for Macor (solid red line), titanium dioxide (dot-dashed green line), alumina (dashed purple line) and diamond dotted blue line)

can be achieved using a discharge tube constructed of a material with low thermal conductivity, to limit the flow of heat away from the inner surface and into the main housing bulk. Expected thermal gradients across the discharge tube after 10 s of operation calculated using Equation 5.14 for alternate discharge tube materials with various thermal conductance values are shown in Figure 5.10. The materials shown are diamond (k=2000 W m^{-1} K^{-1} - dotted blue line), alumina (k=30 W m^{-1} K^{-1} - dashed purple line), titanium dioxide (k=8 W m^{-1} K^{-1} - dash-dotted green line) and Macor (k=2 W m^{-1} K^{-1} - solid red line).

Diamond, with a high thermal conductance, develops little or no thermal gradient resulting in a low inner surface temperature. The lower the thermal conductance, the larger the temperature gradient across the discharge tube and the hotter the inner discharge tube surface becomes, making materials with low thermal conductance better suited to electrothermal thruster applications. Additionally, based on Equation 5.13, the lower the density (ρ) and specific heat (c_p) of a material, the faster the final temperature will be reached. Therefore, materials with low thermal conductance, low density and low specific heat are best suited to electrothermal plasma micro-thrusters and Pocket Rocket.

5.5 Chapter Summary

Spatiotemporal profiles of neutral gas temperature in Pocket Rocket are made using rovibrational spectroscopy band fitting for both pure nitrogen and argon with 10% nitrogen discharges. The following observations are made:

- Fast (sub-millisecond) neutral gas heating in both nitrogen and argon with 10% nitrogen occurs evenly across the discharge volume resulting from collisional processes within the plasma.

- Slower neutral gas heating (tens to hundreds of seconds) in both nitrogen and argon with 10% nitrogen is enhanced in regions near the walls, caused by surface heating effects from heating of the thruster housing. Two distinct timescales for surface heating are observed, being from heating of the alumina discharge tube initially, followed by slower heating of the entire housing bulk.

- Discharge tube materials with low thermal conductance develop large temperature gradients between the inner and outer surfaces. A high inner surface temperature is optimal for propellant heating in an electrothermal device, hence materials with low thermal conductance should be used to maximise the surface heating gain.

Chapter 6

Pocket Rocket Computational Fluid Dynamics Simulation

Rovibrational spectroscopy experiments demonstrate that neutral gas heating occurs within Pocket Rocket for both argon and nitrogen (N_2) propellants, with heating coming from collisional volumetric processes and surface heating effects. Further investigations into the physics of operation for Pocket Rocket are performed with Computational Fluid Dynamics (CFD) simulations, using the Computational Fluid Dynamics Advanced Computational Environment (CFD-ACE+) software package outlined in Section 3.4. The use of simulations allows for a deeper understanding of the operation of Pocket Rocket without the problems associated with probe use within small devices, and eliminates the need for costly and time consuming adaptations to experimental setups.

Only argon simulations are considered for this work as the higher temperatures make it more favourable as a propellant than nitrogen, as discussed in Section 4.3. Initially, a 10 W, 1.5 Torr argon discharge simulation, representing the standard operating conditions of Pocket Rocket, is performed and compared to experimental results where possible for validation in Section 6.3. A comparison of experimental neutral gas temperature results from Chapters 4 and 5 and simulation results is included in Section 6.3.2. Once validated, the initial simulation forms the basis for further simulation work investigating the role of secondary electrons (see Section 6.3.1) and the pressure gradient throughout the system (see Section 6.4).

6.1 Parallel Plate CCP Test Case

Prior to commencing the complex 2D Pocket Rocket simulations, a simple parallel plate capacitively coupled plasma (CCP) is modelled using the same parameters as a previous study performed with the benchmarked PHOENIX Particle-In-Cell (PIC) code from Lafleur *et al.* [55] for preliminary comparison. An argon discharge at 100 mTorr created by symmetric electrodes placed 20 mm apart, as shown in Figure 6.1, is simulated using the CFD-ACE+ program. One electrode is grounded (black) and one carries a radio-frequency (RF) (13.56 MHz) voltage with maximum amplitude of 270 V (red). A single temperature Maxwellian electron distribution and ion induced secondary electron coefficient (γ) of 0.1 are used to match the PHOENIX PIC simulation.

Four volumetric gas phase reactions are used in the simulation, being elastic collisions between heavy particles and electrons, electron impact ionisation, electron impact excitation and stepwise ionisation, shown in Equations 6.1a to 6.1d, respectively. Rate coefficients and cross sectional data are taken from the JILA database, University of Colorado, as included in the CFD-ACE+ package.

$$Ar + e \rightarrow Ar + e \tag{6.1a}$$

$$Ar + e \rightarrow Ar^{+} + 2e \tag{6.1b}$$

$$Ar + e \rightarrow Ar^{*} + e \tag{6.1c}$$

$$Ar^{*} + e \rightarrow Ar^{+} + 2e \tag{6.1d}$$

The PHOENIX PIC simulation was performed in one spatial dimension (1D), whereas the CFD-ACE+ simulation is performed in two spatial dimensions (2D). To make the 2D CFD results comparable to the 1D PIC results, the electrodes and discharge fluid volume are given a finite width of 2 mm with both sides applied with a symmetric boundary condition, shown in Figure 6.1 as dashed grey lines. This eliminates edge effects and effectively makes the simulation an infinitely wide parallel plate CCP. Any vertical slice through the 2D geometry will be a quasi-1D solution and directly comparable to the 1D PIC results. The location of the quasi-1D slice used here is shown in Figure 6.1 as a dotted blue line.

While this simulation has a larger physical dimension and lower pressure than Pocket Rocket, applying the pressure-distance scaling law using a factor of 5 gives

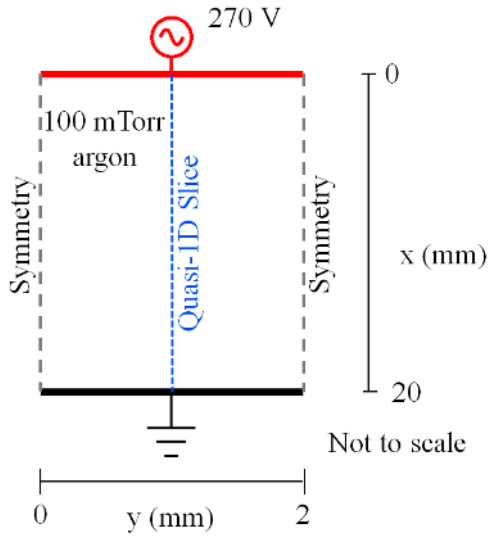

Figure 6.1: CFD simulation geometry for the simple parallel plate CCP test case (not to scale).

a 4 mm physical length scale (approximately the same as the Pocket Rocket tube diameter of 4.2 mm), and a pressure of 0.5 Torr. This is a factor of three lower than the 1.5 Torr pressure stated for Pocket Rocket in the upstream plenum, but as the pressure decreases throughout the Pocket Rocket tube to 0.75 Torr downstream, the pressure at the centre of the tube is likely to be around 1 Torr [160], closer to the scaled pressure value. Although this still does not exactly match the Pocket Rocket parameters, the difference is sufficiently small for the benchmarked PIC simulation to provide a suitable test case for the CFD-ACE+ solution.

Phase resolved RF electrode voltage (dashed line) and plasma potential (solid line) for the CFD simulation are shown in Figure 6.2(a). The plasma potential is taken at the midpoint between the two electrodes (x=10 mm) and oscillates between the maximum input voltage of 270 V and ∼5 V. The phase averaged plasma potential is represented by the straight dotted line in Figure 6.2(a) and is found to be 100 V, matching the time averaged plasma potential at the midpoint of the PIC simulation of just over 100 V [55].

Phase averaged electron (dashed line) and ion (solid line) densities are shown in Figure 6.2(b). Maximum electron and ion densities of 9.9×10^{15} m^{-3} occur at the midpoint of the discharge, tapering off by an order of magnitude at the electrodes, again matching the PIC simulation that gave a density in the order of 6×10^{15} m^{-3}

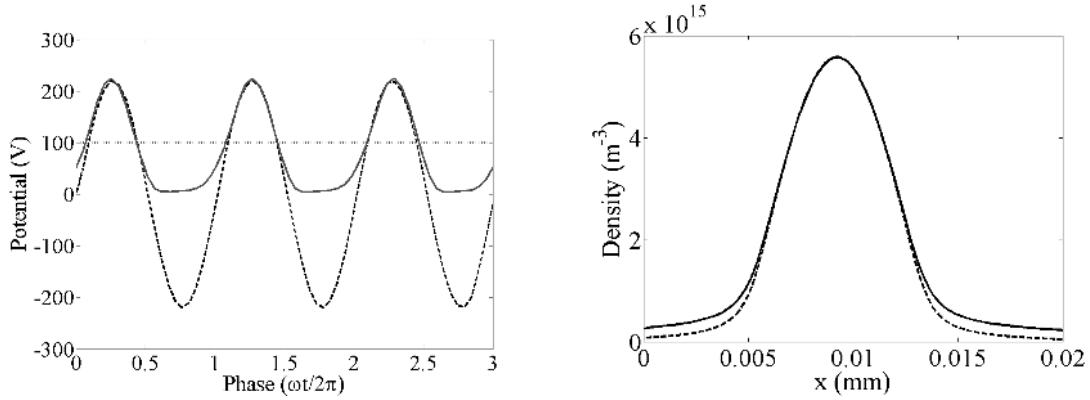

(a) (b)

Figure 6.2: CFD simulation results for a parallel plate CCP showing (a) phase resolved electrode voltage (dashed line) and plasma potential at x=10 mm (solid line) and phase averaged plasma potential at x=10 mm (dotted line), and (b) phase averaged electron (dashed line) and ion (solid line) densities.

[55]. The similarity between the CFD simulation results for plasma potential and density of a parallel plate CCP compared with the benchmarked PHOENIX PIC results gives preliminary confidence in the CFD-ACE+ CCP fluid model and its ability to correctly model the more complex 2D Pocket Rocket discharge.

6.2 Pocket Rocket Simulation Parameters

The parameters defined for the preliminary Pocket Rocket CFD simulation match the standard experimental operating conditions for the thruster (10 W, 1.5 Torr plenum pressure in argon) to allow for direct comparison to previous experiments and global model estimates [43,62–64] for validation purposes. Model geometry used including dimensions and inlet and outlet locations is as discussed in Section 3.4.2 and shown in Figure 3.6. Mesh density is 11075 total grid points, refined in regions expected to have sheaths, and is independent of results as discussed in Section 3.4.2

The inlet is defined with a fixed pressure of 200 Pa (1.5 Torr), with pure neutral argon inflow at 300 K. Argon density is calculated using the ideal gas law, viscosity is calculated using Sutherland's law, and relative permittivity is defined as a constant 1.00. The outlet for the simulation is defined with a fixed pressure of 100 Pa (0.75 Torr) to give a pressure gradient of two across the simulation model to

match experiments. The same four volumetric gas phase reactions used in the PIC comparison, given in Equation 6.1, are used here.

The alumina tube is modelled as a solid dielectric with a density of 3950 kg/m^3 and relative permittivity of 9.3. A 13.56 MHz sinusoidal voltage with maximum amplitude of 240 V is applied to the powered electrode, corresponding to the experimental post match voltage for a 10 W power input, measured with the Octiv probe placed at location A in Figure 2.2.

The initial conditions are pressures of 200 Pa in the plenum, 150 Pa in the discharge tube and 100 Pa in the expansion chamber, a temperature of 300 K everywhere, and an electric potential of 0 V everywhere. Within the plenum chamber and expansion tube the initial gas is pure neutral argon, but in the discharge tube an argon mixture containing 1×10^{-6} molar concentration of argon ions with a quasi-neutral amount of electrons at 2 eV is used to provide an arbitrary amount of charged particles to initiate breakdown.

The simulation is run for 20,000 timesteps using only eight iterations per timestep to accelerate the solution to a quasi-steady state near the final solution. Quasi-steady state is defined here as no change in parameters between successive RF cycles determined using monitor points placed within the discharge tube, plenum chamber and expansion tube. The number of iterations per timestep is then increased to sixty and the simulation continued for an additional 400 timesteps, the final 60 of which (corresponding to 3 complete RF cycles) being used for the final results presented in Section 6.3. This method minimises the simulation run time while maintaining the required accuracy of the final solution. Total computational run time for this preliminary Pocket Rocket simulation is approximately 8 hours which represents 150 ms of total transient simulation time.

6.3 Pocket Rocket Simulation Results

While the main focus of this study is plasma parameters such as electron density (n_e), electron temperature (T_e), plasma potential (V_p) and bias voltage (V_b), the CFD simulation also produces complete 2D results for background gas parameters including velocity (v), density (ρ) and pressure (p). Although most background gas

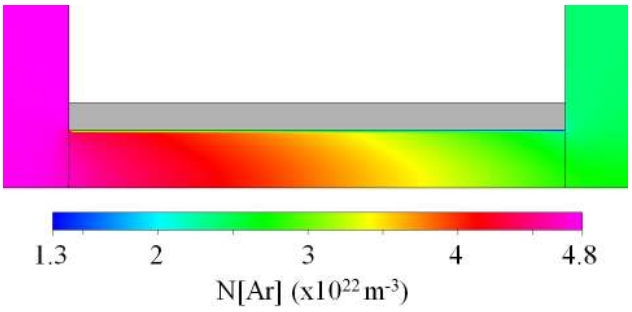

(a)

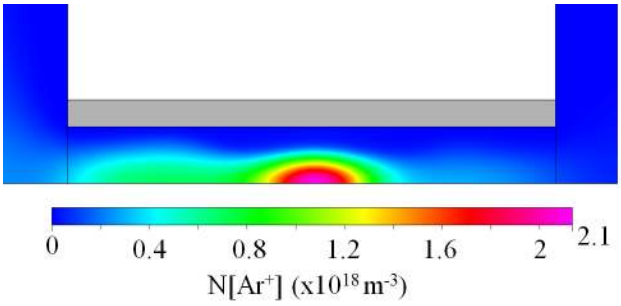

(b)

Figure 6.3: Two dimensional, time averaged CFD simulation results for (a) neutral gas density and (b) ion density within the discharge tube. The full 2D plot has been cropped to show only the region of interest (discharge tube) for clarity.

results are not included here as they are not of direct interest, Figure 6.3 shows 2D phase averaged plots of neutral gas density (n_g) and ion density (n_i), cropped from the complete 2D results to show only the discharge tube (region of interest) for clarity. The low ionisation degree in Pocket Rocket (0.44% in argon (Ar) at 10 W and 1.5 Torr [62]) means the plasma has little effect on the neutral gas density.

The peak in ion density in the centre of the tube, visible in Figure 6.3(b), has been previously noted in experiments by Charles *et al.* [43]. Charles *et al.* measured ion saturation current (I_{sat}) along the central axis of the Pocket Rocket discharge tube using the same Langmuir Probe as discussed in Section 3.1 and observed a peak in I_{sat} at the axial midpoint of the tube. From Equation 3.1, I_{sat} is directly proportional to n_i, therefore axial ion density peaks at the midpoint of the tube.

A qualitative comparison between ion density from the CFD simulation and ion saturation current previously measured by Charles *et al.* [43] is shown in Figure 6.4. Both the experimental ion saturation current and simulated ion density peak

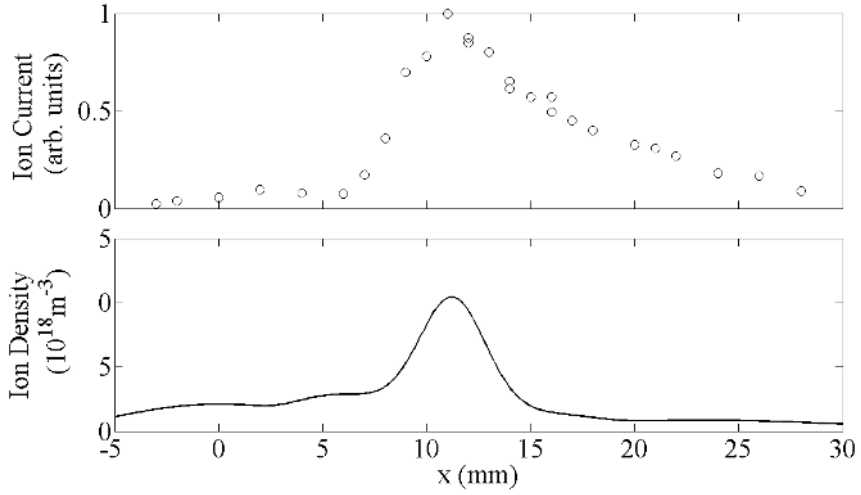

Figure 6.4: Ion saturation current along the central axis measured using a Langmuir Probe (top) [43] and simulated ion density along the central axis (bottom). The discharge tube lies between 0 mm and 20 mm, with the plenum chamber and expansion tube results cropped for clarity. The gas flow is from left to right (in the direction of increasing x).

at x = 11 mm, corresponding to the centre of the RF electrode. Downstream of the peak, the experimental results taper off slower than the simulation results due to flow constriction from the Langmuir probe increasing error bars in that region.

Similarly, a peak in electron density also occurs in the centre of the discharge tube, visible in Figure 6.5(a) showing complete 2D results for phase averaged n_e. The electron density peaks in the centre of the discharge tube, reaching 2.1×10^{18} m^{-3}, similar to previous experimental and global model estimates in the same axial location from Charles *et al.* [43] of 1.8×10^{18} m^{-3} and 2.4×10^{18} m^{-3}, respectively.

The neutral gas density gradient throughout the tube results in a higher absolute electron density in the upstream end of the discharge tube when compared with the downstream end giving an asymmetric electron density profile. However, the ionisation percentages in the upstream and downstream ends are both still approximately equal ($< 0.1\%$).

Phase averaged complete 2D results for T_e and V_p are shown in Figures 6.5(b) and 6.5(c), respectively. Electron temperature within the main bulk of the discharge tube lies between 2 and 2.4 eV, in agreement with global model estimates of 2 eV [43]. Downstream in the expansion tube the electron temperature decreases to <1 eV as the plasma expands into the larger volume and cools. Plasma potential peaks at

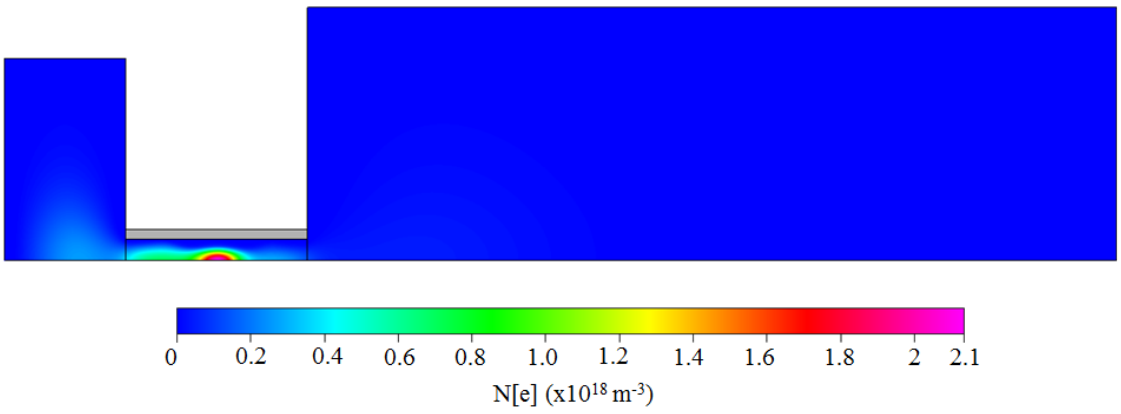

(a)

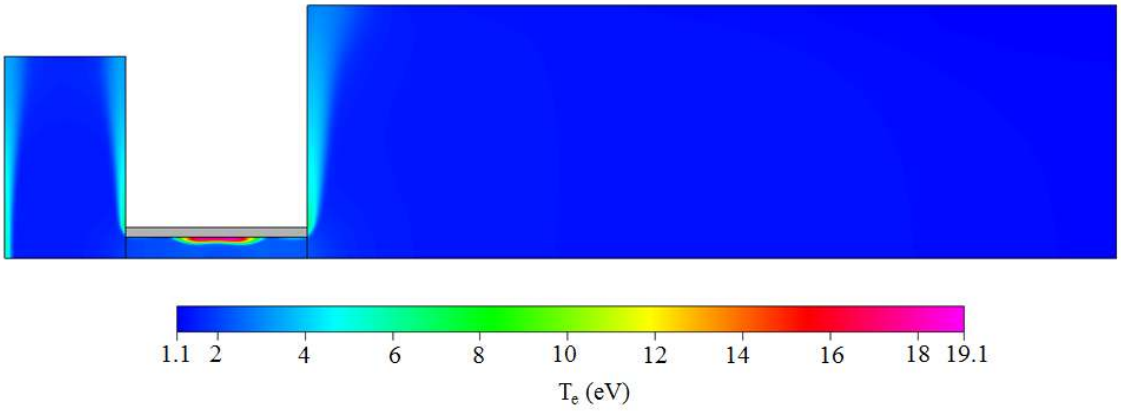

(b)

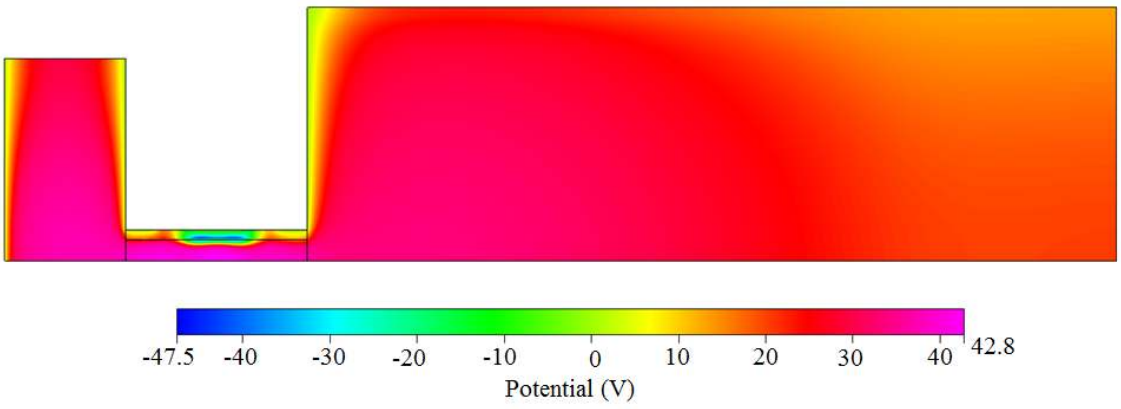

(c)

Figure 6.5: Complete phase averaged CFD simulation results for (a) electron density, (b) electron temperature and (c) plasma potential , showing the plenum chamber, discharge tube and expansion tube.

42 V in the centre of the discharge tube, corresponding to the peak in electron density, and decreases to 36 V at the discharge tube exit. Experiments by Dixon *et al.* [72] on a similar experimental setup, gave a plasma potential around 32 V near the tube exit for an approximately 1.5 Torr argon plasma, matching the simulation.

The asymmetry between the powered electrode area and the grounded area (including the grounded electrodes and plenum walls) in Pocket Rocket and a non-uniform axial density profile [43] results in a negative direct current (DC) self-bias developing on the alumina tube insert. This is clearly visible in Figure 6.5(c), as is the corresponding enhanced sheath in the nearby discharge region. Ion induced secondary electrons emitted from the walls in the vicinity of the DC self-bias are accelerated through the enhanced sheath to high velocities. Phase averaged T_e in this region has a maximum of 19.1 eV, as shown in Figure 6.5(b), substantially higher than the phase averaged 2.4 eV in the centre of the discharge tube. Similar acceleration of ion induced secondary electrons also occurs in the grounded electrode sheath regions as shown in Figures 6.5(b) and 6.5(c). However, without a negative DC bias to enhance the sheath voltage, the electrons attain significantly lower phase averaged temperatures of around 5 eV.

The self-bias on the alumina tube is also clearly evident in Figure 6.6, showing phase resolved potentials on the powered electrode and inner alumina tube surface, and the plasma potential on the central axis of the tube, all measured at the axial midpoint of the tube (x=11 mm). The potential on the inner alumina tube surface oscillates between 80 V and -200 V, with a DC bias of -43 V. Sheath capacitance model calculations previously performed estimate the inner surface of the alumina tube will develop a bias of -36 V [43], similar to the -43 V produced by the simulation. A slight phase offset between the inner alumina tube surface and the powered electrode potentials occurs, which is characteristic of the response voltage on the inner surface of a cylindrical dielectric tube with applied RF voltage on the outside [50]. Plasma potential follows the phase of the inner alumina surface potential and matches the maximum positive voltage, as expected for CCP in direct contact with a potential surface.

The effect of the hot ion induced secondary electrons accelerated through the enhanced sheath region caused by the self-bias is seen in Figure 6.7(a), showing

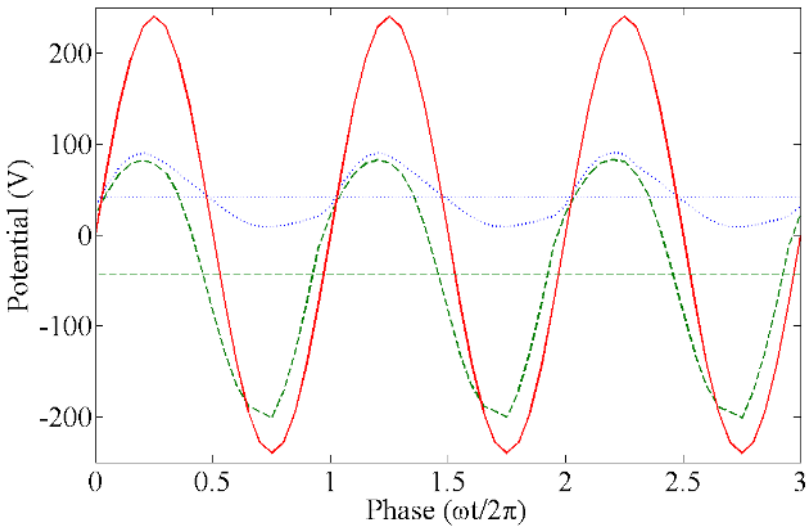

Figure 6.6: Phase resolved RF electrode voltage (solid red line), inner alumina tube surface potential (dashed green line) and plasma potential on the central axis of the tube (dotted blue line) at x=11 mm. Phase averaged plasma potential on the central axis (straight blue dotted line) and phase averaged inner alumina tube surface potential (DC self-bias) (straight dashed green line) are also shown.

phase resolved results for T_e, n_e and n_i at a point 0.1 mm from the inner surface of the alumina tube directly in line with the centre of the RF electrode (coordinates (11,2) in Figure 3.6). During the positive half of the RF period (phase<0.5), T_e sits around 1.6 eV, but during the negative half of the period (phase>0.5) T_e increases dramatically up to 42 eV as the enhanced negative sheath accelerates the ion induced secondary electrons into the main plasma bulk. Correspondingly, electron density decreases by two orders of magnitude during the negative half of the period as electrons are accelerated away from the sheath region by the large negative potential. As the electrons reach temperatures up to 42 eV, a significant number have energies well above the first ionisation potential of argon of 15.76 eV, and a corresponding peak in ion density occurs.

Figure 6.7(b) shows phase resolved T_e, n_e and n_i in the centre of the alumina tube (coordinates (11,0) in Figure 3.6). Only a slight increase in T_e (up to ~3 eV) occurs during the negative half of the RF cycle (phase>0.5), followed by a slight increase significantly less than an order of magnitude in ion and electron density. The lower T_e shows that the hot electrons from the sheath region have undergone

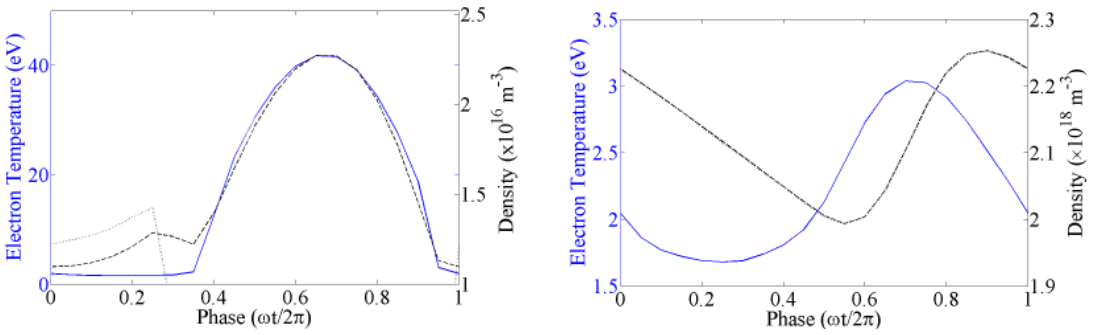

(a) (b)

Figure 6.7: Electron density (black dotted line), ion density (black dashed line) and electron temperature (blue solid line) with rf phase at a point in the discharge in line with the rf electrode (x=11 mm) and (a) 0.1 mm from the inner surface of the dielectric tube (y=2 mm) and (b) on the central axis of the thruster tube (y=0 mm).

significant inelastic collisions to either lose their additional energy or not diffuse into the central bulk plasma region. The bulk plasma remains quasi-neutral with n_e and n_i shadowing each other exactly as the effects of the negative bias are negated by this point.

6.3.1 Secondary Electrons

The DC self-bias from the asymmetry of the Pocket Rocket device appears to create a beam of ion induced secondary electrons with high energies that migrate into the main plasma bulk creating a peak in ion density in the centre of the discharge tube. This is supported by a recent 2D PIC simulation of a hollow cathode discharge that showed the discharge was driven by secondary electrons and sheath heating was not sufficient to sustain the discharge in the absence of secondary electrons [52]. To investigate the role of secondary electrons in the Pocket Rocket device, the above CFD simulation was repeated with ion induced secondary electron coefficients (γs) of 0.001, 0.01, 0.02, 0.05, and 0.2. The results for axial ion densities for each γ tested are shown in Figure 6.8, including the original results from Section 6.3 using γ=0.1.

For secondary electron emission coefficients of 0.02 or higher, the axial ion density profile containing a single peak at the midpoint of the tube is consistent with experimental results, but the peak density varies from 1.3×10^{18} m^{-3} to 4.9×10^{18} m^{-3}. For secondary electron coefficients of 0.01 or less, the ion density along the central

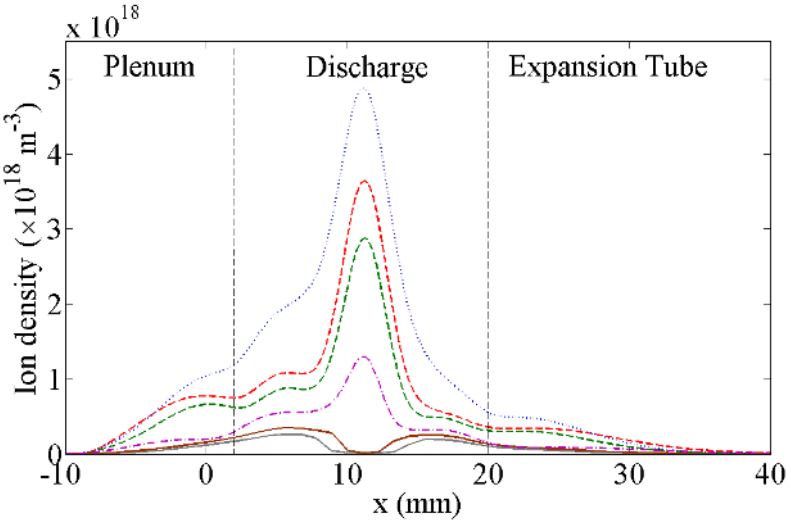

Figure 6.8: Ion density along the central axis of Pocket Rocket with ion induced secondary electron coefficients of 0.001 (solid grey line), 0.01 (solid brown line), 0.02 (dashed purple line), 0.05 (dashed green line), 0.1 (dashed red line) and 0.2 (dotted blue line).

axis develops a two peak distribution with a drop in density at the axial midpoint, diverging from experimental results. The decrease in density at the axial midpoint is caused by the sheath near the RF electrode extending across the entire radius, effectively blocking the plasma from the centre of the tube. With secondary electrons turned off (results not included in Figure 6.8), the solution also contains a two peak distribution but with unrealistic densities, suggesting the role of secondary electrons is crucial within the Pocket Rocket discharge as it was in the hollow cathode PIC simulations [52].

These results suggest that even with low secondary electron effects, plasma breakdown still occurs between the RF and grounded electrodes creating low plasma densities in those regions. Ions then bombard the surface of the dielectric, especially in the centre of the tube where the negative DC bias develops. If the ion induced secondary electron coefficient is too low, the density of ion induced secondary electrons accelerated by the sheath in the vicinity of the RF electrode is insufficient to further breakdown the plasma and create the peak in density in the centre of the tube. However, if the ion induced secondary electron coefficient is sufficient to create a beam of ion induced secondary electrons with sufficient density and energy to undergo ionisation collisions with neutral argon atoms, the central peak observed in experiments occurs.

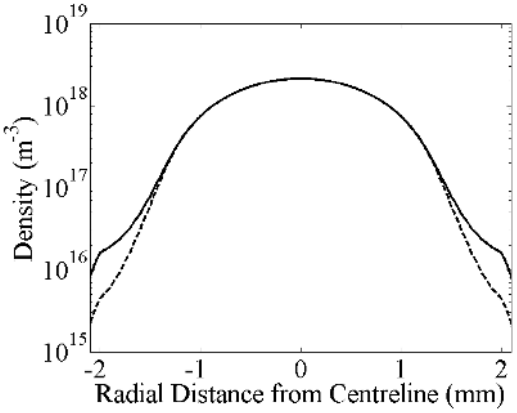

Figure 6.9: Phase-averaged electron (dashed line) and ion (solid line) density radially across the Pocket Rocket tube, in line with the centre of the rf electrode (x=11 mm).

The ion induced secondary electrons enter the main plasma bulk as a beam and as a result may not undergo significant collisions for the fluid approximation to hold. For the fluid approximation to be valid for electrons in the sheath region, the mean free path for electron-argon collisions must be significantly smaller than the sheath width. Mean free path (λ_{mfp}) for electron-argon collisions within the sheath region is calculated using a neutral density in the central region of the tube of 3.5×10^{22} m^{-3} (see Figure 6.3(a)) and cross sectional data from the JILA database, University of Colorado. Values for λ_{mfp} range from 0.57 mm for an electron energy of 2 eV ($\sigma = 3.52\times10^{-20}$ m^{-2}), to 85 μm for an electron energy of 14 eV ($\sigma_{max} = 23.8\times10^{-20}$ m^{-2}). Energetic tail electrons with an electron energy of 180 eV ($\sigma = 6.42 \times 10^{-20}$ m^{-2}) based on the maximum sheath potential that develops during the RF cycle (see Figure 6.6), have a mean free path of $\sim$0.91 mm.

Sheath width is estimated as $\sim$0.5 mm, based on the phase-averaged electron and ion density simulation results across the tube radius at x=11 mm (in line with the centre of the RF electrode), taken as the point where ion and electron density distinctly differ in Figure 6.9. This value is in good agreement with experimental estimates from digital photography [64] of 0.3 mm to 0.6 mm, but higher than estimates made with the Child sheath law of $\sim$0.2 mm [43] and is likely slightly overestimated.

Based on the above approximations, low energy and energetic tail electrons will not undergo a sufficient number of collisions within the sheath for the fluid approximation to be valid in that region and will instead enter the main plasma bulk as

an energetic beam. While the exact effect of this on the simulation results is indeterminate, the agreement between the simulation and experimental results suggest the effect is small and the simulation results are reasonable. However, as with all modelling applications, the simulation results are an approximation and should be taken as a guideline only.

6.3.2 Neutral Gas Temperature

The final results of the preliminary CFD Pocket Rocket simulation are for neutral gas temperature, to compare directly with experimental results in Chapters 4 and 5. Simulated neutral gas temperature includes heat transfer to the gas from plasma species, as outline in Section 3.4.1, Equations 3.38 to 3.42, including ion Ohmic heating and ion surface recombination heating.

Phase averaged simulation results for neutral gas temperature (T_g) along the central axis of the discharge tube are shown in Figure 6.10. The temperature peaks at just over 1000 K at the axial midpoint of the tube (in the same region as the peak plasma density) after entering from the plenum at approximately ambient temperatures (300 K). A decrease in temperature occurs downstream as the gas accelerates and expands into the expansion tube.

Although the simulation maximum temperature of ∼1000 K appears to match the steady state temperature of 1060 K for Ar with 1% N_2, measured using rovibrational spectroscopy in Chapter 4, this is likely a coincidence. After the 20400 timesteps performed here, the simulation time has reached only 150 ms. This places the solution roughly in the plateaued region in the temporal results between 100 ms and 1 s (see Figure 5.4), which means collisional effects inducing volumetric heating are in effect, but the simulation has not run for sufficient time for wall heating effects to be visible in the results. At 150 ms, the temperature of the discharge is expected to be lower than 1000 K by a few hundred degrees based on results of the temporal study performed in Section 5.2.

The steady state rovibrational spectroscopy measurement of 1060 K for Ar with 1% N_2 at 1.5 Torr and 10 W from Chapter 4 is a volume averaged result, and not the maximum value. The average temperature in the discharge tube from the simulation results is 580 K, shown in Figure 6.10 as a dashed grey line. This is 480 K cooler

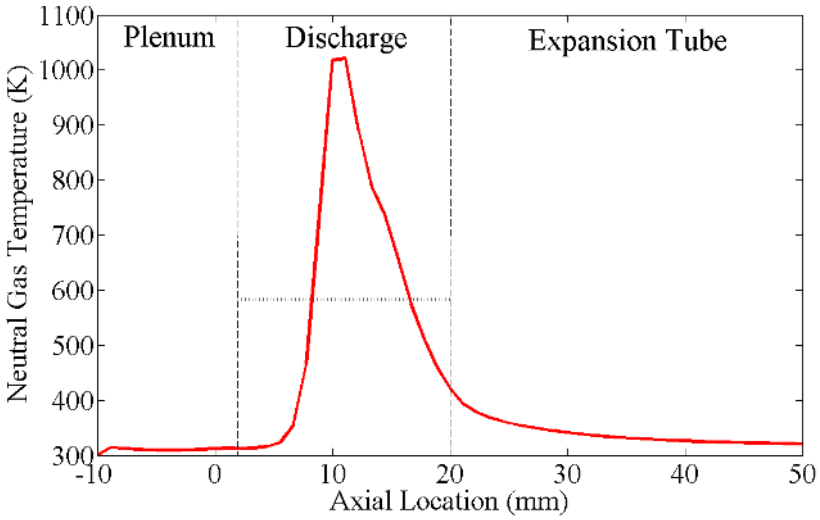

Figure 6.10: Phase averaged neutral gas temperature along the central axis of the Pocket Rocket discharge (solid line). The thin dashed line represents the axially averaged temperature within the discharge tube, between x=2 mm and x=20 mm.

than the measured 1060 K steady state temperature and seems reasonable compared to the ∼700 K measured in Chapter 5 at 150 ms before wall heating effects become noticeable.

Given that it takes eight hours to run 150 ms of Pocket Rocket simulation time, running 100 s of simulation time will take approximately 220 days (7 months). It is therefore not feasible to run the complete 2D CCP simulation for long enough time scales for wall heating effects to be directly included in the results. Instead, a modified steady state simulation encompassing only neutral gas flow and heat transfer is used as an indication of wall heating effects. The volumetric heat addition from collisional plasma effects is simulated by applying a constant power density to the discharge tube fluid volume. The surface heating effects are simulated by applying a constant power density to the inner surface of the alumina tube. Using this method, the transient plasma effects do not need to be included and an approximation of the final neutral gas temperature accounting for volume and surface heating effects, including the resulting effect on the gas flow and density profiles, can be approximated with simulation times of a few minutes, rather than several months.

Constant power density applied to the discharge tube fluid volume to simulate collisional heating effects is taken directly from the Pocket Rocket CFD simulation outlined in the preceding sections of this chapter. Phase averaged 2D power density

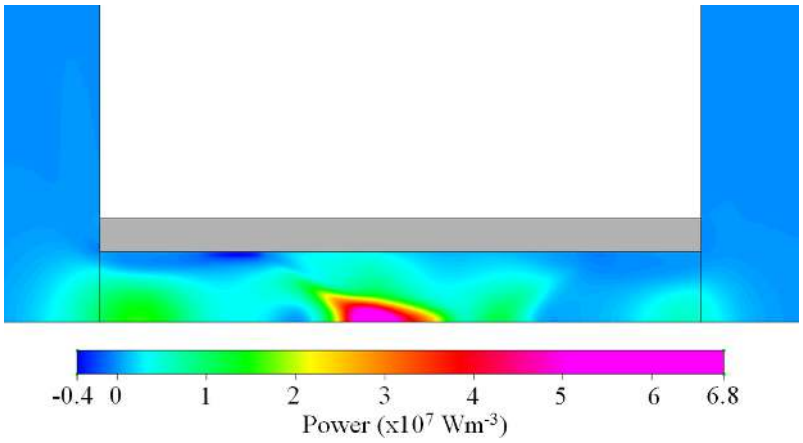

Figure 6.11: Power density results from the Pocket Rocket CFD simulation. Results have been cropped to show only the discharge tube region of interest for clarity.

results in the discharge tube are shown in Figure 6.11 giving a spatially averaged power density of 5.8×10^6 W m^{-3}. Assuming this power is deposited throughout the entire discharge tube volume, this corresponds to 1.6 W of total power.

Constant power density onto the wall is calculated using fluxes of metastable argon atoms and argon ions to the wall, and the amount of energy deposited per particle. Fluxes of excited atoms and ions are taken from the complete Pocket Rocket CFD simulation outlined in Section 6.3 and are shown in Figure 6.12. It is assumed that the main contribution from excited argon atoms comes from the $^3P_0$ and $^3P_2$ metastable states with excitation potentials of 11.72 eV and 11.54 eV, respectively. The energy deposited onto the inner alumina tube surface per atom is approximated as the average excitation energy for these two states, or 11.63 eV. Assuming the entire 11.63 eV is deposited onto the wall during the quenching collision gives 1.8×10^{-18} J per atom. Multiplying this by the flux density from Figure 6.12 and taking the average along the wall gives 310 W m^{-2} of power deposited from quenching of metastable states on the walls.

For ion bombardment of the walls, the kinetic energy of the ion is approximated using Equation 3.42, giving 7.0×10^{-18} J per ion. Assuming all of this energy is transferred to the wall during the collision, multiplying by the ion flux density from Figure 6.12 and taking the average along the wall gives 2050 W m^{-2} of power deposited from ion collisions with the walls.

A small contribution to wall heating may also come from radiated photons with

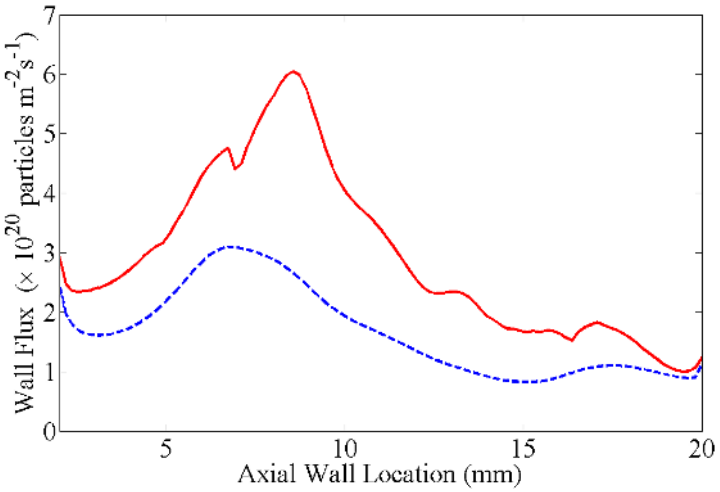

Figure 6.12: Fluxes of excited argon and argon ions to the inner surface of the alumina tube wall from the Pocket Rocket CFD simulation results

wavelengths of 104.5 nm and 106.7 nm from resonant emission processing occurring in the main bulk [161]. However, photons emitted in the main bulk must first travel through the discharge and may be absorbed before reaching the walls, depending on the optical thickness. Optical thickness (τ_a) for a photon with wavelength λ_a is approximated by Equation 6.2, where r_e is the classical electron radius, M is the mass of a discharge atom and d is the discharge diameter [81].

$$\tau_a = \frac{1}{2}\frac{\pi}{2}^{\frac{1}{2}} r_e \lambda_a n_g d \left(\frac{Mc^2}{kT_g}\right)^{\frac{1}{2}} \tag{6.2}$$

A 1000 K argon plasma with neutral density in the order of 3.5×10^{22} has an optical thickness of $\sim$ 250 at wavelengths around 104-107 nm. Therefore, few of the photons emitted in the bulk will reach the walls and any contribution to wall heating from radiated photons in the bulk is neglected.

The total average power density deposited onto the inner alumina tube surface from ion bombardment and metastable quenching is therefore approximated as 2360 W m^{-2}, corresponding to approximately 0.6 W total power. This is significantly less than the energy deposited in the plasma, but not all power deposited into the plasma is transferred to the walls as some is carried out in the plume. From calculations performed in Section 4.3, plume power is approximately 1 W, accounting for the difference between simulation volumetric power and calculated surface power.

The steady state heat transfer simulation requires that the complete thruster

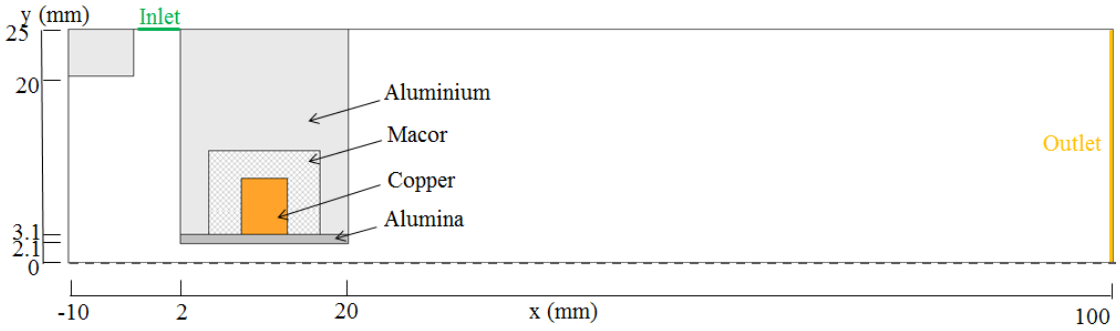

Figure 6.13: Model geometry including Pocket Rocket housing used for steady state heat transfer CFD simulations.

Table 6.1: Thermal properties of housing materials.

	Al_2O_3	Cu	Macor	Al
ρ [kg/m^{-3}]	3950	8960	2520	2700
c_p [J/kg-K]	880	386	790	900
k [W m$^{-1}K^{-1}$]	40	385	1.46	210

housing be modelled, as only the temperature of the outer housing surface is known to include as a simulation boundary condition. The housing was not required to be included for the initial simulation as wall heating effects, hence thruster housing heating, were not significant given the short simulation time, and neglecting the housing reduced computational expense. The modified geometry used is shown in Figure 6.13, with the alumina tube shown in dark grey, the copper electrode as orange, the Macor housing as hatched white and the aluminium housing as light grey. The fluid volumes are white and are the same three volumes as the previous simulation.

Thermal properties used for the different materials are given in Table 6.1. A constant volumetric heat addition of 5.8×10^6 W m^{-3} is applied to the discharge tube fluid volume (not including the plenum or expansion tube), and a constant surface heat addition of 2050 W m^{-2} is applied to the entire inner surface of the alumina tube. The inlet remains as pure argon at 1.5 Torr and 300 K, and the outlet at 0.75 Torr. As this is a steady state simulation involving just heat transfer and neutral gas flow effects, no plasma effects are considered and the entire fluid is assumed to be pure neutral argon.

Results for the temperature of the gas and housing are shown in Figure 6.14.

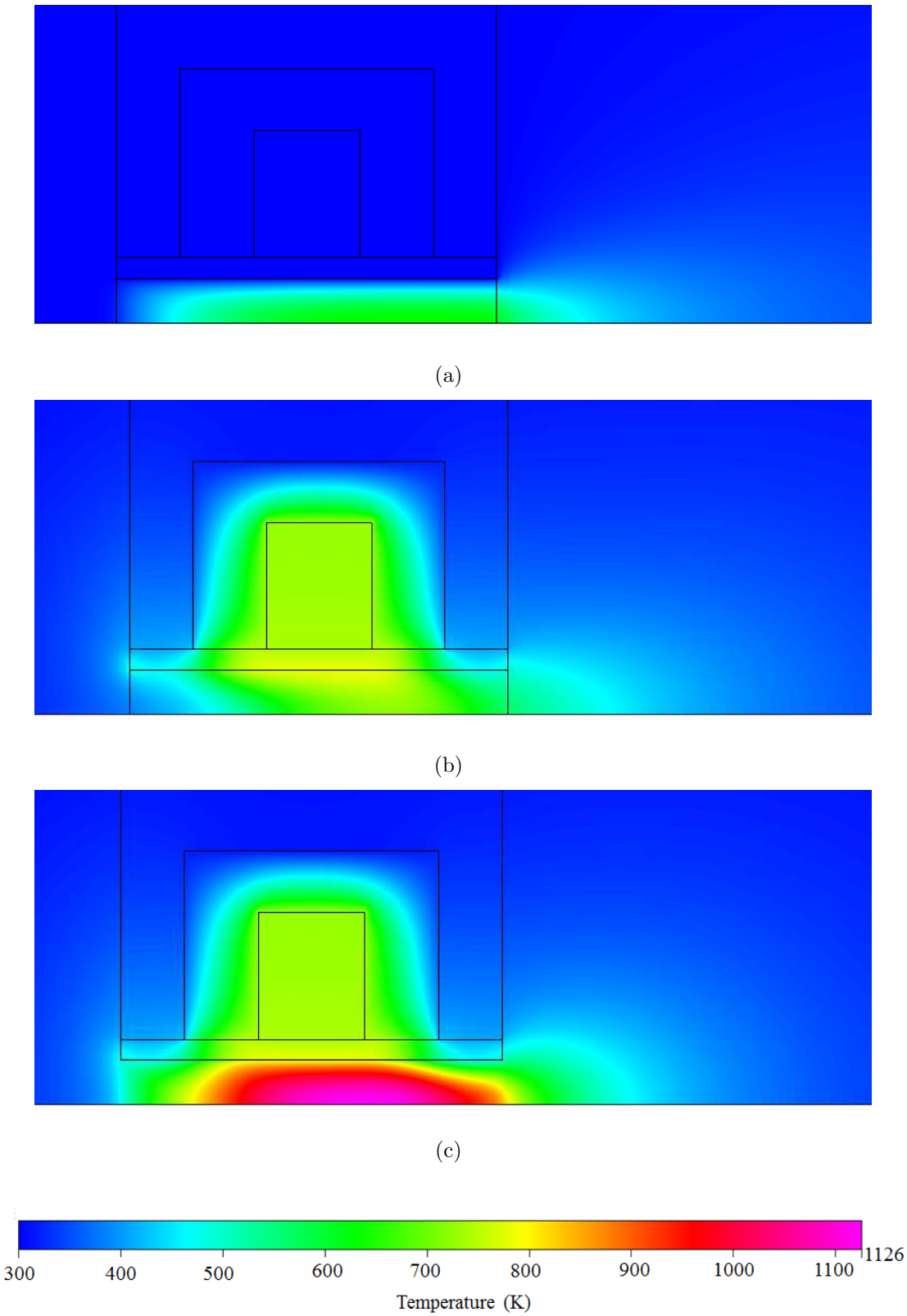

Figure 6.14: Temperature of the neutral gas and housing for (a) constant volumetric power input only, (b) constant surface power input only and (c) combined heating effects from constant volume and surface power inputs. The results are cropped to show only the region of interest for clarity.

The results have been cropped from the full simulation model to a region of interest encompassing the discharge tube, alumina tube, copper electrode and Macor housing for clearer presentation. Figure 6.14(a) shows heating effects from volumetric power input alone, Figure 6.14(b) shows heating effects from surface power input alone, and Figure 6.14(c) shows the combined heating effects from volume and surface power input.

The volumetric heating only case is used to compare with temperature results from the complete Pocket Rocket CFD simulation in Section 6.3, to ensure the steady state approximation method is valid. Average gas temperature from the complete Pocket Rocket CFD results is 580 K. The constant power density steady state approximation is around 600 K within the discharge tube, as shown in Figure 6.14(a), in agreement with the complete simulation result. The temperature increase from surface heating alone is shown in Figure 6.14(b). While there is no direct comparison with experiments or other simulations available, the temperature through the discharge tube from surface heating alone is around 650 K. This is the same temperature increase as from volume heating alone, something previously noted in the temporal experiment for nitrogen, but not for argon where volume heating was dominant, and it is possible the surface heating effects here are overestimated.

Combined heating from both volumetric and surface heating effects is shown in Figure 6.14(c), showing temperatures within the discharge tube around 1100 K, in excellent agreement with the measured steady state result of 1060 K. The spatial variation of temperature measured in Section 5.3, where neutral gas temperature (T_g) was higher in the vicinity of the walls, is not corroborated here as the volume and surface heating power inputs were defined as single constant average values throughout the entire discharge tube volume and over the entire alumina tube surface, removing any localised heating effects.

Neutral gas temperature results from the 10 W, 1.5 Torr argon Pocket Rocket CFD simulation agree with the experimental gas temperatures measured using rovibrational spectroscopy, and support the spatiotemporal rovibrational study results that heating occurs through both volumetric collisional processes and wall heating effects. The complete plasma simulation results also agree with previous experimental and global model estimates for plasma density, plasma potential, electron

temperature and DC self-bias, supporting the use of CFD simulations to further analyse the Pocket Rocket thruster and the underlying discharge physics. The use of CFD simulations for further investigations eliminates the need for costly and time consuming changes to the physical experimental setup, and is therefore a very powerful diagnostic tool.

6.4 Pressure Gradient Simulations

While many choices could be made for further investigations using CFD, such as electrode configuration or discharge tube geometry, here is it chosen to investigate the pressure gradient. During experiments the pressure gradient between the upstream plenum and downstream vacuum chamber is between two and four, with background pressures up to 0.75 Torr for the standard operating plenum pressure in argon of 1.5 Torr. As discussed in Section 2.3.1, the flow becomes choked at higher pressure gradients forming a shock at the exit of the discharge tube. The shock formed by the choked flow is expected to make the behaviour of the plasma inside the discharge tube independent of the downstream pressure [67], thereby removing the requirement to upgrade the experimental setup to produce higher pressure gradients.

However, as an electrothermal thruster operating in space, Pocket Rocket will be subjected to a significantly higher pressure gradient, with background pressures of around 10^{-10} to 10^{-8} Torr at altitudes between 100 and 1000 km, the approximate altitudes of low earth orbit (LEO). Background pressures around 10^{-10} to 10^{-8} Torr give a pressure gradient between 10^{8} to 10^{10}, many orders of magnitude higher than the pressure gradient in the standard experimental setup, and further investigations into the effect of a higher pressure gradient should be performed to make the preliminary investigations into the operation of Pocket Rocket complete.

6.4.1 Simulation Parameters

The flow through Pocket Rocket becomes choked at pressure gradients higher than approximately 2.1, after which a shock forms at the tube exit and the downstream pressure becomes independent of the pressure within the discharge tube. It is there-

fore expected that the discharge parameters inside the tube will not significantly change with increasing pressure gradient, hence a higher pressure gradient will not affect thruster performance.

The initial simulation of Pocket Rocket in Chapter 6 was performed to emulate the standard experimental setup, including the 50 mm diameter, 700 mm long downstream glass expansion tube connecting the Pocket Rocket device to the vacuum chamber. The inlet pressure was defined at 1.5 Torr and the outlet pressure defined at 0.75 to give a pressure gradient between the plenum chamber and outlet of the glass expansion tube ($\frac{p_{pl}}{p_{ex}}$) of two. To investigate the effect of pressure gradient on plasma parameters in the discharge tube and plume regions, the simulation is repeated with the outlet pressures set to 0.375 Torr, 0.075 Torr, 0.0025 Torr and 0.00025 Torr, giving values for $\frac{p_{pl}}{p_{ex}}$ of 4, 20, 200 and 2000 to compare with the initial simulation with $\frac{p_{pl}}{p_{ex}}$ of 2. A stagnant flow case, with an outlet pressure set to 1.5 Torr ($\frac{p_{pl}}{p_{ex}}$=1) is also included for comparison. The remaining simulation parameters are identical to those presented in Chapter 6.

6.4.2 Simulation Results

Figure 6.15 shows the simulation results for neutral gas number density and plasma (ion) density along the thruster central axis with changing pressure gradient across the system. The stagnant case ($\frac{p_{pl}}{p_{ex}}$=1) is shown as a blue line, $\frac{p_{pl}}{p_{ex}}$=2 is shown in green, $\frac{p_{pl}}{p_{ex}}$=4 is shown in red, $\frac{p_{pl}}{p_{ex}}$=20 is shown as an aqua line, $\frac{p_{pl}}{p_{ex}}$=200 is shown as a magenta line and $\frac{p_{pl}}{p_{ex}}$=2000 is shown as a brown line.

For a pressure gradient of 4 or above, the neutral density at the tube exit remains constant regardless of the downstream neutral density, demonstrating the flow has become choked as predicted by the choked flow criterion (Equation 2.2). Plasma density demonstrates no significant trend with pressure gradient in either the discharge tube or plume region (expansion tube), and retains a peak density of $\sim 2 \times 10^{18}$ m^{-3} at the axial midpoint of the discharge tube for all conditions tested.

Phase averaged electron temperature and potential also demonstrate no significant trend with increasing pressure gradient. Figure 6.16 shows phase averaged electron temperature in the centre of the discharge tube (blue circles), phase averaged electron temperature in the sheath region by the powered electrode (blue

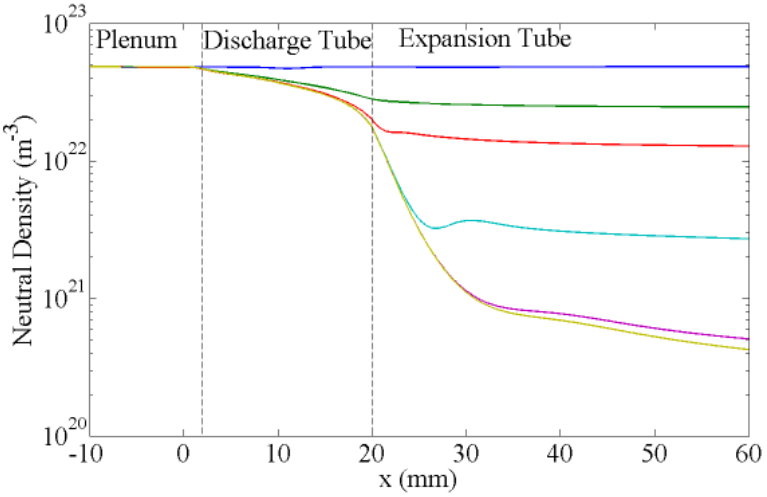

(a)

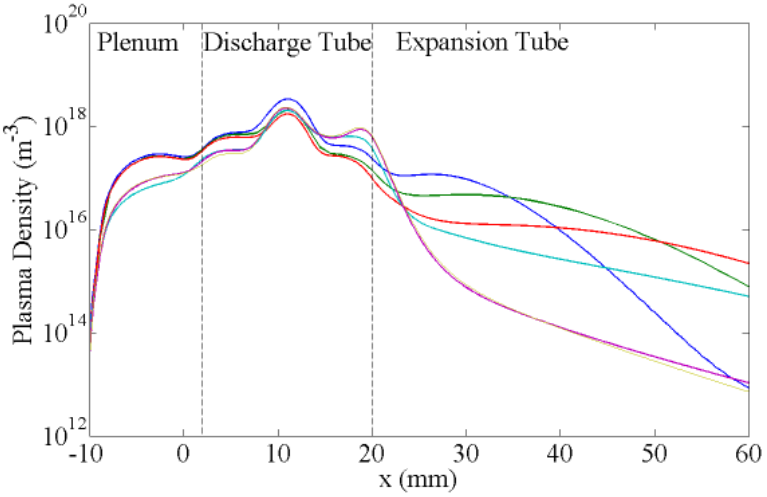

(b)

Figure 6.15: Axial profiles for (a) neutral gas density and (b) plasma (electron) density for pressure gradients of 1 (blue line), 2 (green line), 4 (red line), 20 (aqua line), 200 (purple line) and 2000 (brown line).

triangles), phase averaged plasma potential in the centre of the discharge tube (red squares) and DC self-bias potential on the alumina tube (red diamonds).

The electron temperature in the centre of the tube remains around 2.5 eV regardless of pressure gradient. Plasma potential in the centre of the discharge tube changes slightly, varying between 30 V and 43 V for all simulations run, but has no apparent trend with changing pressure gradient.

The phase averaged electron temperature in the powered sheath region is slightly lower in the stagnant case (T_e=15.6 eV) where the background gas density is much

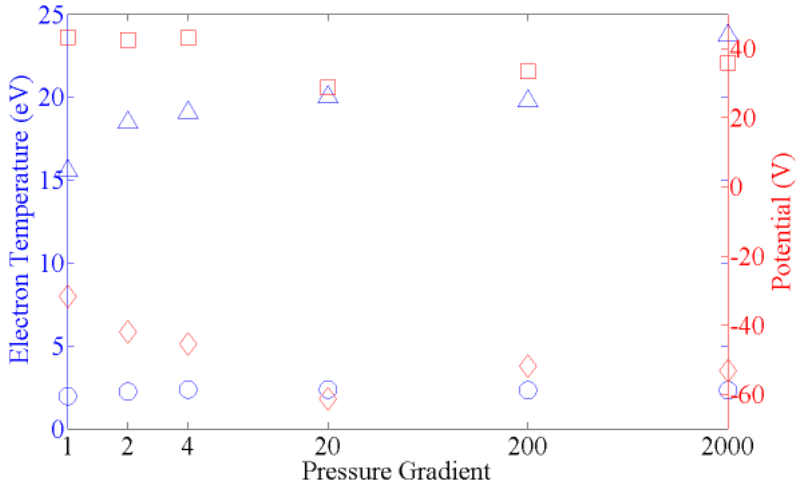

Figure 6.16: CFD results for phase averaged plasma potential in the centre of the discharge tube (red squares), DC self-bias on the alumina tube (red diamonds), electron temperature in centre of discharge tube (blue circles), and electron temperature in the sheath by the powered electrode (blue triangles) with varying pressure gradients.

higher than the other pressure gradient simulations resulting in more electron collisions, but otherwise has no significant trend apparent and remains between 18 eV and 23 eV. Similarly, the stagnant case develops a DC self-bias of -32 V, which is lower than the remaining simulations with DC self-bias results between -42 V and -60 V, again with no apparent trend with pressure gradient.

Based on the results for electron temperature in the sheath region and DC self-bias, the beam of secondary electrons entering the main plasma bulk and driving the discharge, as discussed in Section 6.3.1, is likely unaffected by changing pressure gradient. This is supported by main bulk plasma parameters of electron temperature and plasma potential also demonstrating no significant change with pressure gradient (Figure 6.16), and corroborates the results from Figure 6.15, where the bulk plasma density is unaffected by pressure gradient.

Testing pressure gradients higher than 2000 with CFD simulations is not feasible as the low downstream pressures create rarefied flow conditions, beyond the limit of the fluid approximation. Simulations of higher pressure gradients would need to be performed with a hybrid fluid-particle code, which is currently beyond the capabilities of the CFD-ACE+ software. However, a neutral gas temperature of 1260 K has recently been measured in a 1.5 mm diameter Pocket Rocket thruster prototype

known as Mini Pocket Rocket operating at 1.6. Torr and 30 W with an experimental pressure gradient of 5000 [162], confirming pressure gradient has no effect on neutral gas heating for higher pressure gradients. Therefore, the operating pressure gradient across Pocket Rocket should have little effect on thruster performance.

6.5 Chapter Summary

A preliminary Computational Fluid Dynamics simulation of the Pocket Rocket device performed and validated against experimental results where possible has demonstrated the following:

- The asymmetry between the powered and grounded electrode area results in a negative DC self-bias developing on the surface of the alumina tube in the vicinity of the powered sheath region. The negative DC bias enhances sheath potentials by the powered electrode, accelerating ion induced secondary electrons in that region to high velocities and energies. The ion induced secondary electrons enter the main plasma bulk as a beam, resulting in a peak in plasma density in the centre of the tube (both axially and radially).

- The ion induced secondary electron emission coefficient affects the peak plasma density of the simulation, demonstrating ion induced secondary (gamma) electrons drive the discharge. For low ion induced secondary electron emission coefficients, the peak in plasma density in the centre of the tube disappears, deviating from experimental results and confirming Pocket Rocket operates in the gamma mode.

- Volumetric and surface heating contributions to neutral gas temperature are approximately equal, and are in agreement with direct measured temperatures in Chapter 5.

- Increasing the pressure gradient across the Pocket Rocket system has little effect on either bulk plasma parameters or the beam of secondary electrons driving the discharge. Hence, operating pressure gradient across Pocket Rocket has little effect on thruster performance, confirming proof of concept of Pocket Rocket as an electrothermal plasma micro-thruster.

Chapter 7

Conclusions

An electrothermal plasma micro-thruster known as 'Pocket Rocket', under development at the Australian National University, has been studied using rovibrational spectroscopy and Computational Fluid Dynamics (CFD). The Pocket Rocket device consists of a small alumina tube surrounded at the midpoint by a radio-frequency (RF) powered electrode. Neutral gas (here argon (Ar) and nitrogen (N_2)) at pressures of a few Torr flows from an upstream plenum chamber with grounded walls through the tube before expanding downstream into an insulated expansion tube connected to a vacuum chamber. Power input of a few tens of Watts creates a weakly ionised plasma discharge within the alumina tube.

Ion-neutral collisions within the plasma bulk results in neutral gas heating throughout the discharge volume. Ion neutralisation and metastable atom quenching on the alumina tube walls results in surface heating, increasing the temperature of the neutral gas flowing through the tube. The heated neutral gas particles have higher velocities than cold gas particles, and accelerate in the direction of plasma flow increasing the momentum of the neutral jet expelled from the alumina tube. The increased momentum of the expelled jet makes the Pocket Rocket device a viable electrothermal plasma micro-thruster.

The neutral gas temperatures of both argon and N_2 discharges were measured using the rovibrational spectroscopy technique outlined in Section 3.3. As this technique is only suitable for diatomic molecules, trace amounts of N_2 were added to the argon discharge to produce the required rovibrational bands. Resonant energy transfer between argon metastable atoms and N_2 molecules may affect temperature

measurements made using the rovibrational spectroscopy band fitting technique for Ar-N_2 mixtures. The effect of the resonant energy transfer was tested by measuring the gas temperature of various percentage mixtures of N_2 in argon and comparing the results to an analytical model. Results showed (see Section 4.1) that mixtures involving between 5% and 50% N_2 may produce inaccurate gas temperatures, but low percentages of N_2 (<5%) do not significantly affect measured argon gas temperatures.

Neutral gas temperatures for standard operating conditions of 1.5 Torr plenum pressure and 10 W pre-match input power were measured as 1060 K for an argon with 1% N_2 discharge and 430 K for a pure N_2 discharge (see Section 4.2). Argon gas temperatures are higher than N_2 gas temperatures as an argon atom has only three translational degrees of freedom for kinetic energy distribution, whereas N_2 has two rotational and one vibrational mode in addition to the three translational modes for kinetic energy to be distributed between. Measured gas temperatures in N_2 increase with power and decrease slightly with pressure, as both increasing the power and decreasing the pressure results in higher power deposition per molecule. Measured gas temperatures in argon have no discernible trend with either power or pressure, with power deposition likely saturated at powers below those used here.

Spatiotemporal studies of neutral gas temperature for both N_2 and argon with 10% N_2, described and discussed in Chapter 5, demonstrate that fast (sub-millisecond) neutral gas heating occurs evenly across the discharge volume, resulting from collisional processes within the plasma. Slower neutral gas heating (tens to hundreds of seconds) from ion bombardment of the thruster walls resulting in surface heating is enhanced in regions near the walls. Two distinct timescales for surface heating in Pocket Rocket are observed, being from heating of the alumina discharge tube initially, followed by slower heating of the entire housing bulk. The thermal design of Pocket Rocket can therefore be optimised for future design iterations by using discharge tube materials with high thermal conductance values. This will create large temperature gradients between the inner and outer surfaces of the discharge tube, optimising the amount of heat retained in the tube for gas heating while minimising the heat transferred into the thruster housing and associated satellite components. Further investigations into thruster housing materials and thermal de-

sign optimisation should be performed as part of the development of a flight ready prototype.

Additional investigations into the operation of the Pocket Rocket device were performed using Computational Fluid Dynamics (CFD) simulations, instead of making expensive and time consuming changes to experimental components. Results of a preliminary CFD simulation representing standard experimental operating conditions were validated against experimental results where possible, to benchmark the use of CFD simulations using the Computational Fluid Dynamics Advanced Computational Environment (CFD-ACE+) package on Pocket Rocket, as discussed in Chapter 6. Simulation results agreed with experimental values for plasma density, plasma potential, direct current (DC) self-bias and neutral gas temperature, benchmarking the preliminary simulation and allowing for further simulations using CFD to be performed with confidence.

The Pocket Rocket device is highly asymmetric resulting in a DC self-bias developing on the surface of the ceramic tube in the vicinity of the powered electrode, as demonstrated by CFD simulations in Chapter 6. Ions bombarding the surface of the tube in this region release secondary or gamma electrons, that are accelerated as a beam into the main discharge bulk by the enhanced sheath from the self-bias. This results in a peak in plasma density in the centre of the tube, both radially and axially. The role of the ion-induced secondary electrons on the peak in plasma density was investigated using additional CFD simulations, outlined in Section 6.3.1. It was shown that with a low ion-induced secondary electron coefficient, the discharge plasma density profile deviates from the single peak at the centre of the tube observed during experiments, demonstrating Pocket Rocket operates in the gamma capacitively coupled plasma (CCP) mode.

For all experiments and preliminary simulations performed in this work, the pressure gradient across the system was between two and four. At pressure gradients higher than approximately two, the flow becomes choked, a shock forms at the discharge tube exit, and the downstream pressure becomes independent of the pressure upstream of the shock, as discussed in Section 2.3.1. Therefore, the flow and plasma parameters within the discharge tube are expected to remain relatively constant at higher pressure gradients, and the need for a more complex and expensive pump-

ing system for experiments is not required. However, as an electrothermal plasma micro-thruster operating in space, the pressure gradient across the system will be significantly higher than two, and for completeness the effect of a higher pressure gradient was investigated using additional CFD simulations.

Results of the CFD simulations performed with pressure gradients between the upstream plenum and downstream expansion tube of greater than two, as discussed in Section 6.4, demonstrated there was little effect on either the bulk plasma parameters or the beam of ion-induced secondary electrons driving the discharge. Therefore, thruster operation is not expected to be significantly affected at higher pressure gradients, and although experimental testing was performed with low pressure gradients the results should be indicative of true thruster performance.

Thruster performance estimates (see Section 4.3) made using the measured gas temperatures and the Rocket Equation (Equation 1.1) show argon is a preferable propellant over N_2, producing similar thrust but with higher specific impulse and efficiency. Pocket Rocket operating on argon at 10 W and 1.5 Torr produces an estimated thrust of 2.4 mN with a specific impulse of 76 s. This is approximately double the performance of a cold gas thruster with similar geometry and similar performance to other microwave and radio-frequency electrothermal thrusters discussed in Chapter 1. However, the current Pocket Rocket design is completely unoptimised, and it is expected that performance can be increased significantly by optimising the design to be used for a flight ready prototype.

In preparation of a flight ready prototype, the neutral gas temperatures attained for alternate propellants should be analysed, to ensure the most suitable propellant is utilised in the final design for optimal performance. Construction of the thruster housing and choice of discharge tube material should be thermally optimised, as mentioned above. In addition, further improvements to the performance of the Pocket Rocket device can be achieved by optimising the electrode configuration and discharge tube geometry. It is suggested CFD simulations are used for preliminary investigations into geometric optimisation, to reduce the time and expense required to create numerous additional experimental devices. Finally, although a nozzle was not included here where the investigation focussed on the underlying physics of the thruster and not its direct performance, any flight ready prototype development

should include investigations into an optimal nozzle design.

Outcomes of this work have demonstrated proof of concept of the Pocket Rocket electrothermal plasma micro-thruster under development at the Australian National University, and have identified the underlying physical mechanisms behind the associated plasma discharge and neutral gas heating. Expansion of this work through the suggestions included above will lead to the development of an optimised flight ready Pocket Rocket prototype. Additionally, the outcomes of this work in regards to the plasma discharge and neutral gas heating findings can be applied to other electrothermal plasma devices, to improve performance and advance the current state of technology.

Bibliography

[1] R. H. Frisbee, "Advanced space propulsion for the 21st century," *Journal of Propulsion and Power*, vol. 19, no. 6, pp. 1129–1154, 2003.

[2] J. Mueller, *Micropropulsion for Small Spacecraft*, ch. Thruster Options for Microspacecraft, pp. 45–137. AIAA, Reston, VA, 2000.

[3] A. Mehrparvar, *CubeSat Design Specification Revision 13*. The CubeSat Program, California Polytechnic State University, 2014.

[4] J. Puig-Suari, C. Turner, and W. Ahlgren, "Development of the standard cubesat deployer and a cubesat class picosatellite," in *Proceedings of the Aerospace Conference*, vol. 1, pp. 347–353, 2001.

[5] M. Swartwout, "The first one hundred cubesats: A statistical look," *Journal of Small Satellites*, vol. 2, no. 2, pp. 213–233, 2013.

[6] D. M. Goebel and I. Katz, *Fundamentals of Electric Propulsion: Ion and Hall Thrusters*. John Wiley and Sons, 2008.

[7] C. Charles, "Plasmas for spacecraft propulsion," *J. Phys. D: Appl. Phys*, vol. 42, p. 163001, 2009.

[8] T. Edelbaum, "Optimum low-thrust rendezvous and station keeping," *Journal of Spacecraft and Rockets*, vol. 2, no. 7, pp. 1196–1201, 1964.

[9] R. W. Conversano, "Mission capability assessment of cubesats using a miniature ion thruster," *Journal of Spacecraft and Rockets*, vol. 50, pp. 1035–1046, 2013.

[10] C. Lugini and M. Romano, "A ballistic-pendulum test stand to characterize small cold-gas thruster nozzles," *Acta Astronautica*, vol. 64, no. 56, pp. 615 – 625, 2009.

[11] J. Kohler, J. Bejhed, H. Kratz, F. Bruhn, U. Lindberg, K. Hjort, and L. Stenmark, "A hybrid cold gas microthruster system for spacecraft," *Sensors and Actuators A: Physical*, vol. 98, pp. 587 – 598, 2002.

[12] T. Yuan, A. Li, B. Huang, Y.-T. Chen, and C. Chen, "Design, fabrication, and test of a microelectromechanical-system-based millinewton-level hydrazine thruster," *Journal of Propulsion and Power*, vol. 27, no. 2, pp. 509–512, 2011.

[13] C.-K. Kuan, G.-B. Chen, and Y.-C. Chao, "Development and ground tests of a 100-millinewton hydrogen peroxide monopropellant microthruster," *Journal of Propulsion and Power*, vol. 23, no. 6, pp. 1313–1320, 2007.

[14] D. L. Hitt, C. M. Zakrzwski, and M. A. Thomas, "Mems-based satellite micropropulsion via catalyzed hydrogen peroxide decomposition," *Smart Materials and Structures*, vol. 10, no. 6, p. 1163, 2001.

[15] K. Sathiyanathan, R. Lee, H. Chesser, C. Dubois, R. Stowe, R. Farinaccio, and S. Ringuette, "Solid propellant microthruster design for nanosatellite applications," *Journal of Propulsion and Power*, vol. 27, no. 6, pp. 1288–1294, 2011.

[16] C. D. Rayburn, M. E. Campbell, and A. T. Mattick, "Pulsed plasma thruster system for microsatellites," *Journal of Spacecraft and Rockets*, vol. 42, no. 1, pp. 161–170, 2005.

[17] M. Tajmar, A. Genovese, and W. Steiger, "Indium field emission electric propulsion microthruster experimental characterization," *Journal of Propulsion and Power*, vol. 20, no. 2, pp. 211–218, 2004.

[18] A. Genovese, N. Tajmar, M andBuldrini, and W. Steiger, "2000-hour endurance test of indium field emission electric propulsion microthruster cluster," *Journal of Propulsion and Power*, vol. 20, no. 2, pp. 219–227, 2004.

[19] M. Alexander, J. Stark, K. Smith, B. Stevens, and B. Kent, "Electrospray performance of microfabricated colloid thruster arrays," *Journal of Propulsion and Power*, vol. 22, no. 3, pp. 620–627, 2006.

[20] M. Gamero-Castano and V. Hruby, "Electrospray as a source of nanoparticles for ef cient colloid thrusters," *Journal of Propulsion and Power*, vol. 17, no. 5, pp. 977–987, 2001.

[21] A. Smirnov, Y. Raites, and N. Fisch, "Parametric investigation of miniaturized cylindrical and annular hall thrusters," *Journal of Applied Physics*, vol. 92, no. 10, p. 5673, 2002.

[22] D. Lamprou, V. J. Lappas, T. Shimizu, D. Gibbon, and M. Perren, "Hollow cathode thruster design and development for small satellites," in *32nd International Electric Propulsion Conference, Sept 11-15, Weisbaden, Germany*, 2011.

[23] A. Dunaevsky, Y. Raites, and N. Fisch, "Plasma acceleration from radio-frequency discharge in dielectric capillary," *Applied Physics Letters*, vol. 88, no. 25, p. 251502, 2006.

[24] J. P. Sheehan, T. Collard, B. W. Longmier, and I. Goglio, "New low-power plasma thruster for nanosatellites," in *Joint Propulsion Conference, 28-30 July, Cleveland, Ohio*, 2014.

[25] F. Chen, "A compact permanent-magnet helicon thruster," *Plasma Science, IEEE Transactions on*, vol. 43, pp. 195–197, Jan 2015.

[26] M. Martinez-Sanchez and J. Pollard, "Spacecraft electric propulsion - an overview," *Journal of Propulsion and Power*, vol. 14, pp. 688–699, Sept-Oct 1998.

[27] W. Morren, S. Hay, T. Haag, and J. Sovey, "Performance characterizations of an engineering model multipropellant resistojet," *Journal of Propulsion*, vol. 5, no. 2, pp. 197–203, 1989.

[28] G. F. Willmes and R. L. Burton, "Low-power helium pulsed arcjet," *Journal of Propulsion and Power*, vol. 15, no. 3, pp. 440–446, 1999.

[29] W. Deininger, G. Cruciani, and M. Glogowski, "Performance comparisons of low-power arcjets," *Journal of Propulsion*, vol. 11, no. 6, pp. 1368–1371, 1995.

[30] B. Glocker and M. Auweter-Kurtz, "Performance characteristics of a medium power hydrogen arcjet," *Journal of Propulsion and Power*, vol. 9, no. 5, pp. 779–781, 1993.

[31] T. Takahashi, Y. Takao, K. Eriguchi, and K. Ono, "Numerical and experimental study of microwave-excited microplasma and micronozzle flow for a microplasma thruster," *Physics of Plasmas*, vol. 16, no. 8, 2009.

[32] Y. Takao, K. Eriguchi, and K. Ono, "A miniature electrothermal thruster using microwave-excited microplasmas: Thrust measurement and its comparison with numerical analysis," *Journal of Applied Physics*, vol. 101, no. 12, 2007.

[33] T. Takahashi, Y. Takao, Y. Ichida, K. Eriguchi, and K. Ono, "Microwave-excited microplasma thruster with helium and hydrogen propellants," *Physics of Plasmas*, vol. 18, no. 6, 2011.

[34] W. B. Stein, A. A. Alexeenko, and I. Hrbud, "Performance modeling of a coaxial radio-frequency gas-discharge microthruster," *Journal of Propulsion and Power*, vol. 24, no. 5, pp. 1007–1016, 2008.

[35] S. E. Williams, *Experimental Characterization of Radio Frequency Microthermal Thruster Performance*. PhD thesis, Purdue University, 2011.

[36] L. Blackhall and J. Khachan, "A simple electric thruster based on ion charge exchange," *Journal of Physics D: Applied Physics*, vol. 40, no. 8, p. 2491, 2007.

[37] R. Burton and P. Turchi, "Pulsed plasma thruster," *Journal of Propulsion and Power*, vol. 14, no. 5, pp. 716–735, 1998.

[38] P. Chabert and N. Braithwaite, *Physics of Radio-Frequency Plasmas*. Cambridge University Press, 2011.

[39] J. P. Sheehan, B. W. Longmier, E. A. Bering, C. S. Olsen, J. P. Squire, M. G. Ballenger, M. D. Carter, L. D. Cassady, F. R. C. Daz, T. W. Glover, and A. V. Ilin, "Temperature gradients due to adiabatic plasma expansion in a magnetic

nozzle," *Plasma Sources Science and Technology*, vol. 23, no. 4, p. 045014, 2014.

[40] S. A. Bufton and R. L. Burton, "Velocity and temperature measurements in a low-power hydrazine arcjet," *Journal of Propulsion and Power*, vol. 13, no. 6, pp. 768–774, 1997.

[41] S. Muncheberg, M. Krischke, and N. Lemke, "Nanosatellites and micro systems technology capabilities, limitations and applications," *Acta Astronautica*, vol. 39, no. 12, pp. 799 – 808, 1996. International Symposium on Small Satellites for Earth Observation.

[42] R. Boswell, C. Charles, P. Alexander, J. Dedrick, and K. Takahashi, "Plasma expansion from a radio frequency microdischarge," *Plasma Science, IEEE Transactions on*, vol. 39, no. 11, pp. 2512 –2513, 2011.

[43] C. Charles and R. W. Boswell, "Measurement and modeling of a radiofrequency micro-thruster," *Plasma Sources Sci. Technol.*, vol. 21, no. 022002, 2012.

[44] F. Boley, *Plasmas - laboratory and cosmic*. Van nostrand, 1966.

[45] M. A. Lieberman and A. J. Lichtenberg, *Principles of Plasma Discharges and Plasma Processing*. John Wiley and Sons, 2005.

[46] N. S. J. Braithwaite, "Introduction to gas discharges," *Plasma Sources Science and Technology*, vol. 9, no. 4, p. 517, 2000.

[47] T. Kihara, "The mathematical theory of electrical discharges in gases," *Rev. Mod. Phys.*, vol. 24, pp. 45–61, Jan 1952.

[48] H. Smith, C. Charles, and R. Boswell, "Breakdown behavior in radio-frequency argon discharges," *Physics of Plasmas*, vol. 10, no. 3, pp. 875–881, 2003.

[49] S. C. Brown and A. D. MacDonald, "Limits for the diffusion theory of high frequency gas discharge breakdown," *Physical Review*, vol. 76, no. 11, pp. 1629–1633, 1949.

[50] H. Butler and G. Kino, "Plasma sheath formation by radio-frequency fields," *The Physics of Fluids*, vol. 6, September 1963.

[51] H. D. Hagstrum, "Theory of auger ejection of electrons from metals by ions," *Phys. Rev.*, vol. 96, pp. 336–365, Oct 1954.

[52] T. Lafleur and R. W. Boswell, "Particle-in-cell simulations of hollow cathode enhanced capacitively coupled radio frequency discharges," *Physics of Plasmas*, vol. 19, no. 2, p. 023508, 2012.

[53] A. R. Ellingboe and R. W. Boswell, "Capacitive, inductive and helicon wave modes of operation of a helicon plasma source," *Physics of Plasmas*, vol. 3, no. 7, pp. 2797–2804, 1996.

[54] S. Y. Moon, J. K. Rhee, D. B. Kim, and W. Choe, "Alpha, gamma and normal, abnormal glow discharge modes in radio-frequency capacitively coupled discharges at atmospheric pressure," *Physics of Plasmas*, vol. 13, no. 3, 2006.

[55] T. Lafleur, R. W. Boswell, and J. P. Booth, "Enhanced sheath heating in capacitively coupled discharges due to non-sinusoidal voltage waveforms," *Applied Physics Letters*, vol. 100, no. 19, p. 194101, 2012.

[56] H. B. Smith, C. Charles, R. W. Boswell, and H. Kuwahara, "Bias formation in a pulsed radiofrequency argon discharge," *Journal of Applied Physics*, vol. 82, no. 2, pp. 561–565, 1997.

[57] D. Vender and R. W. Boswell, "Electron–sheath interaction in capacitive radio-frequency plasmas," *38th National Symposium of the American Vacuum*, vol. 10, no. 4, pp. 1331–1338, 1992.

[58] A. Fruchtman, "Neutral depletion in a collisionless plasma," *IEEE Transactions on Plasma Science*, vol. 36, no. 2, pp. 403–413, 2008.

[59] D. O'Connell, T. Gans, D. L. Crintea, U. Czarnetzki, and N. Sadeghi, "Neutral gas depletion mechanisms in dense low-temperature argon plasmas," *Journal of Physics D: Applied Physics*, vol. 41, no. 3, p. 035208, 2008.

[60] A. Fruchtman, "The thrust of a collisional-plasma source," *IEEE Transactions on Plasma Science*, vol. 39, no. 1, pp. 530–539, 2011.

[61] A. Greig, C. Charles, and R. Boswell, "Simulation of main plasma parameters of a cylindrical asymmetric capacitively coupled plasma micro-thruster using computational fluid dynamics," *Frontiers in Plasma Physics*, vol. 2, no. 80, 2015.

[62] A. Greig, C. Charles, R. Hawkins, and R. W. Boswell, "Direct measurement of neutral gas heating in a radio-frequency electrothermal plasma microthruster," *Applied Physics Letters*, vol. 103, p. 074101, 2013.

[63] A. Greig, C. Charles, N. Paulin, and R. W. Boswell, "Volume and surface propellant heating in an electrothermal radio-frequency plasma micro-thruster," *Applied Physics Letters*, vol. 105, no. 5, pp. –, 2014.

[64] A. Greig, C. Charles, and R. Boswell, "Plume characteristics of an electrothermal plasma microthruster," *Plasma Science, IEEE Transactions on*, vol. 42, pp. 2728–2729, Oct 2014.

[65] S. Dixon, C. Charles, J. Dedrick, T. Gans, D. O'Connell, and R. Boswell, "Observations of a mode transition in a hydrogen hollow cathode discharge using phase resolved optical emission spectroscopy," *Applied Physics Letters*, vol. 105, no. 1, 2014.

[66] S. Dixon, J. Dedrick, C. Charles, T. Gans, D. O'Connell, and R. Boswell, "Phase resolved imaging of a repetitive extrusion of hydrogen plasma from a hollow cathode source," *Plasma Science, IEEE Transactions on*, vol. 42, pp. 2834–2835, Oct 2014.

[67] D. R. Miller, *Atomic and Molecular Beam Methods*, ch. Free Jet Sources, pp. 15–53. Oxford University Press, 1988.

[68] H. Mott-Smith and I. Langmuir, "The theory of collectors in gaseous discharges," *Phys. Rev.*, vol. 28, pp. 727–763, Oct 1926.

[69] J. P. Sheehan and N. Hershkowitz, "Emissive probes," *Plasma Sources Science and Technology*, vol. 20, no. 6, p. 063001, 2011.

[70] J. R. Smith, N. Hershkowitz, and P. Coakley, "Inflection-point method of interpreting emissive probe characteristics," *Review of Scientific Instruments*, vol. 50, no. 2, pp. 210–218, 1979.

[71] V. A. Godyak and V. I. Demidov, "Probe measurements of electron-energy distributions in plasmas: what can we measure and how can we achieve reliable results?," *Journal of Physics D: Applied Physics*, vol. 44, no. 23, p. 233001, 2011.

[72] S. Dixon, C. Charles, and R. Boswell, "Spatial evolution of eepfs in a millimetre scale radio frequency argon plume," *Journal of Physics D: Applied Physics*, vol. 46, no. 36, p. 365202, 2013.

[73] W. Cox, C. Charles, R. W. Boswell, and R. Hawkins, "Spatial retarding field energy analyzer measurements downstream of a helicon double layer plasma," *Applied Physics Letters*, vol. 93, no. 7, 2008.

[74] Y. Zhang, C. Charles, and R. Boswell, "Transport of ion beam in an annular magnetically expanding helicon double layer thruster," *Physics of Plasmas*, vol. 21, no. 6, 2014.

[75] J. E. Allen, R. L. F. Boyd, and P. Reynolds, "The collection of positive ions by a probe immersed in a plasma," *Proceedings of the Physical Society. Section B*, vol. 70, no. 3, p. 297, 1957.

[76] T. E. Sheridan, "How big is a small langmuir probe?," *Physics of Plasmas*, vol. 7, no. 7, pp. 3084–3088, 2000.

[77] T. E. Sheridan, "The plasma sheath around large discs and ion collection by planar langmuir probes," *Journal of Physics D: Applied Physics*, vol. 43, no. 10, p. 105204, 2010.

[78] I. D. Sudit and F. F. Chen, "Rf compensated probes for high-density discharges," *Plasma Sources Science and Technology*, vol. 3, no. 2, p. 162, 1994.

[79] V. A. Godyak, R. B. Piejak, and B. M. Alexandrovich, "Measurement of electron energy distribution in low-pressure rf discharges," *Plasma Sources Science and Technology*, vol. 1, no. 1, p. 36, 1992.

[80] E. Schrödinger, *Collected Papers of Wave Mechanics*, ch. Quantisation as a Problem of Proper Values: Part I, pp. 1–13. Blackie and Son Limited, 1928.

[81] H. R. Griem, *Plasma Spectroscopy*. McGraw, 1964.

[82] G. P. Davis and R. A. Gottscho, "Measurement of spatially resolved gas-phase plasma temperatures by optical emission and laser-induced fluorescence spectroscopy," *Journal of Applied Physics*, vol. 54, no. 6, pp. 3080–3086, 1983.

[83] U. Fantz, "Basics of plasma spectroscopy," *Plasma Sources Science and Technology*, vol. 15, no. 4, p. S137, 2006.

[84] J. E. Sansonetti and W. C. Martin, "Handbook of basic atomic spectroscopic data," *Journal of Physical and Chemical Reference Data*, vol. 34, no. 4, pp. 1559–2259, 2005.

[85] R. Pearse and A. Gaydon, *The Identification of Molecular Spectra*. Chapman & Hall, 1965.

[86] W. Richards and P. Scott, *Structure and Spectra of Molecules*. John Wiley and Sons, 1985.

[87] D. M. Phillips, "Determination of gas temperature from unresolved bands in the spectrum from a nitrogen discharge," *Journal of Physics D: Applied Physics*, vol. 9, no. 3, p. 507, 1976.

[88] P. J. Bruggeman, N. Sadeghi, D. C. Schram, and V. Linss, "Gas temperature determination from rotational lines in non-equilibrium plasmas: a review," *Plasma Sources Science and Technology*, vol. 23, no. 2, p. 023001, 2014.

[89] V. Linss, H. Kupfer, S. Peter, and F. Richter, "Two n2+ populations with different boltzmann distribution of the rotational levels found in different types of n 2 /ar discharges - improved estimation of the neutral gas temperature," *Journal of Physics D: Applied Physics*, vol. 37, no. 14, p. 1935, 2004.

[90] J.-S. Poirier, P.-M. Brub, J. Muoz, J. Margot, L. Stafford, and M. Chaker, "On the validity of neutral gas temperature by n 2 rovibrational spectroscopy

in low-pressure inductively coupled plasmas," *Plasma Sources Science and Technology*, vol. 20, no. 3, p. 035016, 2011.

[91] S. Y. Moon and W. Choe, "A comparative study of rotational temperatures using diatomic oh, o2 and n2+ molecular spectra emitted from atmospheric plasmas," *Spectrochimica Acta Part B: Atomic Spectroscopy*, vol. 58, no. 2, pp. 249 – 257s, 2003.

[92] B. A. Cruden, M. V. V. S. Rao, S. P. Sharma, and M. Meyyappan, "Neutral gas temperature estimates in an inductively coupled cf4 plasma by fitting diatomic emission spectra," *Journal of Applied Physics*, vol. 91, no. 11, pp. 8955 –8964, 2002.

[93] B. Bai, H. H. Sawin, and B. A. Cruden, "Neutral gas temperature measurements of high-power-density fluorocarbon plasmas by fitting swan bands of c2 molecules," *Journal of Applied Physics*, vol. 99, no. 1, 2006.

[94] H. Nassar, S. Pellerin, K. Musiol, O. Martinie, N. Pellerin, and J.-M. Cormier, "N 2 + /n 2 ratio and temperature measurements based on the first negative n 2 + and second positive n 2 overlapped molecular emission spectra," *Journal of Physics D: Applied Physics*, vol. 37, no. 14, p. 1904, 2004.

[95] L. Mi, P. Xu, and P.-N. Wang, "Temperature determination of n 2 discharge plasma by computational simulation of its emission spectra," *Journal of Physics D: Applied Physics*, vol. 38, no. 21, p. 3885, 2005.

[96] X.-J. Huang, Y. Xin, L. Yang, Q.-H. Yuan, and Z.-Y. Ning, "Spectroscopic study on rotational and vibrational temperature of n2 and n2+ in dual-frequency capacitively coupled plasma," *Physics of Plasmas*, vol. 15, p. 113504, 2008.

[97] C. Biloiu, X. Sun, Z. Harvey, and E. Scime, "Determination of rotational and vibrational temperatures of a nitrogen helicon plasma," *Review of Scientific Instruments*, vol. 77, no. 10, 2006.

[98] C. Biloiu, X. Sun, Z. Harvey, and E. Scime, "An alternative method for gas temperature determination in nitrogen plasmas: Fits of the bands of the first positive system," *Journal of Applied Physics*, vol. 101, no. 7, 2007.

[99] S. G. Belostotskiy, T. Ouk, V. M. Donnelly, D. J. Economou, and N. Sadeghi, "Gas temperature and electron density profiles in an argon dc microdischarge measured by optical emission spectroscopy," *Journal of Applied Physics*, vol. 107, no. 5, pp. –, 2010.

[100] N. Kang, S. Oh, and A. Ricard, "Kinetics of metastable argon atoms in an ar-n2 rf icp discharge," *Journal of Korean Physical Society*, vol. 58, p. 776, 2011.

[101] T. Sakamoto, H. Matsuura, and H. Akatsuka, "Spectroscopic study on the vibrational populations of n2 c3 and b3 states in a microwave nitrogen discharge," *Journal of Applied Physics*, vol. 101, no. 2, 2007.

[102] V. M. Donnelly and M. V. Malyshev, "Diagnostics of inductively coupled chlorine plasmas: Measurements of the neutral gas temperature," *Applied Physics Letters*, vol. 77, no. 16, pp. 2467–2469, 2000.

[103] A. A. Bol'shakov, B. A. Cruden, and S. P. Sharma, "Determination of gas temperature and thermometric species in inductively coupled plasmas by emission and diode laser absorption," *Plasma Sources Science and Technology*, vol. 13, no. 4, p. 691, 2004.

[104] A. Kilinov, P. Veis, C. Foissac, C. Dupret, and P. Supiot, "Spectroscopic characterization of nitrogenargon discharge created by helical cavity," *WDS'07 Proceedings of Contributed Papers, Part II*, pp. 175–180, 2007.

[105] A. N. Goyette, J. R. Peck, Y. Matsuda, L. W. Anderson, and J. E. Lawler, "Experimental comparison of rotational and gas kinetic temperatures in n2 and he-n2 discharges," *Journal of Physics D: Applied Physics*, vol. 31, no. 13, p. 1556, 1998.

[106] R. A. Porter and W. R. Harshbarger, "Gas rotational temperature in an rf plasma," *Journal of The Electrochemical Society*, vol. 126, no. 3, pp. 460–464, 1979.

[107] N. Masoud, K. Martus, M. Figus, and K. Becker, "Rotational and vibrational temperature measurements in a high-pressure cylindrical dielectric barrier discharge," *Contributions to Plasma Physics*, vol. 45, no. 1, pp. 32–39, 2005.

[108] E. Stoffels, A. J. Flikweert, W. W. Stoffels, and G. M. W. Kroesen, "Plasma needle: a non-destructive atmospheric plasma source for fine surface treatment of (bio)materials," *Plasma Sources Science and Technology*, vol. 11, no. 4, p. 383, 2002.

[109] D. Staack, B. Farouk, A. F. Gutsol, and A. A. Fridman, "Spectroscopic studies and rotational and vibrational temperature measurements of atmospheric pressure normal glow plasma discharges in air," *Plasma Sources Science and Technology*, vol. 15, no. 4, p. 818, 2006.

[110] D. M. Zube and R. M. Myers, "Thermal nonequilibrium in a low-power arcjet nozzle," *Journal of Propulsion and Power*, vol. 9, no. 4, pp. 545–552, 1993.

[111] A. Lofthus and P. H. Krupenie, "The spectrum of molecular nitrogen," *Journal of Physical and Chemical Reference Data*, vol. 6, no. 1, pp. 113–307, 1977.

[112] N. Popov, "Investigation of the mechanism for rapid heating of nitrogen and air in gas discharges," *Plasma Physics Reports*, vol. 27, no. 10, pp. 886–896, 2001.

[113] G. Marr, *Plasma Spectroscopy*. Elsevier Publishing Company, 1968.

[114] K. Takahashi, T. Lafleur, C. Charles, P. Alexander, R. W. Boswell, M. Perren, R. Laine, S. Pottinger, V. Lappas, T. Harle, and D. Lamprou, "Direct thrust measurement of a permanent magnet helicon double layer thruster," *Applied Physics Letters*, vol. 98, no. 14, p. 141503, 2011.

[115] G. Herzberg and K. P. Huber, *Molecular spectra and molecular structure*. No. v. 1 in Molecular Spectra and Molecular Structure, Prentice-Hall, inc., 1945.

[116] K. P. Huber and G. Herzberg, *Molecular Spectra and Molecular Structure IV. Constants of Diatomic Molecules*. Van Nostrand Reinhold Company, 1979.

[117] G. M. Barrow, *Introduction to Molecular Spectroscopy*. McGraw-Hill Book Company Inc., 1962.

[118] J. L. Dunham, "The energy levels of a rotating vibrator," *Phys. Rev.*, vol. 41, pp. 721–731, Sep 1932.

[119] E. U. Condon, "Nuclear motions associated with electron transitions in diatomic molecules," *Phys. Rev.*, vol. 32, pp. 858–872, Dec 1928.

[120] J. Franck and E. G. Dymond, "Elementary processes of photochemical reactions," *Trans. Faraday Soc.*, vol. 21, pp. 536–542, 1926.

[121] P. A. Fraser, "A method of determining the electronic transition moment for diatomic molecules," *Canadian Journal of Physics*, vol. 32, no. 8, pp. 515–521, 1954.

[122] R. Zare, E. Larsson, and R. Berg, "Franck-condon factors for electronic band systems of molecular nitrogen," *Journal of Molecular Spectroscopy*, vol. 15, no. 2, pp. 117 – 139, 1965.

[123] M. Roberto, H. Smith, and J. Verboncoeur, "Influence of metastable atoms in radio-frequency argon discharges," *Plasma Science, IEEE Transactions on*, vol. 31, no. 6, pp. 1292 – 1298, 2003.

[124] H. B. Smith, "Studies of plasma breakdown and decay in a capacitive radiofrequency argon discharge," *Physics of Plasmas*, vol. 5, no. 9, pp. 3469–3476, 1998.

[125] D. O'Connell, R. Zorat, A. R. Ellingboe, and M. M. Turner, "Comparison of measurements and particle-in-cell simulations of ion energy distribution functions in a capacitively coupled radio-frequency discharge," *Physics of Plasmas*, vol. 14, no. 10, p. 103510, 2007.

[126] K. Matyash, R. Schneider, F. Taccogna, A. Hatayama, S. Longo, M. Capitelli, D. Tskhakaya, and F. X. Bronold, "Particle in cell simulation of low temper-

ature laboratory plasmas," *Contributions to Plasma Physics*, vol. 47, no. 8-9, pp. 595–634, 2007.

[127] G. A. Bird, *Molecular gas dynamics and the direct simulation of gas flows*. Clarendon, 1994.

[128] C. G. Wilson, Y. B. Gianchandani, R. R. Arslanbekov, V. Kolobov, and A. E. Wendt, "Profiling and modeling of dc nitrogen microplasmas," *Journal of Applied Physics*, vol. 94, no. 5, pp. 2845–2851, 2003.

[129] E. A. Bogdanov, A. A. Kudryavtsev, R. R. Arslanbekov, and V. I. Kolobov, "Simulation of pulsed dielectric barrier discharge xenon excimer lamp," *Journal of Physics D: Applied Physics*, vol. 37, no. 21, p. 2987, 2004.

[130] R. R. Arslanbekov and V. Kolobov, "2-d simulations of striations in direct current glow discharges in argon," *Plasma Science, IEEE Transactions on*, vol. 33, pp. 354–355, Apr 2005.

[131] R. R. Arslanbekov and V. I. Kolobov, "Two-dimensional simulations of the transition from townsend to glow discharge and subnormal oscillations," *Journal of Physics D: Applied Physics*, vol. 36, no. 23, p. 2986, 2003.

[132] S. Yun, V. Kolobov, and G. R. Tynan, "Neutral uniformity and transport mechanisms for plasma etching," *Physics of Plasmas*, vol. 8, no. 6, pp. 3069–3076, 2001.

[133] V. I. Kolobov, "Fokker-planck modeling of electron kinetics in plasmas and semiconductors," *Computational Materials Science*, vol. 28, no. 2, pp. 302 – 320, 2003.

[134] Y. Lu, D. Yan, and Y. Chen, "2-d fluid simulation of dual-frequency capacitively coupled plasma," *Journal of Hydrodynamics, Ser. B*, vol. 21, no. 6, pp. 814 – 819, 2009.

[135] B. Launder and D. Spalding, "The numerical computation of turbulent flows," *Computer Methods in Applied Mechanics and Engineering*, vol. 3, no. 2, pp. 269 – 289, 1974.

[136] E. S. Fishburne, "Transfer of electronic energy between a metastable argon atom and a nitrogen molecule," *The Journal of Chemical Physics*, vol. 47, no. 1, pp. 58–63, 1967.

[137] D. W. Setser, D. H. Stedman, and J. A. Coxon, "Chemical applications of metastable argon atoms. iv. excitation and relaxation of triplet states of n2," *The Journal of Chemical Physics*, vol. 53, no. 3, pp. 1004–1020, 1970.

[138] H. Barankova, L. Bardos, and S. Berg, "Metastable assisted deposition of tin films," *Applied Physics Letters*, vol. 67, no. 11, pp. 1521–1523, 1995.

[139] Z. L. Petrovi, F. Tochikubo, S. Kakuta, and T. Makabe, "Spatiotemporal optical emission spectroscopy of rf discharges in sf6," *Journal of Applied Physics*, vol. 73, no. 5, pp. 2163–2172, 1993.

[140] J. Muoz, J. Margot, and M. Chaker, "Argon metastable and resonant densities in a low-pressure arn 2 inductively coupled plasma," *Journal of Physics D: Applied Physics*, vol. 46, no. 45, p. 455205, 2013.

[141] W. R. Bennett Jr, "Optical spectra excited in high pressure noble gases by alpha impact," *Annals of Physics*, vol. 18, no. 2, pp. 367 – 420, 1962.

[142] A. Meige, O. Sutherland, H. B. Smith, and R. W. Boswell, "Ion heating in the presheath," *Physics of Plasmas*, vol. 14, no. 3, p. 032104, 2007.

[143] F. Penning, *Electrical Discharges in Gases*. Philips Technical Library, 1957.

[144] A. Phelps, "Cross sections and swarm coefficients for nitrogen ions and neutrals in n2 and argon ions and neutrals in ar for energies from 0.1ev to 10kev," *J. Phys. Chem. Ref. Data*, vol. 20, no. 3, pp. 557–573, 1991.

[145] J. Henriques, E. Tatarova, F. M. Dias, and C. M. Ferreira, "Effect of gas heating on the spatial structure of a traveling wave sustained ar discharge," *Journal of Applied Physics*, vol. 90, no. 10, pp. 4921–4928, 2001.

[146] V. Linss, "Spatial distribution of the neutral gas temperature in rf and dc magnetron sputter discharges determined by fitting rotational spectra of the

n2+ using a two-temperature fit," *Spectrochimica Acta Part B: Atomic Spectroscopy*, vol. 60, no. 2, pp. 253 – 263, 2005.

[147] S. De Benedictis, G. Dilecce, and M. Simek, "Excitation and decay of n2 states in a pulsed discharge: Kinetics of electrons and long-lived species," *The Journal of Chemical Physics*, vol. 110, no. 6, pp. 2947–2962, 1999.

[148] B. Bakowski, G. Hancock, R. Peverall, G. A. D. Ritchie, and L. J. Thornton, "Characterization of an inductively coupled n 2 plasma using sensitive diode laser spectroscopy," *Journal of Physics D: Applied Physics*, vol. 37, no. 15, p. 2064, 2004.

[149] M. Shimada, R. Cattolica, and G. R. Tynan, "Electron beam fluorescence temperature measurements of n2 in a semiconductor plasma reactor," *Journal of Vacuum Science & Technology A*, vol. 22, no. 2, pp. 371–376, 2004.

[150] R. A. Arakoni, J. J. Ewing, and M. J. Kushner, "Microdischarges for use as microthrusters: modelling and scaling," *Journal of Physics D: Applied Physics*, vol. 41, no. 10, p. 105208, 2008.

[151] C. D. Pintassilgo, V. Guerra, O. Guaitella, and A. Rousseau, "Study of gas heating mechanisms in millisecond pulsed discharges and afterglows in air at low pressures," *Plasma Sources Science and Technology*, vol. 23, no. 2, p. 025006, 2014.

[152] A. Agarwal, S. Rauf, and K. Collins, "Gas heating mechanisms in capacitively coupled plasmas," *Plasma Sources Science and Technology*, vol. 21, no. 5, p. 055012, 2012.

[153] G. Makrinich and A. Fruchtman, "Experimental study of a radial plasma source," *Physics of Plasmas*, vol. 16, no. 4, p. 043507, 2009.

[154] V. Guerra, E. Tatarova, F. M. Dias, and C. M. Ferreira, "On the self-consistent modeling of a traveling wave sustained nitrogen discharge," *Journal of Applied Physics*, vol. 91, no. 5, pp. 2648–2661, 2002.

[155] R. C. Millikan and D. R. White, "Systematics of vibrational relaxation," *The Journal of Chemical Physics*, vol. 39, no. 12, pp. 3209–3213, 1963.

[156] Y. Itikawa, "Cross sections for electron collisions with nitrogen molecules," *Journal of Physical and Chemical Reference Data*, vol. 35, no. 1, pp. 31–53, 2006.

[157] V. Zhdanov, *Elementary Physicochemical Processes on Solid Surfaces*. Springer US, 1991.

[158] D. R. Pitts and L. E. Sissom, *Theory and Problems of Heat Transfer*. McGraw-Hill Book Company Inc, 1977.

[159] M. Zemansky, *Heat and Thermodynamics*. McGraw-Hill Book Company, Inc.,, 1957.

[160] S. Dixon, C. Charles, R. Boswell, W. Cox, J. Holland, and R. Gottscho, "Interactions between arrayed hollow cathodes," *Journal of Physics D: Applied Physics*, vol. 46, no. 14, p. 145204, 2013.

[161] D. F. Berisford, R. D. Bengtson, and L. L. Raja, "Power balance and wall erosion measurements in a helicon plasma," *Physics of Plasmas*, vol. 17, no. 3, 2010.

[162] C. Charles, A. Bish, R. Boswell, J. Dedrick, A. Greig, R. Hawkins, and T. Ho, "A short review of experimental and computational diagnostics for radiofrequency plasma micro-thrusters," *Plasma Chemistry and Plasma Processing*, pp. 1–16, 2015.